UNIVERSITY OF CALIFORNIA SAN DIEGO

Solid State Electrode-Electrolyte Interface Engineering and Material Processing For All Solid State Batteries

A dissertation submitted in partial satisfaction of the requirements for the Doctor of Philosophy

in

Nanoengineering

by

Han Quoc Nguyen

Committee in charge:

Professor Ying Shirley Meng, Chair
Professor Zheng Cheng
Professor Zhaowei Liu
Professor Shyue Ping Ong
Professor Oleg Shypko

2019

The Dissertation of Han Quoc Nguyen is approved, and it is acceptable in quality and form for publication on microfilm and electronically:

Chair

University of California, San Diego

2019

DEDICATION

To my mentors, friends, and Oanh Truong. I could not have gone this far without you.

EPIGRAPH

"Nothing is impossible, the impossible just takes longer"

-Professor Ying Shirley Meng

"As a scientist, keep your mind open to any possible phenomena remaining in the great unknown. But never forget that your profession is exploration of the real world, with no preconception or idol of the mind accepted, and testable truth the only coin of the realm."

−Edward O. Wilson, Letters To A Young Scientist

"We are all working with incomplete information, and we are all doing the best we can with it."

−John B. Goodenough, Witness to Grace

"For a successful technology, reality must take precedence over public relations, for nature cannot be fooled"

-Richard P. Feynman, Appendix F - Challenger Shuttle Report

TABLE OF CONTENTS

LIST OF FIGURES

LIST OF TABLES

ACKNOWLEDGEMENTS

The work in this thesis would not be possible without the generous support, guidance, and patience from numerous individuals.

First and foremost, I am deeply grateful to Professor Ying Shirley Meng, whom is a tremendous adviser, mentor, and role model. A deep gratitude will forever be reserved for her, for taking a chance on an individual with no research experience with a first-generation educational background. Her everlasting energy and passion for the field of electrochemistry and material science is an endless source of inspiration. Professor Meng's strong work ethic is a superb example to strive for, and has made a true impact on my life.

To Dr. Thomas A. Yersak for the introduction into solid-state electrolyte work.

To Dr. Sunny Hy for the training in the art of scholarly work.

To Dr. Abhik Banerjee for the countless conversations on electrochemistry.

To Dr. Xuefeng Wang for sharing his enthusiasm in science and adventurous nature.

To Dr. Jean-Marie Doux, for sharing his expertise in design and fabrication.

Dr. James Salvador for providing an exceptional example of a professional scientist.

Dr. Milan Gembicky for the technical and engineering skills of X-ray diffraction.

Members of Laboratory for Energy Storage and Conversion: labmates, mentors, and friends.

I would like to thank my collaborators at the Materials Virtual Lab, Dr. Iek-Heng Chu, Dr. Zhi Deng, Hanmei Tang, and Zhuoying Zhu.

To the many others who I've worked with in some capacity: post-docs, PhD students, MS students, and undergrads.

Lastly, to my girlfriend Oanh Truong, who is an endless source of support and patience as I go through the rigors of the doctorate degree.

Chapter 3, in full, is a reprint of the material "Experimental and Computational Evaluation of a Sodium-Rich Anti-Perovskite for Solid State Electrolytes" as it appears in the Journal of the Electrochemical Society, Nguyen, H., Hy, S., Wu, E., Deng, Z., Samiee, M., Yersak, T., Luo, J., Ong, S. P., and Meng, Y. S. 2016, 163, 10, A2165-A2171. The dissertation author was co-primary investigator and author of this paper. The author performed all the experimental work and electrochemical tests. Both Deng and the author designed and analyzed, and wrote the results.

Chapter 4, in full, is a reprint of the material "Insights into the Performance Limits of the $Li_7P_3S_{11}$ Superionic Conductor: A combined First-Principles and Experimental Study" as it appears in the Applied Materials & Interfaces, Chu, I-H., Nguyen, H., Hy, S., Lin, Y.C., Wang, Z., Xu, Z., Deng, Z., Meng, Y.S., and Ong, S.P. 2016, 8, 12, 7843-7853. The dissertation author was the co-author of this paper. The author performed all the experimental work and electrochemical tests. Both Chu and the author designed and analyzed, and wrote the results.

Chapter 5, in full, is a reprint of the material "Single-step synthesis of highly conductive Na_3PS_4 solid electrolyte for sodium all solid-state batteries" as it appears in the Journal of Power Sources, Nguyen, H**.**, Banerjee, A., Wang, X., Tan, D., Wu, E. A., Doux, J., Stephens, R., Verbist, G., Meng, Y.S., 2019. The dissertation author was co-primary investigator and author of this paper. The author performed all the experimental work and electrochemical tests. We thank Dr. Curtis Moore and Dr. Milan Gembicky at the Crystallography Facility at the University of California, San Diego for assisting on the capillary XRD data collection. The characterization work was performed in part at the San Diego Nanotechnology Infrastructure (SDNI), a member

of the National Nanotechnology Coordinated Infrastructure, which is supported by the National Science Foundation under Grant ECCS-1542148.

Chapter 6, in full, is a reprint of the material "Room-Temperature All-solid-state Rechargeable Sodium Ion Batteries with a Cl-doped Na_3PS_4 Superionic Conductor" as it appears in Scientific Reports, Chu, I.H., Kompella, C.S., Nguyen, H., Zhu, Z., Hy, S., Deng, Z., Meng, Y.S., and Ong, S.P. 6, 33733, 2016. The dissertation author was the co-primary investigator and author of this paper. The author performed all the experimental work and electrochemical tests

Chapter 7, in full, is currently being prepared for submission for publication ―Nanoscale Solid-Solid Interfacial Engineering to Enable High Energy All-Solid-State Battery. Banerjee, A., Tang, H., Wang, X., Cheng, J-H. Zhang, M., **Nguyen, H.,** Wynn, T., Wu,, E.A., Doux, J.M., Macwin Dsouza, M., Ong, S.P., Meng, Y.S. The dissertation author is a co-author of this paper. The dissertation author performed XRD and Raman experiments, and discussed results of this paper.

Chapter 8, in full, is currently being prepared for submission for publication ―Enabling A Room Temperature All Soild-State Lithium Metal Battery. **Nguyen, H.,** Doux, J.M., Tan, D., Banerjee, A., Wang, X., Wu,, E.A., Jo, C., Meng, Y.S. The dissertation author is the co-primary investigator and author of this paper. The author conducted all the experimental test and analysis in this work.

Finally, I would like to acknowledge the funding sources that allowed for the work to be conducted: U.S. Department of Energy, Office of Science, Basic Energy Sciences under Award Numbers. DE-SC0012118 (computational studies) and DE- SC0002357 (experimental work), National Science Foundation, Designing Materials to Revolutionize and Engineer our Future

(DMREF) program under grant No. 1436976, Energy & Bio- sciences Institute through the EBI-Shell program contract number PT78832, LG-Chem, and seed funding from Sustainable Power and Energy Center (SPEC).

VITA

2014	Bachelor of Science in Nanoengineering
	University of California, San Deigo
2015	Master of Science, University of California San Diego
2019	Doctor of Philosophy, University of California San Diego

PUBLICATIONS

Nguyen, H.; Hy, S.; Wu, E.; Deng, Z.; Samiee, M.; Yersak, T.; Luo, J.; Ong, S. P.; Meng, Y. S. Experimental and Computational Evaluation of a Sodium-Rich Anti-Perovskite for Solid State Electrolytes. *J. Electrochem. Soc.* **2016**, *163* (10), 2165–2171. https://doi.org/10.1149/2.0091610jes.

Chu, I. H.; **Nguyen, H.**; Hy, S.; Lin, Y. C.; Wang, Z.; Xu, Z.; Deng, Z.; Meng, Y. S.; Ong, S. P. Insights into the Performance Limits of the Li7P3S11 Superionic Conductor: A Combined First-Principles and Experimental Study. *ACS Appl. Mater. Interfaces* **2016**, *8* (12), 7843–7853. https://doi.org/10.1021/acsami.6b00833.

Chu, I.-H.; Kompella, C. S.; **Nguyen, H.**; Zhu, Z.; Hy, S.; Deng, Z.; Meng, Y. S.; Ong, S. P. Room-Temperature All-Solid-State Rechargeable Sodium-Ion Batteries with a Cl-Doped Na3PS4 Superionic Conductor. *Sci. Rep.* **2016**, No. July, 1–10. https://doi.org/10.1038/srep33733.

Wu, E. A.; Kompella, C. S.; Zhu, Z.; Lee, J. Z.; Lee, S. C.; Chu, I.-H.; **Nguyen, H.**; Ong, S. P.; Banerjee, A.; Meng, Y. S. New Insights into the Interphase between the Na Metal Anode and Sulfide Solid-State Electrolytes: A Joint Experimental and Computational Study. *ACS Appl. Mater. Interfaces* **2018**, *10* (12). https://doi.org/10.1021/acsami.7b19037.

Nguyen, H.; Banerjee, A.; Wang, X.; Tan, D.; Wu, E. A.; Doux, J.; Stephens, R.; Verbist, G.; Meng, Y.S. Single-Step Synthesis of Highly Conductive Na 3 PS 4 Solid Electrolyte for Sodium All Solid-State Batteries. *J. Power Sources* **2019**, No. February, 126623. https://doi.org/10.1016/j.jpowsour.2019.05.031.

Tan, D., Wu, E.A., **Nguyen, H.**, Chen, Z., Doux, J.M., Wang, X., Banerjee, A., Meng, Y.S. Elucidating Reversible Electrochemical Redox of Li_6PS_5Cl solid Electrolyte. ACS Energy Letters **2019 submitted**

Banerjee, A., Tang, H., Wang, X., Cheng, J-H. Zhang, M., **Nguyen, H.,** Wynn, T., Wu,, E.A., Doux, J.M., Wu, T., Ma, L., Dsouza, M., Ong, S.P., Meng, Y.S. Nanoscale Solid-Solid Interfacial Engineering to Enable High Energy All-Solid-State Battery. **2019 In preparation**

ABSTRACT OF THE DISSERTATION

Solid State Electrode-Electrolyte Interface Engineering and Material Processing For All Solid State Batteries

by

Han Quoc Nguyen

Doctor of Philosophy in Nanoengineering

University of California San Diego, 2019

Professor Ying Shirley Meng, Chair

Current state of the art commercial lithium ion batteries (LIB) have been successful power sources for portable electronics. The success of this battery has led to its penetration into electric vehicle and grid-scale storage markets. However, large quantities of LIB batteries pose a threat

to public safety, as they are capable of explosive results due to the flammability of the electrolyte.

All-solid-state battery (ASSB) technology is gaining attention because its has properties that can address all the shortcomings of LIB, such as: improved safe battery operations using non-volatile and non-flammable components, enabling the Li metal anode, preventing dendrite propagation, high voltage operation, suitable mechanical properties, and high transference number. Among the known solid electrolytes, sulfides have shown promise due to their processibility at lower temperatures, high ionic conductivity, and ductility compared to their oxide analogs.

Herein, we investigate new SSE material and evaluate their structure and properties. The crystal structure of the SSE is solved through x-ray diffraction. The performance of the SSE is evaluated through electrochemical means such as: electrochemical impedance spectroscopy, Arrhenius behavior, electrochemical stability window, and galvanostatic charge and discharge performance in a battery.

SSE for ASSB is demonstrated to have comparable room temperature ionic conductivity as their LE counterparts. Their performance can be further improved through post-processing reducing grain boundary impedance and defect engineering. The interface of the SSE and electrodes are a formidable technical hurdle to understand and overcome due to their buried nature in the ASSB configuration. The most complex interface is the cathode/SSE interface where parasitic reaction products are formed by chemical and electrochemical means occurs. Through proper interface engineering the stability of the interface can be improved.

A lithium metal anode is demonstrated to reversibly cycle with high voltage cathodes and Li-S chemistries shorting and showing a pathway to safe and high energy density ASSB.

Chapter 1 Introduction and Thesis Outline

Rechargeable batteries are positioned as the best strategy to store and deliver the energy generated from sustainable sources given their success in portable devices and transportation. This technology is currently extending its application for grid-home storage, where it has the potential to take an entire community completely "off the grid." As the demands for these applications rise, so does the need for increased battery performances, and will become more important that the battery supports sustainable energy generation such as: solar, wind, and hydroelectric. Therefore, the next generation batteries need to outperform their predecessors, and research into the fundamental phenomena is needed to improve battery performances.

A battery is a device that stores and delivers electrochemical energy to conduct work, where the energy is actually stored as chemical bonds of the constituent compounds.[1] The first true battery was invented by Volta, which is now known as the "Volta Pile." The individual cells consisted of simple copper-zinc metal electrodes separated by an insulating fabric soaked with electrolyte. The pile design is made up of the individual cells stacked together and connected in series and was able to supply steady current for employment in laboratories at the time.[2] In today's modern world, batteries come in all sorts of sizes and chemistries such as: Lead-acid, Nickel-Metal-Hydrides, and Zinc-batteries.

To date, the most successful battery is the lithium-ion battery (LIB) commercialized by Sony Corporation in 1991. The success of this battery lies in the electrode microstructure design and working mechanism, which greatly improves its properties such as, increased energy density, lack of memory affect, longer cycle life, high-energy efficiency, and high power density.[3] These properties allows the LIB to be smaller and lighter than lead-acid, nickel-

cadmium, and nickel-metal hydride batteries, which reduced market shares of these older batteries.

Both the electrodes are layered materials: the cathode is a layered oxide of lithium cobalt oxide (LCO), and the anode is made of layered graphite. This has been nicknamed the rocking chair battery. The active element lithium is shuttled between the electrodes during battery operations and remains in its ionic state. Therefore, the working mechanism can be conceptualized as a rocking chair, where the gradient of lithium-ion shifts with the passage of current. The lithium ions are shuttled between the electrodes through the liquid electrolyte, which is made up of a lithium salt, such as $LiPF_6$ dissolved in carboneous solvents. While the concentration gradient of lithium ions change at different states of charge across the cell, the concentration of the ions in the electrolyte, in principle, remain the same.

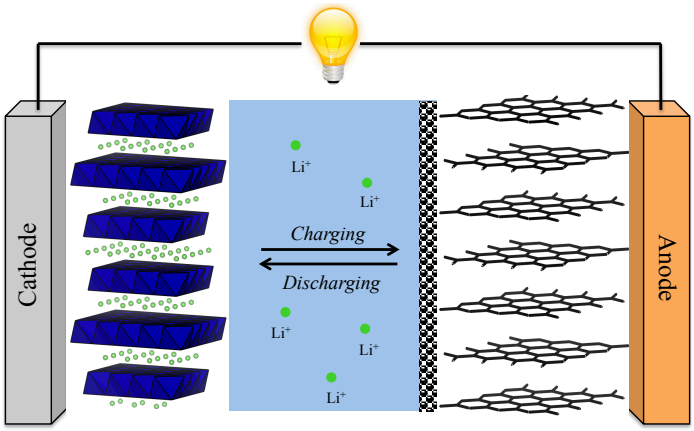

Figure 1.1. Schematic diagram of intercalation lithium-ion batteries. The electrodes are layered structure and lithium-ions are shuttled by the electrolyte during battery operation.

New generations of LIB have been developed by incremental changes in the electrode chemistry: $LiNi_{0.85}Co_{0.1}Al_{0.05}O_2$ (NCA) and $LiNi_8Mn_1Co_1O_2$ (NMC). Tremendous efforts and research have been performed on these now, conventional LIBs, however, the standard design has not changed since their conception.[4,5] It is not to say that there has not been any innovation or discoveries. To the contrary, a large and ever growing body of knowledge in the battery field

is still in existence,[6] and has shown, despite the success of LIBs, they are not without their limitations. LIBs still suffer from: limited energy density, short lifetime, high material cost, limited temperature window, and they present safety issues. Most of the technical hurdles can be traced to the use of graphite anode and the use of flammable liquid electrolytes.

Lithium metal is considered to be the holy-grail of negative electrode materials because is both the lowest density solid metal and has a low reduction potential (-3.7 V vs. SHE). However, dangerous outcomes and poor battery performances have been associated with the use of this metal as an anode with state-of-the-art liquid electrolytes.[7]

The hazards of using lithium metal with conventional lithium ion batteries are due to the dendritic growth of the metallic metal. Over a period of time, the dendrites can internally form an electrical bridge between the electrodes and short the cell, thereby causing an uncontrolled release of the stored energy with catastrophic results. The short circuit heats the cell to a critical temperature known as "thermal runaway," where an exothermic reaction is self-sustained and fire ensues due to the flammable components of the cell, i.e. liquid-electrolyte, carbon containing separator, and binders.

Another technical hurdle associated with the use of lithium metal as the anode is the poor coulombic efficiency (C.E): during continual cycling of the cell, active lithium-ions are lost due to irreversible reactions. This is especially critical in the cell developed by Sony where the anode is graphite and lithium source is finite. Under certain conditions, lithium metal can be plated onto the graphite, instead of intercalating into its Van der Walls gap, and irreversibly react with the electrolyte. The continued loss of lithium ions induces low C.E. and significantly degrade the lifetime of the cell. If one were to use an infinite source of lithium, over time, the liquid

electrolyte can be completely consumed by the reactions with electropositive metal and the battery lifetime would therefore also be adversely affected.[8,9]

All Solid-State Batteries (ASSB) are considered the best strategy to address the challenges that plaque the advanced Li-ion batteries. The key component of an ASSB is the inorganic Solid-State electrolyte (SSE) layer.

SSE are thermally stable over a wider temperature range than their flammable and toxic liquid counterparts. Moreover, SSEs show improved rate performance under conditions where LE would suffer from thermal runaway (~150 ^{o}C). These properties of SSE makes ASSB very safe to use as it entirely eliminates the fire hazard. ASSB have the additional benefit of low self-discharge, versatile geometries, and no leaking.[10] ASSB can potentially increase the energy density of the cell and safely use lithium metal as the anodes, thereby circumventing the long-standing problems associated with conventional LIBs using liquid-electrolytes. With all these benefits, more research efforts are necessary to find suitable SSE that can fit the bill as safe, reliable, and energy dense ASSB.

To date, a range of new materials have been discovered among previous SSE such as: sodium (Na) SuperIonic CONductors (NASICON), Lithium Phosphate OxyNitride (LIPON), and beta-Alumina to name a few.[11–13] These are among a class oxide materials and have been well studied in the literature. However, they have yet to be adopted for large commercial applications as they are not as successful as their liquid counterpart. Their main drawback is their low ion conductivity, which severely limits the power capabilities of the ASSB

With the advent of $Li_{10}GeP_2S_{12}$ (LGPS), interest in the field of SSE have been revitalized as it was shown that sulfur containing SSE can have power capabilities similar to LE, as shown in Figure 1.2. Since this watershed moment in the battery community, a rush of new compounds

have been reported where the ionic conductivity of the SSE are nearly approaching LE or exceeding them all together. The community has seen an increase in SSE research on the synthesis, performance evaluation, and large-scale production has took place since the discovery of LGPS.

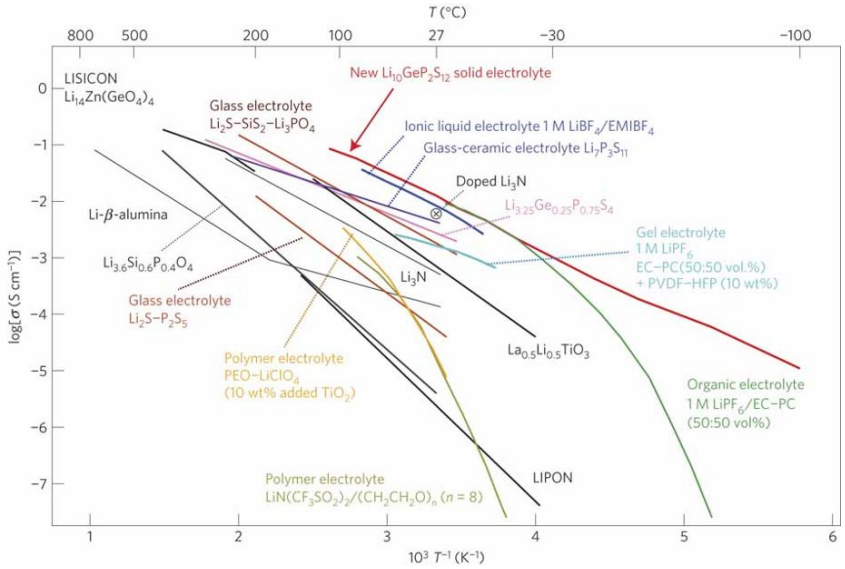

Figure 1.2. Survey comparison of the ionic conductivity of $Li_{10}GeP_2S_{12}$ solid-state electrolyte with other liquid and solid electrolytes.[14]

As the power capabilities of the SSE encroached that of LE it is reasonable that ASSB may outperform LIBs. Other aspects of the SSE have come into focus while the battery community searched for new fast ionic conductors, such as the electrochemical stability window of the SSE and interface stability in contact with the cathode and anode. This dissertation will discuss these issues, which significantly affect the performances of the ASSB.

My PhD thesis consists of nine chapters, including this chapter that provides a general introduction to the battery components and motivation for SSE materials for ASSB. Chapter 2 briefly introduces the characterization tools that I used in my research, which consist of X-ray diffraction, X-ray photoelectron spectroscopy, X-ray tomography, SEM-EDX, and electrochemical impedance spectroscopy. The content of Chapter 3 evaluates a new class of sodium SSE, Na_3OBr anti-perovskite, and examines its performance for battery applications.

Chapter 4 investigates the performance of $Li_7P_3S_{11}$ glass-ceramic electrolyte, a class of sulfur SSE that has lithium ion conductivities comparable to LEs. This work is a combined computational and experimental effort to gain insights to the highly conductive nature of this material. Chapter 5 focuses on processability of the sulfur containing electrolytes, specifically the Na_3PS_4. Large batches of solid-electrolyte can be obtained by this optimization of the synthesis with room temperature processing. Chapter 6 is also combined computational and experimental effort improving the conductivity of Na_3PS_4 SSE by aliovalent doping with halide ions. Chapter 7 considers the cathode-electrolyte interface and reveals complex parasitic reactions occurring through chemical and electrochemical means. This study also reveals the true electrolyte decomposition window of the SSE. Chapter 8 demonstrates the mechanical parameters that are important for successful cycling of ASSB with lithium metal anode at room temperature. Chapter 9 summarizes the overall work and ideas for future research.

Chapter 2 Characterizations Techniques

Electromagnetic radiation is an important probe to investigate material(s) structure and chemical composition. Two fundamental properties of electromagnetic radiation make them ideal as scientific tools; their wavelength and energy. The electromagnetic radiations commonly used range from infrared to X-rays. The corresponding wavelength and energy are shown in Figure 2.1. This range of electromagnetic radiation is of particular importance because the energy and wavelength are in the scales to study materials/molecules.

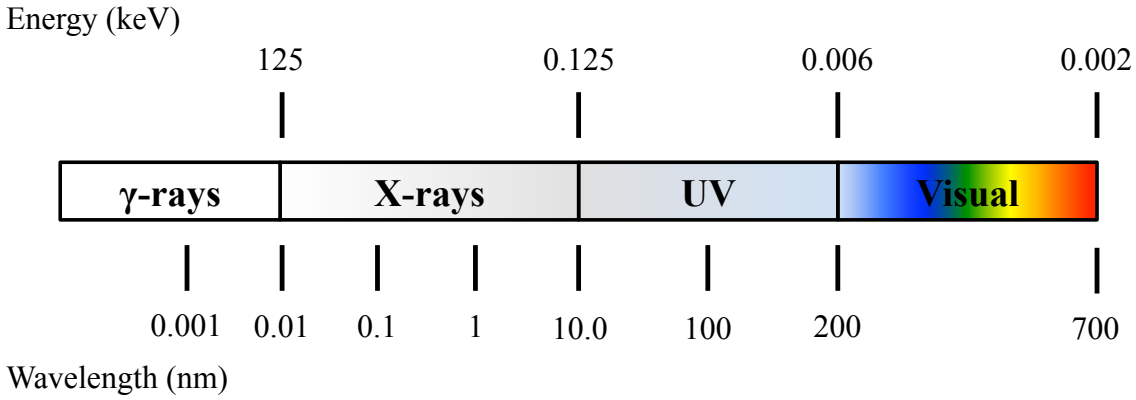

Figure 2.1 Electromagnetic radiation energy and cooresponding wavelengths

Raman Spectroscopy

The majority of light interactions with matter are elastically scattered with no energy lost or gained, also known as Rayleigh scattering, and is not useful for practical purposes. However, some of the light in the visible spectrum can impart energy to a molecule and excite vibrational modes, known as Raman scattering, named after the Sir Chandrashekhara Venkata Raman.[15] This scattering event is a rare occurrence, and is described to occur in 1 of 10^6 scattering events. The basis of Raman spectroscopy are that when a monochromatic light source in the visible range, such as a laser, illuminates and interacts with a sample, Raman scattering occurs if the energy of the scattered light is different from the incident light. The inelastic scattering is filtered

from the Rayleigh scattering and is called Raman shifts. The shifts provide information of the normal vibrational, rotational, and other low frequency transitions in a molecule.

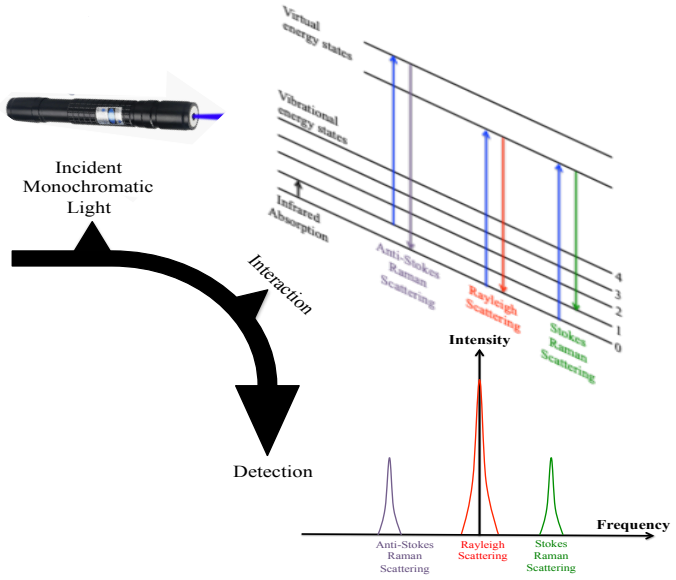

Figure 2.2. Basic schematic of Raman spectrocopy

From a classical description the interaction of light and matter is quantized, such that the scattering only occurs at specific energies for different materials. The excitation causes vibration of specific modes in the material and its response is detectable in IR and Raman spectroscopy briefly described in Figure 2.2. The selection rule for a Raman-active vibration, that there be a change in polarizability during the vibration. This technique is non-destructive and capable of finger printing specific molecules in materials, such as Na_3PO_4, benzene ring, sulfur, and silicon to name a few.[16]

X-ray Diffraction

Electromagnetic radiation in the X-ray range was discovered by Wilhelm Conrad Roentgen in 1895 and has been an instrumental tool for medicine and material science. On the energy landscape, X-rays energies are high enough to transmit through low-density materials. X-ray's are very practical in medical practices as soft tissues can absorb some of the X-rays and

produce a contrast image through X-ray transmission. This property of X-rays allow for internal structures to be observed without destruction of the object in question. X-ray energies are also capable of exciting core level electrons as to identify specific elements in a material. X-rays finally have wavelengths on the scale of atomic distances such that the electron density and lattice array of crystals can be interrogated by diffraction. These properties of X-ray radiation make them highly versatile tools to answer scientific inquiries.

In principle, to spatially resolve two objects, the size of the probe needs to be of the same order of magnitude as the sample. This can be also described as:

$$\Delta \approx \frac{\lambda}{2}$$

Where Δ is the minimum feature that can be resolved, λ is the wavelength of light. Atomic spacing is on the order of Å (10^{-10} m). With photons in the visible spectrum, the smallest feature the human eye will be able to see is approximately 0.1 microns and are not suitable to resolve atomic structures. X-ray radiation has wavelengths in the range of atomic distances and can be used to elude the structures at the atomic scale, specifically radiation with wavelengths below 0.1 nm.

X-ray diffraction is a successful method to surmise the atomic ordering and structure of any material that can form crystals. A typical X-ray wavelength used is 1.54 Å and the source is from copper K_α-radiation. This X-ray source is commonly used because the typical size of crystalline structures are on the order of Angstroms. Diffraction can be is described as a elastic scattering event, where photons that are reflected from matter, and if the conditions are correct, they will constructively interfere and produce a reflected beam.

The father and son duo, Bragg, determined the diffraction condition in mathematical form, describing the relationship between the incident and reflective beam, such that there will be interference. It is known today as Bragg's law:

$$n\lambda = 2\mathrm{d}\sin\theta$$

Where, n is an integer, λ is the wavelength, d is the spacing of the scattering plane, and θ is the angle of incident. At specific angles, the reflected x-rays will constructively interfere, if the distance between similar "plane" of atoms is nλ apart. That is the spacing between the reflective planes are integer multiples of the wavelength, for constructive interference to occur. The reflective X-rays destructively interfere otherwise. A simplified scheme is shown in Figure 2.3.

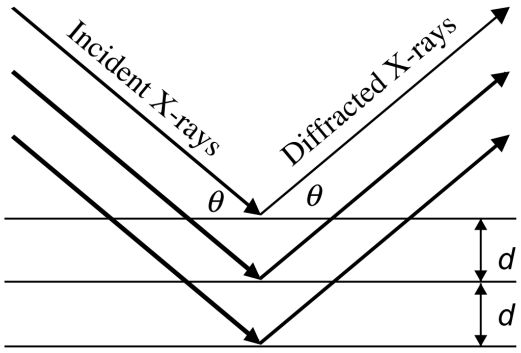

Figure 2.3. The incident X-rays and reflected X-rays make an angle of θ symmetric to the normal crystal planes. Diffraction peaks are observed only if Bragg conditions are satisfied

The above concepts discussed are on the basis of long-range periodicity of crystalline materials. By utilizing Bragg's law the bulk structure of matter and with the use of refinement techniques, the atomic arrangements can be determined. The most famous structure determined through this technique was the DNA helical structure.

X-ray Computed Tomography

X-ray computed tomography is a technique to image internal structure of opaque material. X-ray tomography uses soft x-rays (with wavelengths greater than 0.1 Å) and produce

transmission contrast images. The contrast produced is caused by the attenuation coefficients of the constituent elements or compounds present.

Objects are rotated and sequential 2D projected images are taken at each specified rotation by a planar detector. The images are fed to a computer and a 3D reconstructed image is produced, displaying the internal structure of the object without perturbing it, as shown in Figure 2.4.

The working principle of X-ray tomography is that elements absorb x-rays of differing energies and this produces a contrast image at the detector. This technique is very useful for light elements as they absorb weakly and produce very good contrast imaging. As oppose to heavy elements, which can block an image entirely.

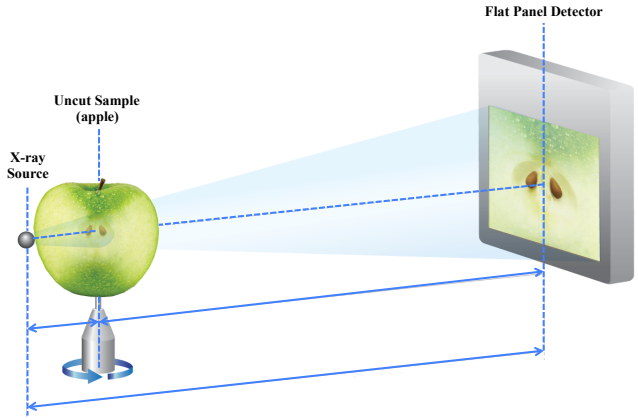

Figure 2.4. Schematic diagram of X-ray CT

A prediction of signal transmission, or attenuation can be calculatd from the attenuation equation.

$$I_t = I_o e^{-\mu x}$$

Where I_o is the incident intensity of the beam, I_t is the intensity of the transmitted beam after interacting with the sample, x is the thickness of the material, and μ is the linear attenuation coefficient. It can be seen that a very thick sample of any attenuation can vastly decrease the signal to be detected.

The linear absorption coefficient, μ, can be further defined by $n \cdot \sigma$, where n is the number of atoms/cm^3 and σ is a proportionality constant that reflects the probability of a photon being scattered or absorbed. Together it states the probability of scattering or absorption for a number of atoms in a volume of material and how it will affect the transmission intensity.

X-ray Photoelectron Spectroscopy (XPS)

XPS is a technique based on Einstein's idea of the photoelectric effect, where the concept of photons carrying quantized energy was used to eject electrons from a surface when photons impinged upon it. XPS was developed by Siegbahn and can be used as a surface characterization technique to probe chemical information of materials.[17] A simple diagram of the photoelectric effect is shown in Figure 2.5.

Figure 2.5. (a) Energy diagram of the core level electron excitation.

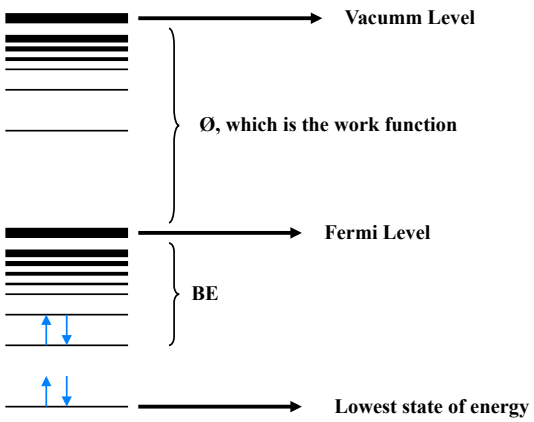

The ejected electron has a kinetic energy (K.E.) that is a sum of the incident photon energy (hυ) minus the binding energy (B.E.) minus the work function of the instrument, as described below.

$$K.E. = h\upsilon - B.E. - \phi_w$$

For a typical XPS, X-ray source, hυ is produced from Mg (K_α: 1253.6 eV), or Al (K_α: 1486.6 eV) and suitable to excite core electrons. The binding energy of the excited electron is unique and dependent upon the bonding environment of a given element giving its own fingerprint region.

Charged particles such as the electrons can interact strongly with matter and the energy of the photoelectron can be maintained if the inelastic mean free path (λ) is minimized. That is, the photoelectron must not inelastically scatter as it traverses to the vacuum level. An important consideration as core level energies is influenced to the change in the local binding environment. The directions of the shifts are dependent on the potential of the nucleus and repelling interactions of the surrounding electrons. Therefore, a higher energy shift can be due to a change in oxidation state or electronegativity. The surface sensitivity and penetration depth make XPS a suitable technique to study the Solid Electrolyte Interphase (SEI) of battery electrodes.

Energy Dispersive X-ray Spectroscopy (EDX)

Every element of the periodic table has a unique number of electrons that reside at specific positions, depicted in Figure 2.6. These positions belong to certain shells, which have different discrete energies for each element.

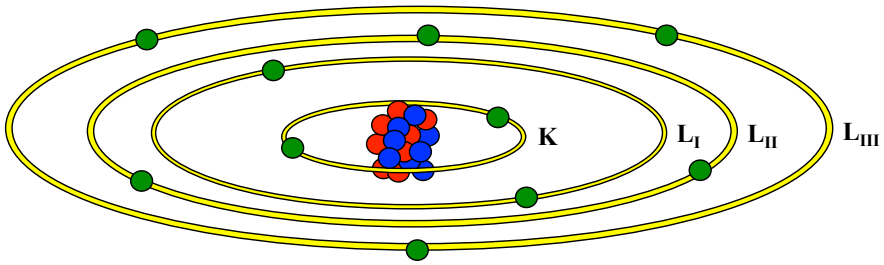

Figure 2.6. Electron orbital shells of an atom. Red and blue spheres are protons and neutrons that form the atomic nucleus, respectively. Green spheres represent the electrons.

The generation of the X-rays in a scanning electron microscope is a two-step process. 1) An impinging electron beam bombards the sample with enough energy to "knock out" a core electron of a constituent element in the sample. Electrons at a higher energy shell will fill the vacant position. 2) When an electron from such a higher-energy shell fills the hole of the lower-

energy shell, the energy difference of this transition in the form of an X-ray electromagnetic radiation.

The emitted X-ray has an energy characteristic of the energy difference between the two orbital shells and therefore depends on the atomic number that is a unique to every element. In this way, X-ray emission energies are a fingerprint of each element and can be used to identify and quantify the elements that are present in a sample.

Electrochemical Impedance Spectroscopy (EIS)

SSE electrolytes are first evaluated by their overall ionic conductivity for energy storage and conversion applications. A straightforward and non-destructive method to determine the power capabilities of an SSE is through EIS.

Ionic diffusion through a SSE entails mobile cations traversing through several different environments: 1) bulk, 2) grain-boundaries, 3) interface, and 4) electrodes. Each environment subjects the mobile ion to different resistance. Through EIS, a time constant of the diffusion process can be produced by impedance spectroscopy.

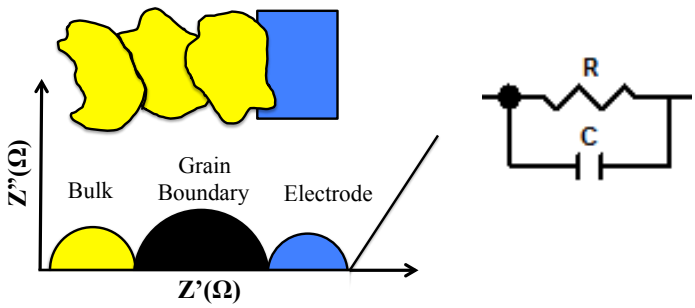

Figure 2.7. Suggested Nyquist interpretation (left). Basic Randal's circuit (right).

The SSE is subjected to an oscillating potential sweeping through a frequency ranging from MHz down to mHz. By sweeping frequency, the collective motion of the cations can be determined at specific frequencies and the impedance response of the process can be broken into its real and

imaginary components. A plot of the real and imaginary impedance components produces a Nyquist plot, where the impedance of specific regions of the SSE produces an arc. The arc can be modeled with a simple Randal circuit use to interpret the impedance of the probed region.

At high frequencies, diffusion in the bulk is interpreted. The Randal circuit elements can be specified by R_b and C_b, as the resistance and capacitance of bulk diffusion, respectively. Capacitance of the bulk diffusion are typically on the order of 10^{-12} F. Lowering the frequency can produce an arc for grain-boundary diffusion, where the diffusion between bulk particles can be represented by R_{gb} and C_{gb}. The typical capacitances of the grain-boundary diffusion are on the order of $10^{-11} – 10^{-8}$ F.

Table 2.1. Capacitance values and possible interpretations[18]

Capacitance (F)	Phenomena Responsible
10^{-12}	Bulk
$10^{-11} – 10^{-8}$	Grain Boundary
$10^{-7} – 10^{-4}$	SSE-Electrode interface

Charge transfer resistance will occur at the SSE-electrode interface, where the oxidation state of the cation can change. This impedance can be measured at lower frequency still.

The last component typically observed in the Nyquist plot has a characteristic of a tail in the low frequency region. The cation is probed in the electrode and its impedance profile as characterized mass transfer.

By fitting Randal circuits to observed Nyquist arcs, the ionic conductivities of SSE can be quantified by the collective real component of impedance of the bulk and grain-boundary

contributions, the sum of R_b and R_{gb}. Normalization to the sample geometry produces the overall ionic conductivity of the SSE as described below.

$$\sigma_i = Z_{real,t}\frac{L}{A}$$

$Z_{real,t}$ is the sum real impedance of the bulk and grain-boundary, A is the cross-sectional measurement area of the sample, L is the thickness of the measured area, and σ_i is the total ionic conductivity in S cm^{-1}.

The activation energy barrier can be extracted through Arrhenius measurements, by exploiting the temperature dependence of the thermally activated diffusion, which is described as:

$$\sigma_i = Ae^{-\frac{E_a}{k_b T}}$$

σ_i is the ionic conductivity at the specified temperature, A is the pre-exponential factor containing the geometric factors of diffusion, k_b is Boltzmann's constant, T is the absolute temperature in Kelvin, and E_a is the activation energy barrier of diffusion. Taking the $\log_{10}$ of both sides produces an equation of a line:

$$\log_{10}\sigma_i = \log_{10} A - 2.3\log_{10}\frac{E_a}{k_b T}$$

Where the slope of the line is E_a. The y-intercept of the Arrhenius plot contains the geometric description of the diffusion through the crystallographic structure specific to the SSE.

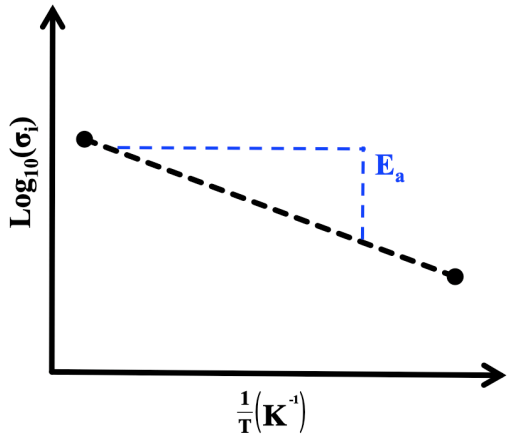

Figure 2.8. A general Arrhenius behavior of SSE ionic conductors

Chapter 3 Experimental and Computational Evaluation of a Sodium-Rich Anti-Perovskite for Solid State Electrolytes

3.1. Introduction

Batteries with liquid electrolytes are ubiquitous since they are economical and practical. They can be found in consumer electronics, power tools, electric vehicles, and many other electronic devices that we encounter in our everyday lives. However, these conventional batteries have safety issues as they typically contain toxic, flammable, and corrosive materials.[19,20] For large-scale energy storage applications these concerns become especially important as they can pose serious health hazards or cause an environmental disruption. Recently, there has been growing interest in solid-state electrolytes as they can make batteries non-flammable, lower maintenance, and also have a longer shelf life due to unity transference number and a lower self discharge rate.[19] Such batteries can withstand more demanding loads and continue to operate without the fear of catastrophic failure.[20,21] Solid electrolytes also have the potential to improve battery performance since they have the potential to be utilized with elemental metals such as lithium or sodium for the anode, which would increase the energy density of the battery.[22] For these reasons, all-solid-state batteries are emerging as suitable candidates for large-scale energy storage. Some examples of solid electrolytes include NASICON, chalcogenide glasses, garnets, and LiPON, but their major drawbacks are that their synthesis and processing methods are energy extensive and complex or limited in scale.[11,12,23–26] Recently developed lithium-rich anti-perovskites (LiRAP) with the formula Li_3OX, where X is a halogen or mixture of halogens, was inspired by the F^- superionic conductivity of the $NaMgF_3$ perovskite.[10] Zhao et al. proposed that the electronically inverted anti-perovskite configuration would yield Li^+ superionic conductivity as the Li^+ cation would become the conductive species.[10] Since then, interest in the LiRAP has

grown and it has been the subject of many electrochemical experiments and theoretical studies to determine its suitability as a solid electrolyte.[27–33] Whenever a new lithium compound is discovered, a common trend in the battery community is to investigate the sodium analog.[34] Anti-perovskites are not an exception: shortly after the conductivity of the LiRAP was reported, so was the ionic conductivity of the NaRAP analog.[35] Na-ion batteries are considered a possible lower cost alternative to Li-ion batteries due to the abundance of sodium in the Earth's crust which is orders of magnitude higher than that of lithium.[36] This positions Na-ion batteries as a candidate for large-scale energy storage systems.[20] Previous efforts to increase the conductivity of anti-perovskite involved defect engineering such as doping or non-stoichiometric mixtures during synthesis.[27,35] We chose a complementary approach and sought to increase the ionic conductivity in the NaRAP via a suitable post-processing method.

Spark plasma sintering (SPS) is a processing technique, which can rapidly densify solid materials compared to conventional sintering, or hot-pressing techniques. These techniques employ convective heating while in SPS, rapid Joule heating takes place. Materials thus can be prepared within minutes with densities in excess of 90% of their theoretical value.[37] Since SPS allows for the intimate joining of materials with disparate melting and sintering temperatures, this technique has been extended to solid-state electrolytes and all solid-state batteries where it has been demonstrated that the mass transport phenomena are enhanced due to the increased inter-particle contact area.[38–42] In this work, the NaRAP Na_3OBr was synthesized by a single step solid-state reaction. We processed Na_3OBr via room-temperature cold-pressing (CP) and SPS and compared the effects of the two methods on the local microstructure and the electrochemical performance. In addition, we investigated the performance of Na_3OBr by considering the

formation energies of intrinsic diffusion mediating defects as estimated from first principles calculations.

3.2. Experimental Material Synthesis

Due to the hygroscopic nature of the starting materials and the electrolyte, all synthesis, material handling, and measurements were carried out in an Argon filled glove box (MBraun, H_2O < 1 ppm, O_2 < 1 ppm) unless otherwise noted. Na_3OBr was synthesized from sodium oxide (Sigma Aldrich, 80% Na_2O and 20% Na_2O_2) and NaBr (Alfa Aesar, 99.999%). These precursors were mixed and ground into a fine powder with an agate mortar and pestle for 10 minutes. The mixture was hydraulically pressed into 13 mm-diameter cylindrical pellets at 370 MPa using a stainless steel die (Carver, Inc.). The pellets were placed on an alumina crucible and heated in an electric furnace at 450◦C for 24 hours where the solid-state reaction described in Eqaution 1. took place.

$$0.8Na_2O + 0.2Na_2O_2 + NaBr \rightarrow Na_3OBr + 0.1O_2 \uparrow \quad [1]$$

Subsequently the pellets were quenched to room temperature by sandwiching the pellets between two large copper blocks. To make the CP sample, the as-synthesized Na_3OBr pellets were ground into a fine powder and pressed at room temperature into a 28 mm diameter pellets with a stainless steel die (Carver, Inc.) at a pressure of 60 MPa. The CP pellet was heated to 450°C for 24 hours and quenched by sandwiching between two copper blocks. To form the SPS sample, as-synthesized Na_3OBr pellets were ground into a fine powder in agate mortar and pestle. The powder was loaded into a 20 mm diameter graphite die with the interior lined with a graphite sheet. The loaded graphite die was placed into the chamber of the SPS machine (Thermal Technology SPS 10–3) and pressed to a preload pressure of 5 MPa. The loaded dies were briefly exposed to air during transport from glove box to SPS equipment. A tight fitting

between the graphite die and graphite foil provides an adequate seal thus protecting the material from moisture during its brief transport in air. The material was heated to 450°C at a rate of 100°C min^{-1} and subjected to a pressure of 60 MPa at a ramp rate of 100 MPa min^{-1}. The temperature and applied pressure dwell times were 5 minutes each. The pellet was conductively cooled to room temperature within the SPS chamber. The heat-treatment and pressurization were all conducted in the flowing argon environment. Upon completion of the respective heat treatment, the surfaces of both the CP and SPS pellets were polished with sandpaper. The dimensions of the pellets were recorded.

3.3. Materials characterization

The relative density of the SPS sample was determined by Archimedes' principle with toluene as the immersing fluid. To ensure that our samples did not react with toluene, a pellet fragment of Na_3OBr was immersed in toluene for 1 hour and then dried at 120°C for 12 hours. The mass of the sample was recorded before immersion and after drying. The relative density of the CP material was calculated by measuring the mass and the dimensions of the pellet. The microstructure of the CP and SPS samples were obtained by imaging their fracture cross sections with a scanning electron microscope (SEM). The as-synthesized Na_3OBr powder was also imaged. Iridium was sputtered onto the SEM samples by an Emitech sputter coater for 7 seconds with a current of 85 mA. Images were obtained with a Philips XL-30 SEM operating at 5 kV. The images were analyzed with ImageJ to quantify the area percentage of void spaces.[43] The sample was briefly exposed to air during transport from the sputtering tool to the SEM, but we do not expect this to drastically change the relative porosity of our samples. Energy-Dispersive X-ray Spectroscopy (EDS) was conducted on a Philips XL30 ESEM using a 40 μm aperture. Samples were prepared for the SEM as previously described. EDS was conducted on the surface

of an as-synthesized pellet. The energy range of the scan was from 0–15 keV as the accelerating beam voltage was 15 kV. The dwell time was 5 minutes. X-ray diffraction (XRD) samples were prepared in a glove box and sealed using polyimide tape to protect the samples from atmospheric conditions during acquisition. XRD data of the as-synthesized, CP, and SPS samples were collected by a Rigaku Rotaflex RU-200B diffractometer using Cu Kα radiation. The 2θ scan range was from 10 to 70°. Rietveld refinement on the XRD data was carried out using GSAS software with EXPGUI in the range of 25–70°.[44] The lower angle data was excluded since the polyimide tape yields a broad peak from 15–25°.

3.4. Electrochemical characterization

Electrochemical impedance spectroscopy (EIS) measurements were conducted using an impedance analyzer (Solartron 1260). The frequency range was 1 MHz–10 mHz and the applied AC potential was 100 mV. Colloidal silver paste (Ted Pella, 16032) was applied to the top and bottom surfaces of the CP and SPS pellets to serve as electrodes and stainless steel plates were used as the current collectors. The paste was cured at 120°C for 30 min on each side to remove the solvents. Temperature-dependent impedance measurements were collected by heating the pellets in an electric furnace from room temperature to 280°C in 20°C increments. The heating rate was 1°C min^{-1} to avoid temperature over-shoot and measurements were conducted after the target temperature was held for an hour to allow for temperature stabilization. The ionic conductivity was determined from fitting the Nyquist plots and normalizing via the dimensions of the pellet. The activation energy (E_a) for Na ion diffusion was calculated from the slope of the Arrhenius plot.

3.5. Defect modeling and formation energy computation

All density functional theory (DFT) calculations were performed using the Vienna Ab initio Simulation Package (VASP)[45] within the projector augmented wave approach.[46] The Perdew-Burke-Ernzerhof (PBE) generalized-gradient approximation (GGA) was adopted for all calculations.[47] A k-point density of at least 1000/(number of atoms in unit cell) was used and the energy cutoff was set to 520 eV. A 3 × 3 × 3 supercell with 135 atoms was used to construct the configurations for all types of defects, including a Na Frenkel defect ($V_{Na} + N_{ai}$), a Na vacancy coupled with substitutional exchange of O by Br ($V_{Na} + Br_O$) and a Na interstitial coupled with substitutional exchange of Br by O ($Na_i + O_{Br}$).

We estimated the mixing energy of structures with defects using the following equation:

$$E_{mix} = E\ (Na_{2-x}O_{1-x}Br_x\ ) - (1 - x)\ E\ (Na_2O) - xE(NaBr), \quad [2]$$

where E ($Na_{2-x}O_{1-x}Br_x$) is the total energy of the configuration of interest, x is the fraction of Br and E (Na_2O) and E (NaBr) are the total energy per formula unit of Na_2O and NaBr, respectively. We also estimated the mixing energy of defect-free Na_3OBr and the result was normalized to a 3 × 3 × 3 supercell for comparison. The total energy of Na_2O, NaBr, and defect-free Na_3OBr were queried from the Materials Project database[48,49] and the analyses were carried out using the Python Materials Genomics (pymatgen) library.[50]

3.6. Results and Discussion

To verify the phase purity of our synthesized material, X-ray diffraction data was collected from the as-synthesized, CP, and SPS materials. Figure 1a presents the respective crystalline structures and phases of our materials. Crystal structure information was determined by Rietveld refinement and the atomic positions of each phase are presented in Table I. The main phase present in the sample was found to be cubic Na_3OBr with trace impurities identified as unreacted NaBr (<5 wt%). The space group P m −3 m (221) of the NaRAP crystal structure is

represented in Figure 1b. According to Rietveld refinement results, the synthesis pathway described in Eq. 1 resulted in the successful formation of Na_3OBr from readily available sodium oxide sources, which consist of a mixture of sodium oxide and sodium peroxide. Thus we demonstrate an alternative synthesis pathway without the use of sodium metal or NaOH as previously reported.[19,35,38] The detailed refinement calculations are shown in Figure 2, and the obtained lattice parameters, tabulated in Table II, are in good agreement with previous reports.[35,51] Subsequent processing of the NaRAP material did not change the crystal structure; in both the CP and SPS cases, the sample was predominantly the NaRAP phase. As seen in Table II, the weight percent of unreacted NaBr is subsequently reduced after the material was processed. There is likely some unreacted sodium oxide which was undetectable with our lab XRD and processing of the as-synthesized material drove the reaction between sodium oxide and NaBr to further completion.

Since the as-synthesized pellets came into contact with copper blocks during the quenching process, EDS was conducted in order to investigate any presence of copper. The spectrum is shown in Figure 1c. Major peaks were identified as the O K_α (0.52 keV), Na K_α (1.04 keV), and Br L_α (1.49 keV) peaks. The Ir M peak (1.98 keV) is from the sputtered Ir and the C K_α peak (0.28 eV) is from the environment or from the instrument. Although the Cu L_α line (0.930 keV) would be difficult to detect, as the Na K_α peak would mask the signal, we also see no significant signal at 8.04 keV, the characteristic Cu K_α line. Coupled with the X-ray diffraction results, where Na_3OBr and NaBr accounted for the observed peaks, copper is not incorporated into our samples.

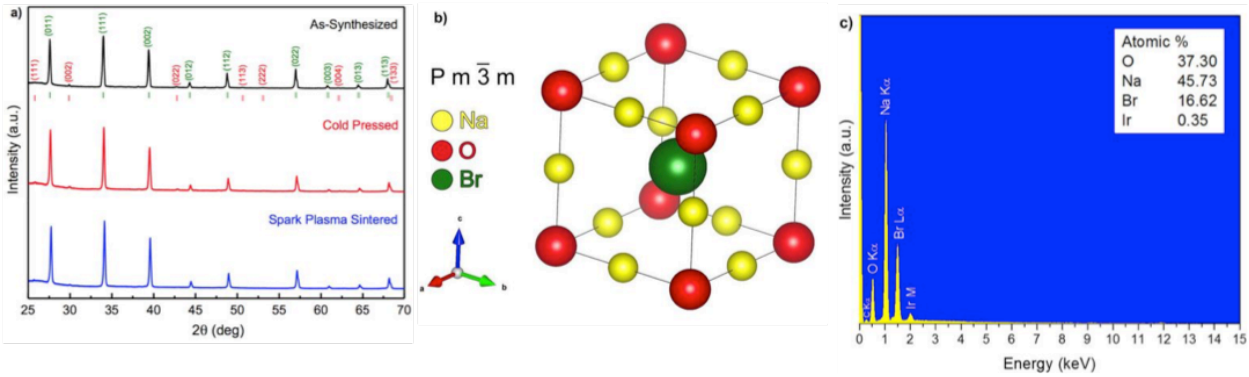

Figure 3.1. XRD pattern of Na_3OBr: as-synthesized (top), Cold-pressed (middle) and SPS (bottom). Green and red Miller indexes correspond to the Na_3OBr phase and NaBr phase, respectively. b) Space group representation of Na_3OBr crystal. c) EDS spectrum taken on the surface fragment of an as-synthesized Na_3OBr sample. Inset: atomic percentages of the detected elements

Table 3.1. Atomic positions for Na_3OBr and NaBr phase for the as-synthesized, CP, and SPS samples, as determined from Rietveld refinement

Atoms	X	Y	Z	Occupancy
		Na_3OBr		
Na	1/2	0	0	3
O	0	0	0	1
Br	1/2	1/2	1/2	1
		NaBr		
Na	0	0	0	1
Br	1/2	1/2	1/2	1

To determine a suitable immersion medium for the density measurement by Archimedes' principle, the results of the toluene stability test are shown in Table III. The difference in mass between the pellet before and after immersion is negligible and the pellet fragment remained intact after the test. Based on this result, Na_3OBr is stable in toluene. The relative density of the CP and SPS samples compared to Na_3OBr's theoretical value was measured to be 89% and 96%,

respectively. This is the first indication that SPS densified our Na_3OBr sample to a higher degree than CP. To examine the microstructure of Na_3OBr, SEM images of the as-synthesized powder, CP cross-section, and SPS cross section were collected. These images are shown in Figures 3a, 3b,and 3c, respectively. The particle morphologies are similar between the as-synthesized, CP and SPS samples, however, in the as-synthesized and CP samples, a significant amount of porosity is evident. This is in contrast to the SPS sample, where there is an observable reduction in the amount of pores. ImageJ was used to quantify the area percentage of the porosity in the CP and SPS samples and the results are shown in Figures 3d and 3e. The area percentage of the porosity was calculated to be 3.98% for the SPS sample compared to 13.79% for the CP sample. These porosity values complement our density measurements well. Although SPS densified our material, the porosity of the material is still visible in the SEM image, in contrast to sulfide-based materials, where SPS processing resulted in a nearly uniformly dense material.[52] A detailed analysis of the contribution of the porosity to the ionic conductivity is discussed in the following section.

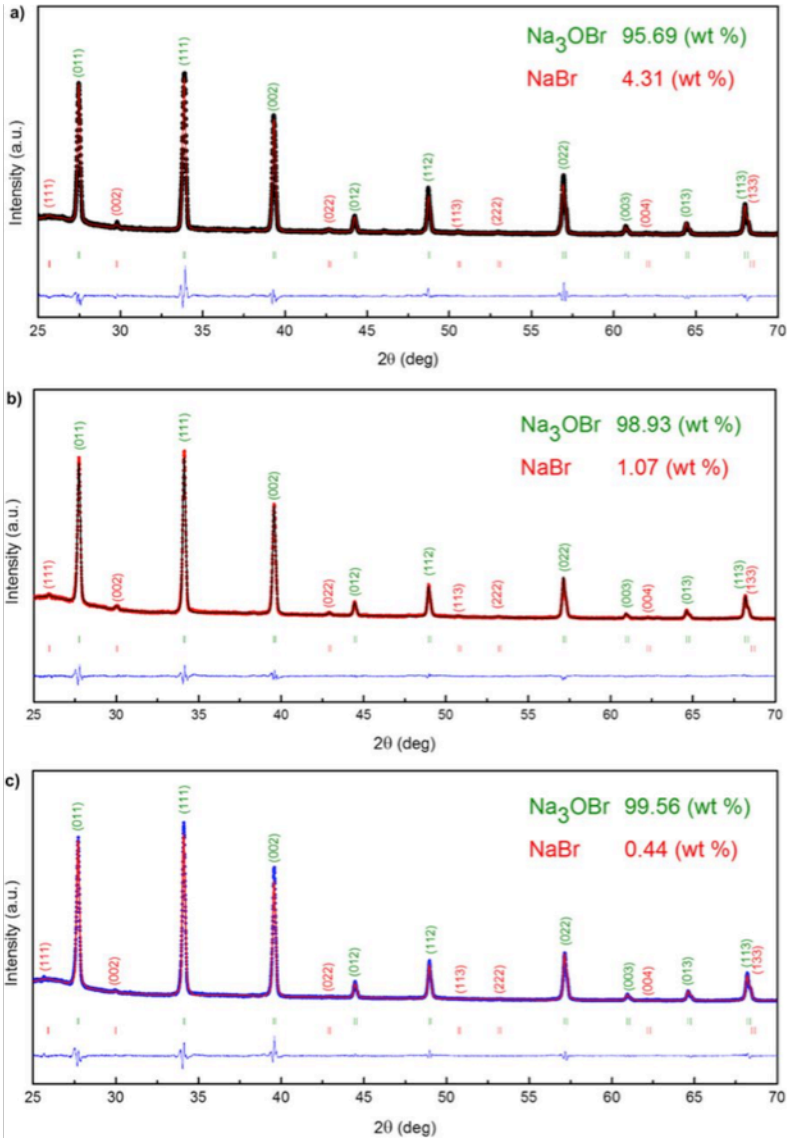

Figure 3.2. Rietveld refinement of the a) as-synthesized sample, b) CP sample, and c) SPS sample. Green and red miller indexes correspond to the Na_3OBr and NaBr phases, respectively.

Table 3.2. Phase fractions and lattice parameters for the as-synthsized, CP, and SPS samples, as determined from Rietveld refinement

Phase	As-Synthesized wt%	CP wt%	SPS wt%	As-Synthesized Lattice Parameters (a=b=c)	CP Lattice Parameters (a=b=c)	SPS Lattice Parameters (a=b=c)
Na_3OBr	95.70%	98.93%	99.56%	4.55757(6) Å	4.56418(6) Å	4.56216(5) Å
NaBr	4.31%	1.07%	0.44%	5.96238(6) Å	5.97050(5) Å	5.97420(5) Å

Table 3.3. Mass of a Na_3OBr pellet fragment before and after immersion in toluene

Mass before immersion in toluene (g)	Mass after immersion in toluene (g)	Percent Difference
0.2185	0.2184	0.046

Electrochemical impedance spectroscopy was performed to analyze the Na+ ionic conductivity of the CP and SPS samples. Figures 4a and 4b show the Nyquist plots of the CP and SPS samples, respectively, measured at 180°C. Our equivalent circuit was derived from a brick-layer model proposed by Huggins.[53] The circuit consists of resistors and constant phase elements (CPE) in the following configuration to represent our cell: The resistor, R_b, represents bulk impedance while the parallel RC combination, R_{int} and CPE_{int}, represents the interfacial impedance contribution. CPE_{geom} represents the presence of the electrolyte material having a finite dielectric constant between two electronically conducting electrodes. These elements model the arc formed from the impedance response. The last element in series, $CPE_{electrode}$, captures the low frequency electric double layer effects of the ion blocking electrode/electrolyte interface, found at the tail section of the spectra. For our CP sample, interfacial impedance was found to have a larger contribution compared to the bulk impedance. A similar result was also observed with the LiRAP, where it was reported that the dominant contribution to the impedance

spectra was from the grain boundaries.[54] While different phenomena have been reported to be responsible for resistive behavior in various ionic conductors,[55] the large interfacial impedance in the CP sample specifically can be attributed to the poor sintering and low relative density of the sample. In contrast, the interfacial impedance of the SPS sample was found to be drastically reduced and its conductivity was calculated to be 1.29×10^{-5} S cm^{-1} compared to 8.91×10^{-8} S cm^{-1} for the CP sample. This is expected as our SEM image shows a reduction in the open porosities of the SPS sample; the increase in contact area between Na_3OBr particles is due to the improved sintering. Although the interfacial impedance of the SPS material is reduced by three orders of magnitude, interestingly, the results for the bulk conductivity are similar between CP and SPS: 2.16×10^{-7} S cm^{-1} and 9.02×10^{-7} S cm^{-1}, respectively. Thus, this comparison between CP and SPS enabled us to investigate not only the effect of SPS on the sintering and interfacial conductivity, but also the intrinsic bulk ionic conductivity of Na_3OBr. The activation energy barrier was calculated from the linear Arrhenius plot displayed in Figure 4c and determined to be 1.142 eV and 0.837 eV for the CP and SPS samples, respectively. Both the decrease in the Na^+ migration energy barrier and the reduction in the interfacial impedance in the SPS sample are attributed to the improved sintering, which ultimately led to an increased overall ionic conductivity. We also previously observed a higher weight percent of the Na_3OBr phase after processing via SPS, which may have contributed to an increase in the overall conductivity by reducing the concentration of impurities.

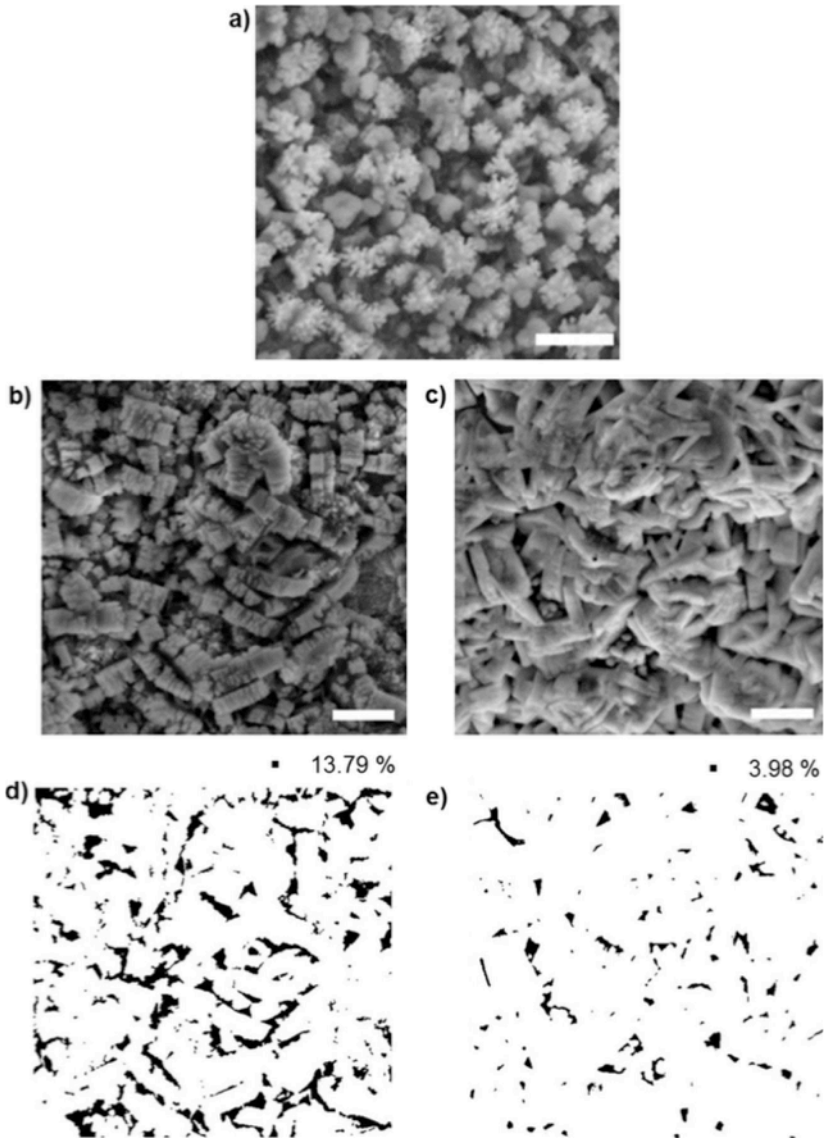

Figure 3.3. SEM and ImageJ analysis of CP and SPS pellets. SEM images of a) the as-synthesized powder, b) CP cross section, and c) SPS cross section. Scale bars are all 1 µm. ImageJ color analysis and quantification of the void spaces in the d) CP and e) SPS SEM images.

Although we observed an improvement in ion conductivity of Na_3OBr processed via SPS, its conductivity is on the order of 10^{-6} S cm^{-1} at temperatures greater than 200°C. We can infer that the room temperature conductivity of NaRAP would be much lower than LiRAP which has reported conductivities on the order of 10^{-6} S cm^{-1} at room temperature.[38] Previous studies

have been conducted to explain the mechanism behind lithium superionic conductivity in LiRAP.[13–17, 56–59] Ab initio molecular dynamics simulations showed that pristine anti-perovskites are not intrinsically superionic conductors; their dense crystal structures do not provide paths for fast ion diffusion.[60] The ionic conductivity of these materials therefore depends on defect density. In contrast, other Li-ion solid-state conductors such as lithium lanthanum titanate (LLTO) and $Li_{10}GeP_2S_{12}$ (LGPS) contain vacant crystallographic sites which facilitate superior ion migration.[14,61] It has been demonstrated that experimentally introducing vacancies in LiRAPs dramatically increases lithium ion conductivity.[44] Thus, for LiRAP to have superionic conductivity, ion transport-facilitating defects must be deliberately generated during synthesis or processing.[16]

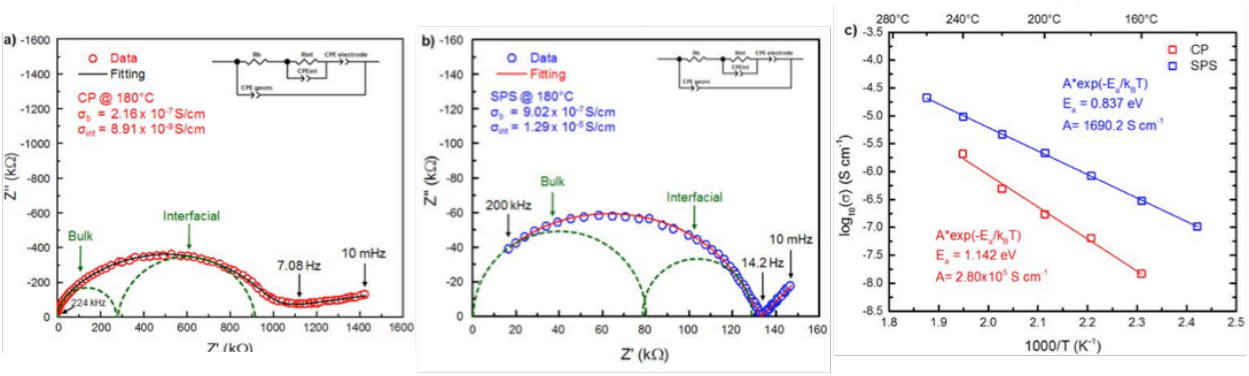

Figure 3.4. Electrochemical Results. Nyquist plot and fitting of the a) CP sample and b) SPS sample, taken at 180°C. c) Arrhenius plot of the CP and SPS samples.

In pristine anti-perovskites, the only defects that can facilitate ion transport are thermally generated. One such defect is an interstitial from a Frenkel defect. In Li_3OCl, the high formation energy of the Li Frenkel defect (1.94 eV) suggests it is extremely difficult to generate a significant concentration of these defects solely by thermal excitation.[17] The computed mixing energies of three types of defects for Na_3OBr are plotted in Figure 5. For the Na Frenkel defect, its mixing energy is 2.53 eV higher compared with defect-free Na_3OBr, which means that the energetic cost of forming the Na Frenkel defect in Na_3OBr is even higher than that in Li_3OCl. We also explored other possible cases for generating a Na vacancy or interstitial, such as Br^- for O^{2-} and O^{2-} for Br^-, respectively, which were previously found to be more energetically favorable than the Frenkel defect in Li_3OCl.[17] In Na_3OBr, the Br^- for O^{2-} substitutional defect had a mixing energy of 2.77 eV and the O^{2-} for Br^- substitution had a mixing energy of 3.03 eV. Unlike Li_3OCl, these energetic costs are all higher than even the Na Frenkel defect.[17]

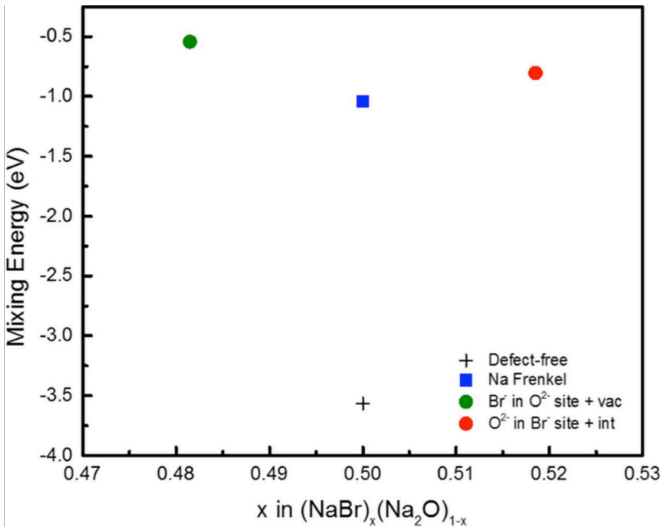

Figure 3.5. Mixing energies for charge-neutral defects represented as deviations from the ideal Na_3OBr anti-perovskite stoichiometry.

The mixing energies of the ion diffusion-facilitating defects in Na_3OBr are all much larger than the mixing energies in LiRAPs. This, coupled with the phase purity of our Na_3OBr samples as determined from XRD, could explain the relatively lower overall conductivity of Na_3OBr versus LiRAPs. We can infer that the amount of thermally generated defects in anti-perovskites, whether vacancies or interstitials, is much lower compared to the concentration of defects that can result from doping or depletion during synthesis.[16] In this context, NaRAPs should be engineered in a similar manner to LiRAPs. Namely, a combination of optimization strategies such as SPS, doping using aliovalent halogens, divalent cations, or the creation of non-stoichiometric anti-perovskites by depletion, could yield NaRAPs with higher ionic conductivity.[11,14,15,38,40]

3.7. Conclusions

We successfully synthesized the solid electrolyte Na_3OBr via a single step heat-treatment from readily available sources. This synthesis method can also be used to synthesize different NaRAP compounds such as Na_3OCl or $Na_3OCl_xBr_{(1-x)}$ ($0 < x < 1$). This reaction mechanism can

be easily scaled up for production of large quantities of solid-state electrolytes and modified to create NaRAP compounds with various halogens. We also demonstrated that SPS is an effective technique to reduce the interfacial impedance and also the overall activation energy of the solid-state electrolyte. We found the bulk conductivity of Na_3OBr to be on the order of 10_{-7} S cm^{-1} at 180°C regardless of the processing technique used. From DFT calculations we conclude that ion diffusion-mediating defects in the material are associated with high formation energies, much higher than in LiRAPs. Future work to increase the ionic conductivity of NaRAP should involve a combination of aliovalent and isovalent substitutions in conjunction with advanced processing such as SPS.

Chapter 3, in full, is a reprint of the material "Experimental and Computational Evaluation of a Sodium-Rich Anti-Perovskite for Solid State Electrolytes" as it appears in the Journal of the Electrochemical Society, H. Nguyen, S. Hy, E. Wu, Z. Deng, M. Samiee, T. Yersak, J. Luo, S. P. Ong, and Y. S. Meng, 2016, 163, 10, A2165-A2171. The dissertation author was co-primary investigator and author of this paper. The author performed all the experimental work and electrochemical tests. Both Deng and the author designed and analyzed, and wrote the results.

Chapter 4 Insights into the Performance Limits of the $Li_7P_3S_{11}$ Superionic Conductor: A Combined First-Principles and Experimental Study

4.1. Introduction

Rechargeable all-solid-state lithium-ion batteries utilizing a fast lithium superionic conductor electrolyte (SCE)[62–66] have the potential to revolutionize energy storage by providing an inherently safer, less flammable alternative to traditional organic electrolyte-based batteries.[67–69] The discovery of the $Li_{10}GeP_2S_{12}$[64,70] and $Li_7P_3S_{11}$[65,66,71–74] glass-ceramic conductors have provided further optimism that SCEs with Li^+ conductivities rivaling that of organic solvents exist. In particular, a room-temperature ionic conductivity of 17 mS cm^{-1} has been achieved in the $Li_7P_3S_{11}$ glass-ceramic,[66] which is the highest ionic conductivity observed for a SCE thus far.

$Li_7P_3S_{11}$ crystallizes in a triclinic structure with space group of $P\bar{1}$ (Int. No. 2),[65] as illustrated in Figure 1. All Li sites are fully occupied, with phosphorus and sulfur atoms forming individual PS_4 tetrahedra or S-sharing P_2S_7 ditetrahedra. The primitive cell consists of two formula units with seven symmetrically distinct lithium sites.

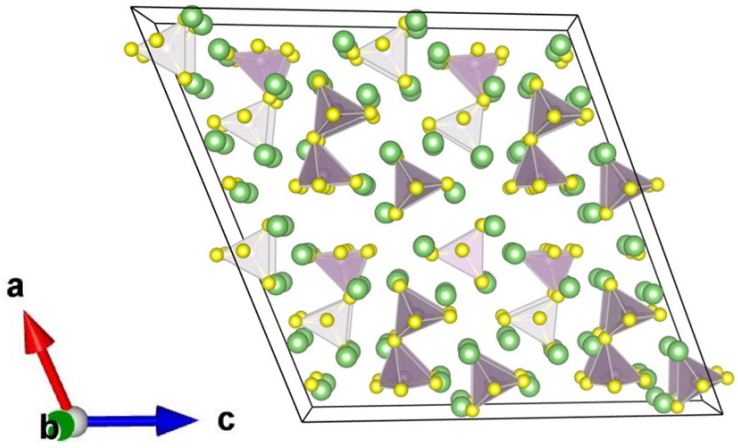

Figure 4.1. Crystal structure of a 2 × 2 × 2 supercell of $Li_7P_3S_{11}$. The tetrahedra are PS_4, and Li and S atoms are labeled with green and yellow spheres, respectively.

$Li_7P_3S_{11}$ was first reported by Mizuno et al. as the metastable crystal precipitated from $70Li_2S{\cdot}30P_2S_5$, with a room-temperature ionic conductivity of 3.2 mS cm^{-1}.[71,72] Its crystal structure was subsequently characterized by Yamane and co-workers.[65] Further optimization of heat treatment and high-pressure conditions during the synthesis process by Seino and co-workers produced a material with a room-temperature ionic conductivity of 17 mS cm^{-1}, [66] which they attributed to the reduction of grain boundary impedance and thus reducing overall cell resistance. Such ionic conductivity even exceeds that of the $Li_{10}GeP_2S_{12}$ family of electrolytes.[64,70,75–77] On the computational front, Onodera et al.[78,79] applied the reverse Monte Carlo (RMC) approach and found that the lithium ionic conduction pathway, formed by LiS_4 tetrahedra linked with vacant S_4 tetrahedra, can be remarkably long. They hypothesized that the large number of vacant S_4 tetrahedra surrounding the Li ions is the origin of the high ionic conductivity in this compound. Lepley and Holzwarth[80] also carried out a density functional theory (DFT) study of $Li_7P_3S_{11}$ and concluded that it is metastable and that the migration barrier along the b crystallographic direction (around 150 meV) is lower than along the other two crystallographic directions. In this work, we build on the existing body of knowledge on the highly promising $Li_7P_3S_{11}$ SCE and present a comprehensive computational and experimental investigation of the performance limits of this material in terms of its phase and electrochemical stability, and Li^+ conductivity. We show that $Li_7P_3S_{11}$ is entropically stabilized at temperatures above 630 K (~360 °C) and tends to form relatively isotropic crystals. We demonstrate that the synthesis approach has a significant effect on the overall conductivity but only a small effect on measured activation energies. While a densification process experimentally observed a significant increase in conductivity from 1.3 to 11.6 mS cm^{-1}, ab initio molecular dynamics simulations predict $Li_7P_3S_{11}$ to have an even higher bulk room temperature Li^+ conductivity of

57 mS cm^{-1}. We also discuss the role of ionic motion correlation and the framework structure in facilitating fast Li^+ diffusion.

4.2 Computational Methods and Details

All calculations were performed using the Vienna ab initio simulation package (VASP)[45] under the projector augmented wave approach.[46]A structural optimization of the experimental $Li_7P_3S_{11}$ structure was first carried out[65] and the fully relaxed structure was used in the subsequent calculations. Unless otherwise indicated, all calculations were spin- polarized and utilized the Perdew−Burke−Ernzerhof (PBE) generalized-gradient approximation (GGA)[47] exchange-correlation functional, a kinetic energy cutoff of 520 eV, and a Monkhorst−Pack k-mesh[81] with density of 1000/(number of atoms in the unit cell). All analyses were performed using the Python Materials Genomics (pymatgen) library.[50]

4.2.1. Phase Stability

The Li−P−S phase diagram at 0 K was constructed by determining the convex hull[82] of the composition- energy coordinates of all $Li_xP_yS_z$ compounds. Precomputed data were obtained from the Materials Project (MP)[48] using the Materials API.[49] The energy difference between the $Li_7P_3S_{11}$ phase and the predicted phase equilibria, also known as the energy above the hull (Ehull), was evaluated.[82] The E_{hull} is always non-negative and becomes zero for stable compounds. The higher the E_{hull}, the less stable the compound is predicted to be. A constant energy correction of −0.66 eV per S atom, which is similar to the scheme proposed by Wang et al.[83] for the O_2 molecule, was applied to the elemental sulfur energy.[84]

4.2.2. Dynamical Stability

Phonon calculations were carried out with a 1 × 2 × 1 supercell of $Li_7P_3S_{11}$ using the Phonopy package.[85] Real- space force constants associated with the atoms in the supercell were

first computed within the framework of density-functional perturba- tion theory (DFPT),[86] and the phonon spectrum was then obtained by solving the dynamical matrices of various high-symmetry wave vectors. Thermodynamic quantities such as Gibbs free energy and vibrational entropy were computed from the phonon spectrum (see Appendix A for supporting information) for details).

4.2.3. Electrochemical Stability

The electrochemical stability of the SCEs in contact with the electrodes was estimated using two thermodynamic approximations. (1) The first approximation is based on the previous work by Ong et al.,[75] which assumes that Li is the main mobile species. Under such conditions, the SCE−electrode interface can be modeled as an open system with respect to Li. The relevant thermodynamic potential is then the grand potential, given as $\phi = E - \mu Li\ NLi$, where E, NLi, and μLi are respectively the internal energy, the number of Li atoms in the open system, and the Li chemical potential. The SCE−anode interface is modeled as the SCE material at high $\mu Li \approx \mu^0_{Li}$, and the SCE− cathode interface is modeled as the SCE material at low $\mu_{Li} \approx \mu^0_{Li} - 5$ eV. Here, μ^0_{Li} is the energy of metallic Li. (2) The second approximation assumes full thermodynamic equilibrium between the SCE and electrode in varying ratios. In essence, the pseudobinary phase diagram between SCE and electrode is constructed to identify the stable phase equilibria. This methodology is similar in spirit with previous work by Miara et al.,[87] but, in our approach, there is no assumption of the alkali ion being the dominant mobile species and composition conservation is enforced for all species. We believe this approach is more reflective of the conditions during actual synthesis and assembly conditions.

4.2.4. Electronic Structure

The band gap of an SCE serves as a measure of its electronic conductivity, as well as an upper limit for its intrinsic electrochemical window.[88] We performed electronic structure calculations using the Heyd−Scuseria−Ernzerhof (HSE) hybrid functional,[89,90] which has been shown to be significantly more accurate at predicting band gaps compared to semi-local functionals.[91] Due to the higher computational load compared to PBE calculations, a reduced Monkhorst−Pack k-mesh 2 × 4 × 2 was adopted instead.

4.2.5. Surface Energies and Wulff Shape

The surface energies for all surfaces with maximum index of 2 of $Li_7P_3S_{11}$ were calculated using the following expression:

$$\gamma = \frac{E_s - E_b}{2A} \quad (1)$$

where E_s and E_b represent the total energy of the slab and bulk, respectively, and A is the surface area. The normal width of the slab was set to at least 10 Å, and a 10 Å vacuum layer was added in the calculation to minimize interactions between periodic images. We further impose the conditions that PS_4^{3-} and $P_2S_7^{4-}$ polyhedra with highly covalent P−S bonds must remain intact, and only nonpolar surfaces were calculated. The equilibrium morphology of the $Li_7P_3S_{11}$ crystal was determined from the surface energies via the Wulff construction.[92]

4.2.6. Diffusivity and Ionic Conductivity

The diffusivity and conductivity of $Li_7P_3S_{11}$ were calculated using non-spin-polarized ab initio molecular dynamics (AIMD) simulations. A smaller plane-wave energy cutoff was selected as 280 eV. A 1 × 2 × 1 supercell along with a minimal Γ-centered 1 × 1 × 1 k-mesh were adopted. The time step was set to 2 fs. The simulation setup is similar to previous work by the authors.[31] The diffusivity was then obtained by performing a linear fitting of the mean square

displacement (MSD) with time. Diffusivities were obtained at temperatures between 400 K and 1200 K in 100 K increments. Then an Arrhenius plot of ionic conductivity (σ(T)), as computed using the resulting diffusivities (D(T)) via the Nernst− Einstein relation, 2

$$\sigma(T)T = \frac{\rho z^2 F^2}{R} D(T) \quad (2)$$

was generated and used to determine the activation energy (Ea). Here, ρ is the molar density of diffusing ions in the unit cell. F, R, and z are the Faraday constant, the gas constant, and the charge of lithium ions that equals +1, respectively. A linear extrapolation was made to obtain the room-temperature conductivity. To analyze the correlations between ion motions, we calculated the self and distinct parts of the van Hove correlation function from the AIMD trajectories, as detailed in our recent work.[84] A detailed description of these methods is also provided in the SI. We also investigated the Li^+ diffusion pathways by calculating the probability density distribution, which is defined on a uniform 3D grid in the unit cell (Ω) and obtained by ensemble averaging over the Li^+ ionic trajectories of AIMD in conjunction with $\int_\Omega P(r)dr = 1.29$ The van Hove and also the diffusion pathway analyses were performed using the pymatgen-diffusion add-on to pymatgen.[39]

4.3 Experimental Methods

4.3.1 Synthesis

$70Li_2S{\cdot}30P_2S_5$ glass was synthesized from reagent-grade chemicals, P2S5 (Sigma-Aldrich, 99%) and Li_2S (Sigma-Aldrich 99.98%). Stoichiometric amounts of these chemicals were mixed and sealed in a quartz ampoule and heated at 973 K (700 °C) for 4 h. The molten sample was then quenched to room temperature in ice water. Subsequently, the resulting glass was ground for 30 min with an agate mortar and pestle into a glass powder. For the cold-pressed sample, the glass powder was sealed in a quartz ampoule, heated at 573 K (300 °C) for 2 h, and

then quenched to room temperature in ice water. For the spark-plasma-sintered (SPS) samples, the glass powder was loaded into 10 mm tungsten−carbide dies, lined with a graphite sheet and pressed lightly. The loaded die was placed into the SPS chamber and pressed to a preload pressure of 10 MPa. The heating and pressure profiles were as follows: 573 K (300 °C) at a rate of 100 K min^{-1} and 300 MPa at a rate of 100 MPa min^{-1}. The temperature and applied pressure dwell times were 5 min. The experiment was conducted under flowing argon gas.

4.3.2. Characterization

Cross-sectional images of cold-pressed and SPS samples were collected with Phillips XL30 scanning electron microscopy (SEM). A thin film of iridium was coated onto the electronically insulating materials for use in the SEM. Iridium was sputtered onto the electrolyte materials by using an Emitech sputter coater for 7s, with a current of 8 μA. SEM images were collected with an applied voltage of 20 kV. X-ray diffraction (XRD) data of glass and glass-ceramic were collected by Rigaku diffractometer, using Cu K_α radiation. The scan range was 10°−70°. The glass-transition temperature (T_g) and the glass-ceramic crystallization temperature (Tc) were determined by differential scanning calorimetry (DSC; PerkinElmer Pyris Diamond). The temperature range was from room temperature to 673 K (400 °C) with a scan rate of 10 K min^{-1}. The glass material was hermetically sealed in aluminum pans, and measurements were conducted under argon purging.

4.3.3. Electrochemical Measurements

Ionic conductivities were measured using electrochemical impedance spectroscopy (EIS) with an impedance analyzer (Solartron 1260) in the frequency range of 1 MHz to 1 Hz with an applied AC voltage of 25 mV. The diameters of the cold-pressed pellets and the SPS pellets were 13 mm and 10 mm, respectively. Cold-pressed pellets were pressed using 5 metric ton while SPS

pellets were used as is. Carbon paste was attached to both sides of the pellets as electrodes, and stainless steel plates were used as current collectors.

High-temperature conductivity measurements on the cold-pressed and SPS pellets were collected by heating the pellets in an electric furnace from room temperature to 453 K in 25 K increments. The solid electrolyte cell was heated in the electric furnace at a rate of 10 K min^{-1} to avoid temperature overshoot. Conductivity measurements were made after the cell had dwelled at the desired temperature for 1 h. The activation energy (E_a) for Li-ion diffusion was obtained from the Arrhenius plot. All measurements and heating were conducted in an Ar atmosphere.

4.4. Results

4.4.1 Crystal Structure and Characterization

Panels a and b of Figure 2 show the SEM images of $Li_7P_3S_{11}$ crystals obtained from the cold-pressed and SPS heat treatment processes, respectively. It is clear that the morphology of the cold-pressed pellet is highly granular and contains a network of open pores, which is in contrast to the morphology of the SPS made pellets that exhibit much smoother surfaces. This is in line with the previous experimental report.[66] Figure 2c shows the XRD patterns for the glass powder, cold- pressed glass-ceramic, and SPS glass-ceramic. The bottom curve shows the pattern of the melt-quenched precursors. No crystalline peaks from the two starting materials are present, and an amorphous glass phase is achieved when the molten material is quenched in ice water. Subsequent heat treatment of the glass phase material to form the glass-ceramic shows the $Li_7P_3S_{11}$ phase formed in both cold-pressed-sintered and SPS samples. The peaks observed in the cold-pressed-sintered and SPS glass-ceramics are identified as the glass-ceramic $Li_7P_3S_{11}$, which are in excellent agreement with the reported crystal structure by Yamane et al.[65] A comparison of the cell parameters estimated via XRD refinement and from DFT calculations in this work with

previous experimental values in the literature is given in Table 1. Our experimental lattice parameters are in good agreement with previous works,[65,78]while the PBE calculated lattice parameters are consistently overestimated by 1−3% compared to the experimental values, which can be attributed to the well-known tendency for GGA functionals to underbind.

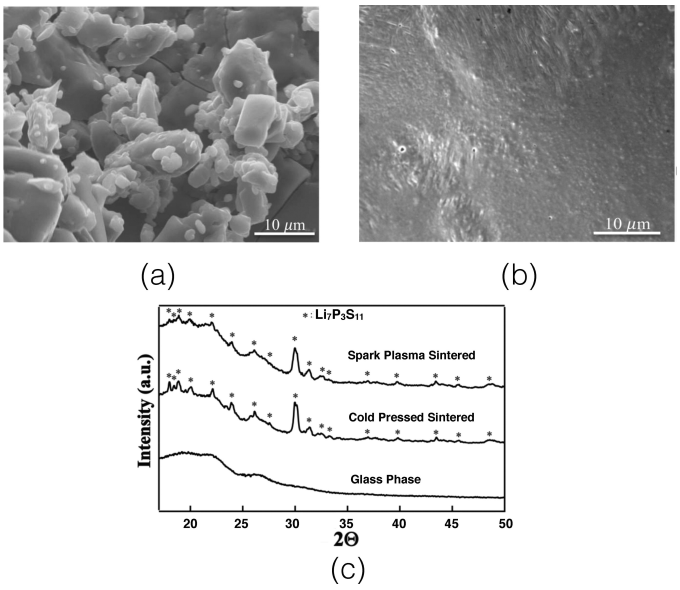

Figure 4.2. SEM images of (a) cold-pressed and (b) SPS $Li_7P_3S_{11}$ glass-ceramics. (c) XRD patterns of $70Li_2S{\cdot}30P_2S_5$ glass sintered by conventional methods and SPS

Table 4.1. Cell Parameters of Li7P3S11 reported in previous experimental studies and this work.

a (Å)	b (Å)	c (Å)	α (deg)	β (deg)	γ (deg)	
12.501	6.032	12.530	102.845	113.202	74.467	Ref. [65]
12.483	6.031	12.499	102.906	113.304	74.495	Ref. [78]
12.586	6.061	12.607	102.937	113.166	74.756	SPS, this work
12.493	6.030	12.532	102.834	113.265	74.524	CP, this work
12.480	6.200	12.640	103.720	113.780	74.090	DFT-PBE, this work

4.4.2. Phase Stability

Figure 3 shows the calculated Li−P−S phase diagrams at 0 K. Regardless of whether a sulfur correction is applied, $Li_7P_3S_{11}$ is predicted to be metastable at 0 K. However, the predicted phase equilibria at the $Li_7P_3S_{11}$ composition depends on whether the sulfur correction is applied. In the absence of a sulfur correction, the predicted phase equilibrium is

$$Li_7P_3S_{11} \rightarrow Li_3PS_4 + Li_4P_2S_6 + S \quad (3)$$

and $Li_7P_3S_{11}$ is predicted to have an Ehull of 27 meV/atom. This result is consistent with the previous work by Lepley et al.[80] Here, Li_3PS_4 refers to the γ phase (Pmn21; ICSD id, 180318), which is energetically more stable at low temperatures, and $Li_4P_2S_6$ has space group $P6_3/mcm$ (ICSD id, 33506). For $Li_4P_2S_6$, we performed an enumeration of the disordered ICSD structure and used the lowest energy ordering in computing the phase diagrams. With the incorporation of the sulfur correction, however, the local phase triangles change and the predicted phase equilibria is given by the following reaction:

$$3Li_7P_3S_{11} \rightarrow 7Li_3PS_4 + P_2S_5 \quad (4)$$

and $Li_7P_3S_{11}$ is predicted to have an Ehull of 21 meV/atom. Here, P_2S_5 refers to the lowest energy phase in the MP database, which has space group $P\bar{1}$ and ICSD id 409061.

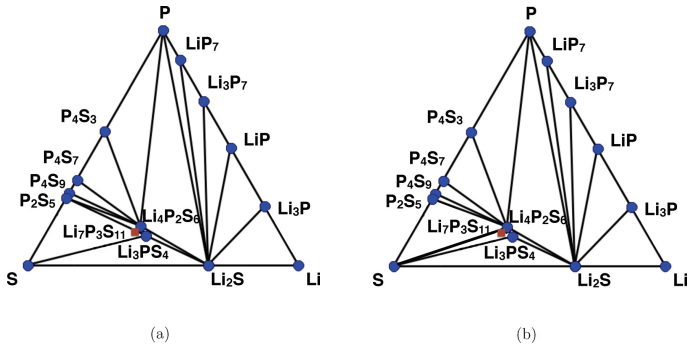

Figure 4.3. Li–P–S phase diagram at zero temperature (a) with and (b) without sulfur energy correction. Stable compounds are indicated as blue dots, whereas the metastable Li_7P3S_{11} is labeled with a brown square.

To estimate the transition temperature at which $Li_7P_3S_{11}$ becomes thermodynamically stable, the vibrational contributions to the entropy were estimated by computing the phonon spectra for $Li_7P_3S_{11}$, Li_3PS_4 and P_2S_5 (see Figure A1 in the Appendix). Figure 4a plots the Gibbs free energy change of the reverse of reaction (4), ΔG(T), with respect to temperature. It can be observed that the free energy change becomes negative at temperatures greater than 630 K (~360 °C), which corresponds to the transition temperature. Figure 4b shows the DSC measurement of $Li_7P_3S_{11}$. A shift in the baseline at around 518 K (245 °C) indicates that the material underwent a glass transition at Tg. Upon further heating, the crystallization temperature (Tc) was observed around 553 K (280 °C) and was followed by another shift in the baseline measurement, indicative of a change in heat capacity. The crystalline phase that was formed slightly above T_c was identified with XRD and found to be the metastable $Li_7P_3S_{11}$ crystal. Overall, the computed transition temperature of 630 K (~360 °C) is in excellent agreement with the measured crystallization temperature of $Li_7P_3S_{11}$ of 553 K (280 °C), as well as that reported previously.[66]

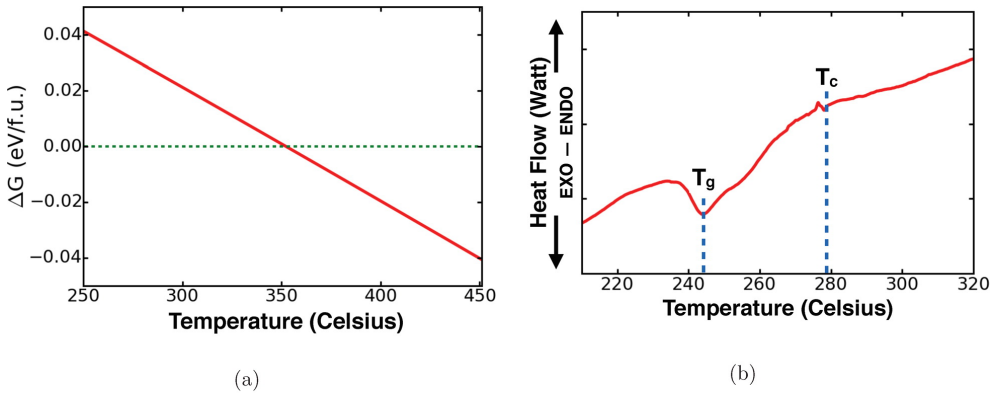

Figure 4.4. (a) Gibbs free energy change from P_2S_5 and Li_3PS_4 to $Li_7P_3S_{11}$ (Δ*G*; eV per formula unit of $Li_7P_3S_{11}$) as a function of temperature (red solid). The green dashed line indicates zero Δ*G*. (b) Experimental DSC curve of $70Li_2S{\cdot}30P_2S_5$ glass. Blue dashed lines denote the glass-transition temperature (T_g) and crystallization temperature (T_c).

4.4.3. Electrochemical Stability

The lithium grand potential phase diagrams at $\mu_{Li} = \mu_{Li}^0$ and $\mu_{Li}^0 - 5$ eV, corresponding to the $Li_7P_3S_{11}$ interface with a Li metal anode and a 5 V charged cathode environment, respectively, are given in Figure A2 in the SI. We find that, in the limit of fast Li mobility, the phase equilibria at the Li anode comprise Li_3P and Li_2S, whereas P_2S_5 and S are found at the 5 V charged cathode. We also investigated the possible compounds formed at the $Li_7P_3S_{11}$/electrode interfaces with varying compositional ratios. Figure 5 shows the pseudobinary phase diagrams and phase equilibria (in Table 3.2) that depend on the ratio between $Li_7P_3S_{11}$ and (a) a CoO_2 charged cathode, (b) a $LiCoO_2$ discharged cathode, or (c) a Li metal anode. At the $Li_7P_3S_{11}$/ Li interface, we find that the predicted phase equilibria comprise γ-Li_3PS_4, $Li_4P_2S_6$, Li_2S, and Li_xP_y compounds, which are all reasonable ionic conductors and poor electronic conductors that may form the basis of a good passivation layer. We also note that the phase equilibria at G in Figure 5c is in line with that predicted by the lithium grand potential approach. This is expected because Li is the only mobile species at the Li anode, and G corresponds to $Li_7P_3S_{11}$ reacting with an excess of Li.

Table 4.2. Phase equilibria of $Li_7P_3S_{11}$ at (a) CoO_2 charged cathode, (b) $LiCoO_2$ discharged cathode, and (c) metallic lithium as labeled in Figure 5.

label	x	phase equilibria
(a) CoO_2		
A	0.8235	0.8235 $\underline{CoS_2}$+ 0.0588 P_2S_5 + 0.4118 Li_3PO_4
B	0.8462	0.8462 $\underline{CoS_2}$+ 0.1538 $Li_4P_2O_7$ + 0.1538 Li_3PO_4
C	0.8696	0.1739 $LiCoPO_4$ + 0.6957 $\underline{CoS_2}$+ 0.0435 Li_2SO_4 + 0.2174 Li_3PO_4
D	0.9067	0.2667 $LiCoPO_4$ + 0.2133 $\underline{Co_3S_4}$+ 0.1733 Li_2SO_4 + 0.0133 Li_3PO_4
E	0.9091	0.2727 $LiCoPO_4$ + 0.0076 $\underline{Co_9S_8}$+ 0.1894 $\underline{Co_3S_4}$+ 0.1818 Li_2SO_4
F	0.9283	0.1055 $Co_3(PO_4)_2$ + 0.0042 $LiCoPO_4$ + 0.0675 $\underline{Co_9S_8}$+ 0.2489 Li_2SO_4
G	0.9289	0.1067 $Co_3(PO_4)_2$ + 0.0089 CoO + 0.0667 $\underline{Co_9S_8}$+ 0.2489 Li_2SO_4
H	0.9778	0.0333 $Co_3(PO_4)_2$ + 0.7111 CoO + 0.1667 $CoSO_4$ + 0.0778 Li_2SO_4
I	0.9836	0.0246 $Co_3(PO_4)_2$ + 0.2623 $\underline{Co_3O_4}$+ 0.1230 $CoSO_4$ + 0.0574 Li_2SO_4
J	0.9844	0.0469 $CoPO_4$ + 0.2734 $\underline{Co_3O_4}$+ 0.1172 $CoSO_4$ + 0.0547 Li_2SO_4
(b) $LiCoO_2$		
A	0.5000	0.5000 $\underline{CoS_2}$+ 0.2500 $Li_4P_2S_6$ + 0.7500 Li_3PS_4 + 0.2500 Li_3PO_4
B	0.6667	0.1667 $\underline{CoS_2}$+ 0.6667 Li_3PS_4 + 0.1667 $\underline{Co_3S_4}$+ 0.3333 Li_3PO_4
C	0.8571	0.2143 $\underline{CoS_2}$+ 0.2857 Li_2S + 0.2143 $\underline{Co_3S_4}$+ 0.4286 Li_3PO_4
D	0.8675	0.2651 Li_2S + 0.2892 $\underline{Co_3S_4}$+ 0.0361 Li_2SO_4 + 0.3976 Li_3PO_4
E	0.8963	0.2075 Li_2S + 0.0996 $\underline{Co_9S_8}$+ 0.1369 Li_2SO_4 + 0.3112 Li_3PO_4
F	0.9135	0.1015 $\underline{Co_9S_8}$+ 0.2307 Li_2O + 0.1396 Li_2SO_4 + 0.2595 Li_3PO_4
G	0.9196	0.0804 Li_6CoO_4 + 0.0932 $\underline{Co_9S_8}$+ 0.1383 Li_2SO_4 + 0.2412 Li_3PO_4
H	0.9677	0.0323 Li_6CoO_4 + 0.3548 Li_2SO_4 + 0.0968 Li_3PO_4 + 0.9355 $\underline{Co}$
I	0.9888	0.1199 Li_6CoO_4 + 0.8689 CoO + 0.1236 Li_2SO_4 + 0.0337 Li_3PO_4
(c) Li		
A	0.5000	1.0000 Li_3PS_4 + 0.2500 $Li_4P_2S_6$
B	0.7500	0.3750 $Li_4P_2S_6$ + 0.5000 Li_2S
C	0.9375	0.6875 Li_2S + 0.1875 P
D	0.9391	0.0261 LiP_7 + 0.6696 Li_2S
E	0.9421	0.0248 Li_3P_7 + 0.6364 Li_2S
F	0.9474	0.1579 LiP + 0.5789 Li_2S
G	0.9600	0.1200 Li_3P + 0.4400 Li_2S

[a]Poor electronic insulators are indicated with an underline.

However, at the $Li_7P_3S_{11}$/cathode interface, the predicted equilibrium phases depend strongly on the particular stoichiometry and cathode chemistry. The presence of products that involve Co, P, or S is consistent with previous experimental findings, where the mutual diffusions of Co, P, and S were observed at the interface formed between a $Li_2S-P_2S_5$ glass and $LiCoO_2$.[93]The formation of cobalt sulfides (e.g.,Co_3S_4) near the $Li_7P_3S_{11}/LiCoO_2$ interface also agrees well with a recent experimental report.[72] In general, we find that the $Li_7P_3S_{11}$/ $LiCoO_2$ interface phase equilibria contain poor electronic insulators (e.g., Co and Co_3O_4 and Co_9S_8)[94,95]in either the charged or discharged state. Unlike $LiCoO_2$, the interfaces between SCEs and other common electrode materials such as the olivine $LiFePO_4$ and spinel $LiMn_2O_4$ are much less studied. Using the same methodology, we investigated the phase equilibria between $Li_7P_3S_{11}$ and

the charged olivine $FePO_4$ (Figure A3 in the SI) and charged spinel Mn_2O_4 (Figure A5 in the SI) cathodes. Although poor electronic insulators such as FeS_2 and MnS_2 appear at certain cathode/SCE ratios x, the phases formed close to the cathode, i.e., with largest values of x, are all fully electronically insulating phases, which may form good passivation layers against further reactions.

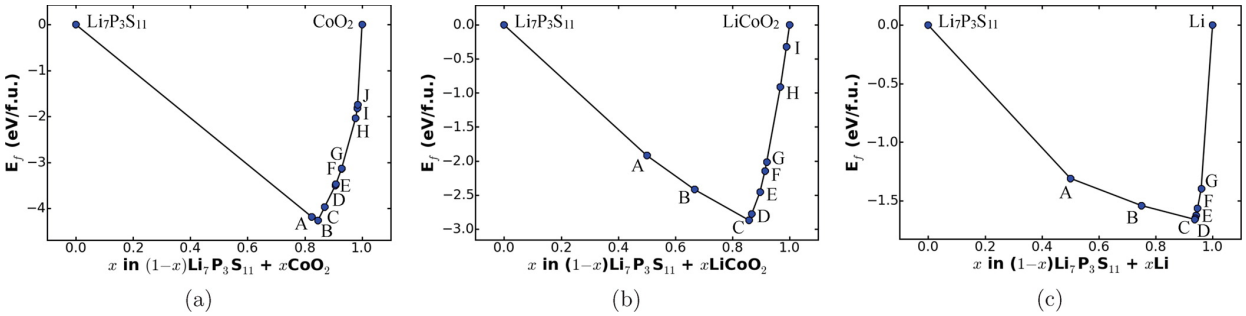

Figure 4.5. Pseudobinary phase diagrams between (a) $Li_7P_3S_{11}$ and CoO_2 charged cathode, (b) $Li_7P_3S_{11}$ and $LiCoO_2$ discharged cathode, and (c) $Li_7P_3S_{11}$ and metallic Li anode. Labeled reactions in the panels are given in Table 2.

4.4.4. Electronic Structure

The electronic band gap, which can be obtained from electronic structure calculations, is often considered as the upper bound of the intrinsic electrochemical window for the SCE studied. The electronic band structure of $Li_7P_3S_{11}$ is illustrated in Figure 6a. A minimum band gap of 3.9 eV is found to be indirect from X to N, which suggests that $Li_7P_3S_{11}$ is a wide band gap insulator. Our calculated band gap also agrees with the value of 3.5 eV previously calculated by Xiong et al.[96] Figure 3.6b displays the stacked projected density of states of the compound. The valence band maximum is mainly contributed to by the p states in S, whereas the p states in both P and S mostly contribute to the conduction band minimum. We have also compared the electronic structure of $Li_7P_3S_{11}$ calculated using the PBE functional to that calculated with the HSE functional. In general, the electronic structure is similar between the two functionals, except that

the PBE band gap is significantly smaller at 2.6 eV, which agrees with the value of 2.1 eV by Xiong et al.[96]

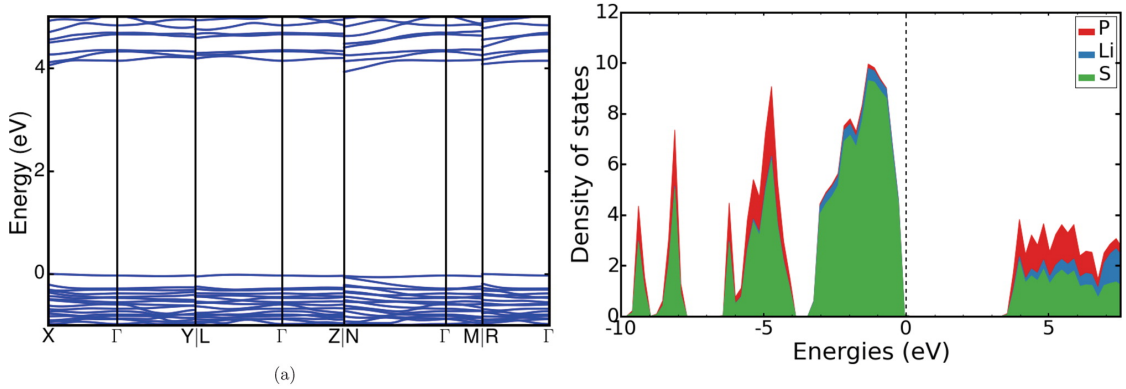

Figure 4.6. (a) Electronic band structure and (b) electronic stacked projected density of states of Li7P3S11 using HSE hybrid functionals.

3.4.5. Surface Energies and Wulff Shape

Figure 7 shows the calculated Wulff shape and surface energies of the six low-index orientations for $Li_7P_3S_{11}$. The (100), (10$\bar{1}$), and (010) surfaces are the most stable with surface energies of 0.1, 0.12, and 0.16 J/m^2, respectively. Using the obtained surface energies, the Wulff construction of $Li_7P_3S_{11}$ was carried out for the equilibrium morphology of $Li_7P_3S_{11}$ crystal, as shown in Figure 7. The relative area contributions $p(n)= A_n/A_{tot}$ for the six orientations n were also estimated. Here, $A_{tot} = \sum nA_n$ is the total surface area over the six orientations n.

Three orientations, (100), (10$\bar{1}$), and (010) contribute more than 90% of the total surface area of the Wulff shape. The calculated Wulff shape is in good qualitative agreement with our cold-pressed sample (Figure 2a), which shows large relatively isotropic crystals with few facets.

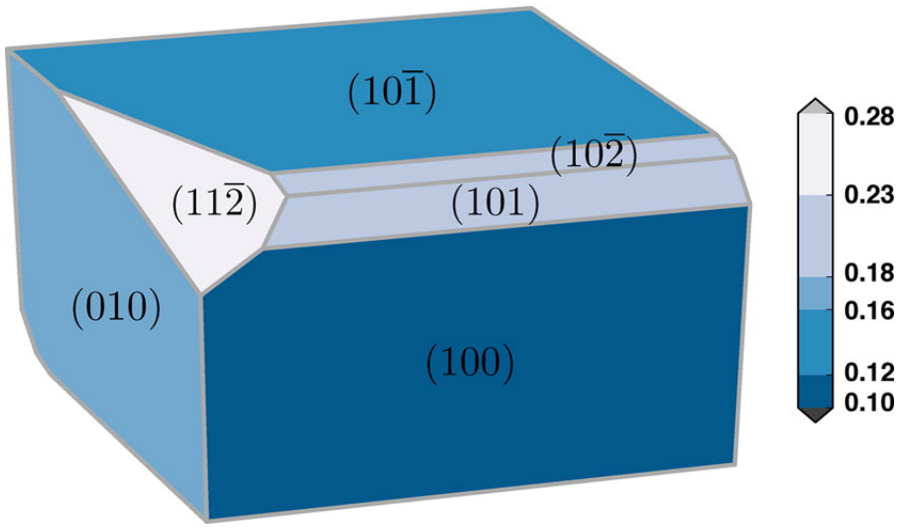

Figure 4.7. Wulff shape of $Li_7P_3S_{11}$ constructed using the six low-index surfaces. The values given at the color bar are the energy scale of the surface in J/m^2. The relative area contributions of the (100), (10$\bar{1}$), and (010) surfaces are 38%, 29%, and 25%, respectively.

4.4.5. Li^+ Conductivity

The theoretically calculated and experimentally measured Arrhenius plot for $Li_7P_3S_{11}$ is shown together in Figure 3.8a. For the experimentally measured Arrhenius plot, electrochemical impedance measurements were conducted where the Arrhenius behavior was calculated by using the real-axis impedance intercept in the Nyquist plot as the total impedance (see Figure A7 and A8 in the SI). The activation energy (E_a) extracted from the theoretically calculated fitting is 187 meV, in excellent agreement with experimental value of 180 meV for the SPS sample (209 meV for the cold-pressed sample). The theoretical room temperature diffusivity (D(T=300K)) is obtained by linear extrapolation and is found to be 5.7×10^{-7} cm^2/s. This is in line with the previous Li-ion diffusion measurements using the pulsed- gradient spin−echo (PGSE) nuclear magnetic resonance (NMR) technique, where the Li-ion diffusivity is $10^{-8} - 10^{-7}$ cm^2/s at temperatures of 303−353 K.[97] It is worth pointing out that, in the AIMD calculations at 700 K or below, the one- dimensional MSD along the b-axis is nearly a factor of 2 higher than along the

other two axes, which is consistent with the nudged elastic band results of Lepley and Holzwarth.[80] The corresponding room-temperature ionic conductivity (σ- (T=300K)) is evaluated as 57 mS cm^{-1}, and the estimated error bar is between 50 and 65 mS cm^{-1}. For the experimentally obtained values, there is a significant increase of σ(T=300K) from the cold-press-sintered (1.3 mS cm^{-1}) to the SPS pellet (11.6 mS cm^{-1}). This increase in conductivity is similar to the densified $Li_7P_3S_{11}$ pellets obtained via hot-press sintering (17 mS cm^{-1}).[5] However, the measured ionic conductivity is significantly lower than the one derived from the AIMD simulations. We will discuss the reasons for this discrepancy in Discussion. We note that the lattice parameters predicted by the PBE functional are about 3% higher than the experimental values. To exclude functional limitations as a potential source of error, we also performed a full relaxation and AIMD simulation using the PBEsol functional, which is known to provide much more accurate predictions of lattice parameters.[98] The PBEsol lattice parameters differ from the experimental values by only 1%, but the extrapolated room- temperature conductivity is 60.5 mS cm^{-1}, which is very close to the PBE value.

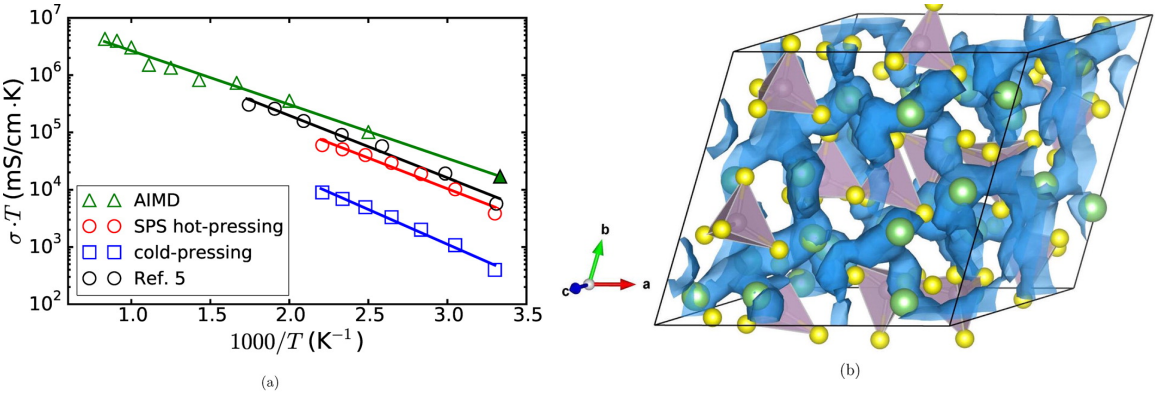

Figure 4.8. (a) Arrhenius plots of $Li_7P_3S_{11}$ obtained from AIMD simulations (green triangles) and conductivity measurements of cold-pressed sample (blue squares) and SPS hot-pressed sample (red circles). The Arrhenius plot by Seino et al.(5) that shows the highest room-temperature ionic conductivity of 17 mS cm^{-1} to date is also shown (black circles) for comparison. The filled triangle corresponds to the linearly extrapolated room-temperature conductivity from AIMD. (b) Isosurface of the probability density distribution (dark blue) $P(r)$ of Li^+ ions in $Li_7P_3S_{11}$ superionic conductor at 600 K, with $P = 0.001$.

4.4.6. Correlated Li^+ Motions and Framework Motions

Figure 3.8b shows the probability density distribution (P(r)) of Li^+ at 600 K. It is clear that the diffusion pathway forms a 3D network in which all of the Li^+ sites are connected to one another via empty S_4 tetrahedra. Given that the Li sites are fully occupied in this compound, this suggests that the Li ionic motion is highly collective, in agreement with previous experimental[97] and computational investigations.[99]This is also in contrast to other Li superionic conductors where defects (e.g., Li^+ vacancy) are required to facilitate the Li-ion diffusion.[31]

The van Hove correlation function (G), which can be divided into the self part (Gs) and the distinct part (Gd), is often adopted for investigating the highly correlated ionic motions. Figure 3.9a plots Gd for lithium after thermal equilibration in which a large magnitude of Gd is reached for r < 1 Å soon after t = 2 ps at 600 K. We relate this to the correlation time scale of the lithium-ion motions. This is also a strong indication of collective motions because for a given reference lithium ion at site r, it shows that other lithium ions move and occupy that site at later time moments when this reference ion diffuses away. Moreover, Gd is peaked but with smaller magnitude and more broadened for r between 3.5 and 4.5 Å, and also between 6 and 7 Å. The former is close to the shortest lithium−lithium distance in the initially relaxed atomic structure (see Figure A9). The presence of these peaks also implies that on average each lithium ion is surrounded by some of the other lithium ions during the entire diffusion process. Figure 9b shows the Gs for lithium as functions of r and t after thermal equilibration process at 600 K. It shows that Gs remains large for r <1 Å before t < 10 ps, and then its value decreases. This suggests that the lithium ions tend to diffuse away from their initial positions to neighboring lithium sites.

For comparison, the Gd and Gs plots for another superionic conductor $Li_{10}GeP_2S_{12}$ are presented in Figure 3.9c,d, respectively. As indicated in Figure 3.9c, we observe that the time scale of correlation in $Li_{10}GeP_2S_{12}$ is around 10 ps at 600 K, which is longer than that of $Li_7P_3S_{11}$. Similar to $Li_7P_3S_{11}$, there are two broadened peaks for r (i) between 3 and 5 Å and (ii) between 6 and 7 Å (see also Figure A10). The former region relates to the shortest lithium−lithium distance in the initially relaxed structure. Comparing the Gs, we may also note that Li^+ in $Li_{10}GeP_2S_{12}$ has a much higher probability of returning to their initial positions and staying there for longer time duration than in $Li_7P_3S_{11}$. These findings are consistent with the lower ionic conductivity of $Li_{10}GeP_2S_{12}$ compared to that of $Li_7P_3S_{11}$. We also investigated the motion of the framework ions in the AIMD trajectories. We find no evidence of framework melting at all temperatures. The P−S bond distances show very small fluctuations of <0.1 Å during the simulations, whereas S−S distances within the same tetrahedron show a slightly larger fluctuation of ~0.2 Å. S−S distance fluctuations become much larger for S in different tetrahedral. We also find that the P - bridging S−P bond angle in the P_2S_7 ditetrahedra fluctuates by around 5° in the simulations.

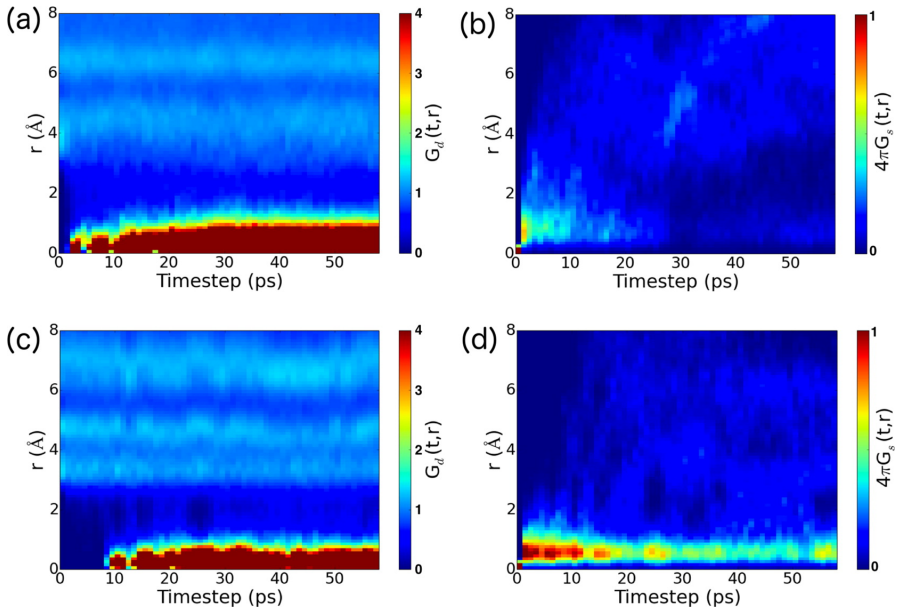

Figure 4.9. Distinct part of the van Hove correlation function (*G*d) for lithium in (a) $Li_7P_3S_{11}$ and (c) $Li_{10}GeP_2S_{12}$. The self-part of the van Hove correlation function (*G*s) for lithium in (b) $Li_7P_3S_{11}$ and (d) $Li_{10}GeP_2S_{12}$. Both *G*d and *G*s are functions of the average Li–Li pair distance *r* and time step after thermal equilibration at 600 K.

4.5 Discussion

In this work, we performed a comprehensive DFT and experimental investigation of the $Li_7P_3S_{11}$ glass-ceramic solid electrolyte. A good solid electrolyte must satisfy several criteria, namely, phase stability, a wide electrochemical stability, and a high Li^+ conductivity. In terms of stability, we find that though $Li_7P_3S_{11}$ is a metastable phase at 0 K, it becomes stable at above 630 K (~360 °C) when vibrational entropic contributions are taken into account. Our estimated transition temperature of 630 K (~360 °C) agrees well with the experimental crystallization temperature of 553 K (280 °C). However, the predicted phase equilibria of $Li_7P_3S_{11}$ depend significantly on the sulfur chemical potential. When a corrected sulfur energy (to reproduce experimental formation energies of sulfides) is used, the predicted phase equilibrium comprises γ-Li_3PS_4 and P_2S_5. When uncorrected sulfur energy is used, the phase equilibrium contains

$Li_4P_2S_6$ and S. The latter phase equilibrium is actually more consistent with previous experimental results, which found $Li_4P_2S_6$ as one of the primary decomposition products under certain synthesis conditions at >633 K (360 °C).[73] There are two reasons for this apparent discrepancy. First, $Li_4P_2S_6$ is a disordered structure, and thus may be entropically more stable at higher temperatures. Second, any sulfur loss at high temperatures would also result in the latter phase equilibrium becoming significantly more favorable, in line with Le Châtelier's principle. We believe that, at lower temperatures, the phase equilibria should indeed comprise the low-temperature γ-Li_3PS_4 and P_2S_5 phases. Furthermore, both $Li_4P_2S_6$ and Li_3PS_4 are observed during solid-state synthesis of $Li_2S{-}P_2S_5$ glass-ceramics.[73]

In agreement with previous DFT results of Zhu et al.,[100] we find that $Li_7P_3S_{11}$ is unlikely to be intrinsically stable against either the cathode or anode. At the Li metal anode, the predicted products formed are generally reasonable ionic conductors and poor electronic conductors that should form a good passivation layer. Somewhat surprisingly, it is the $Li_7P_3S_{11}$/cathode interface that might pose stability issues, depending on the cathode chemistry selected. For the olivine $LiFePO_4$ and spinel $LiMn_2O_4$, we find that the predicted phase equilibria for the $Li_7P_3S_{11}$/charged cathode interface contains fully electronic insulating, but ionic conducting, phases near the cathode. These phases are potential candidates for a good passivation layer, which can stabilize the cathode/$Li_7P_3S_{11}$ interface during battery operations. For the layered $LiCoO_2$ cathode on the other hand, we find that poor electronic insulators are present at all stoichiometry's, in agreement with previous experimental studies.[72] This suggests that the $Li_7P_3S_{11}$/$LiCoO_2$ interface is unstable against further propagation of the reaction front, and buffer layers such as $LiNbO_3$ need to be introduced to improve stability and improve rate capability.[101,102] To the authors' knowledge, there have been no extensive study done on the interactions between different cathode and SCE

chemistries. The DFT results show that the selection of the cathode chemistry is likely to be of critical importance in designing an all-solid-state battery.

The results of the AIMD simulations are somewhat surprising. Though there is excellent agreement between the computed and experimentally measured diffusion activation energy E_a, the extrapolated conductivity at 300 K of 57 mS cm^{-1} is a factor of 3−5 higher than the experimental values, which are between 11.6 and 17 mS cm^{-1}.[66] One possible explanation for this discrepancy is that there is a phase transition that occurs between 300 K and the temperatures of the AIMD simulations. However, the minimum temperature in our AIMD simulations is 400 K, one of the lowest temperatures ever performed for a solid-state conductor, and it is unlikely there is a phase transition between 300 and 400 K that would significantly alter the Li^+ diffusion behavior. Our hypothesis therefore is that the intrinsic bulk Li^+ conductivity of the $Li_7P_3S_{11}$ crystal is indeed significantly higher than the currently achieved conductivities thus far, and grain boundary limitations are responsible for the lower experimental conductivities. In fact, until recently, the ionic conductivity of $Li_7P_3S_{11}$ obtained in the experiments was only as high as 5.2 mS cm^{-1}.[74] It is through the reduction of grain boundary impedance by densification via hot-press sintering or SPS that the highest room-temperature conductivities have been achieved thus far for this material.[66] Another recent experiment also showed that further optimization of the glass-ceramic by reducing the amorphous glass phase detected via p-MAS could improve the overall conductivity of the material.[103] We further support this hypothesis with the observation that despite having fairly similar E_a, the measured conductivities of the cold-pressed and SPS samples differ by more than 1 order of magnitude. The highly granular morphology of the cold-pressed sample is expected to have significantly higher grain boundary resistance than that of the SPS made pellets. Given that the experimental and computed E_a are all

similar, we believe that the local structure and fundamental diffusion mechanisms are similar in both the amorphous grain boundary and the bulk phase. We speculate that the vastly different conductivities are therefore due to either a concentration effect from possible Li depletion at the grain boundaries or a difference in the hopping attempt frequency prefactor in the Arrhenius relation. The testing of these hypotheses will be the subject of future work.

We attempted to obtain further insights into the topological reasons for the high Li^+ conductivity of $Li_7P_3S_{11}$. Consistent with previous analyses,[78,79] the Li probability density distribution shows that Li^+ diffusion occurs through inter- connected S_4 tetrahedral sites. This tetrahedron-to-tetrahedron hopping in a bcc-like anion framework has been identified by Wang et al.[104] as a low-barrier mechanism. The van Hove correlation function analysis also highlights the highly correlated nature of the Li motion in $Li_7P_3S_{11}$, where the site vacated by a diffusing Li^+ is rapidly occupied by another Li^+, resulting in a significantly lower probability of a "back-hop" compared to $Li_{10}GeP_2S_{12}$. Also, the Gd of $Li_7P_3S_{11}$ is peaked at r between 3.5 and 4.5 Å during the time period studied, which corresponds to the average Li−Li separation during diffusion. This is in good agreement with a recent experimental measurement in which the jump length of Li ions during Li^+ migration is estimated at 4.3 Å.[99] Finally, we also find that although the framework PS_4 tends to remain relatively rigid throughout the simulations, significant flexing of the P_2S_7 ditetrahedra is observed. This is consistent with the recent experimental finding that the motional fluctuations of the framework polyhedrons contribute to the fast Li-ion diffusion.[5]

4.5 Conclusions

To conclude, we have performed a comprehensive computational and experimental investigation of the performance limits of the $Li_7P_3S_{11}$ superionic conductor. Our work has shed important insights into the phase and electrochemical stability and Li^+ conductivity in this

material. We find that the stability of the $Li_7P_3S_{11}$/cathode interface depends critically on the cathode chemistry. Unlike layered $LiCoO_2$ cathode, DFT calculations predict that the olivine $LiFePO_4$ and spinel $LiMn_2O_4$ cathodes are likely to form more stable passivation phases with $Li_7P_3S_{11}$. Furthermore, while significant increase from cold-press-sintered to SPS pellet was observed due to densification, the predicted bulk Li^+ conductivity of $Li_7P_3S_{11}$ is 57 mS cm^{-1}, significantly higher than the values achieved experimentally thus far. The significant difference in Li^+ of $Li_7P_3S_{11}$ synthesis via cold-pressed sintering and SPS shows that grain boundary conductivity is likely limiting the overall Li^+ conductivity in $Li_7P_3S_{11}$. Further optimization of overall Li^+ conductivities in $Li_7P_3S_{11}$ should therefore be possible.

Chapter 4, in full, is a reprint of the material "Insights into the Performance Limits of the $Li_7P_3S_{11}$ Superionic Conductor: A combined First-Principles and Experimental Study" as it appears in the Applied Materials & Interfaces, I.-H. Chu, H. Nguyen, S. Hy, Y.-C. Lin, Z. Wang, Z. Xu, Z. Deng, Y. S. Meng, and S. P. Ong, 2016, 8, 12, 7843-7853. The dissertation author was the co-primary investigator and author of this paper. The author performed all the experimental work and electrochemical tests. Both Chu and the author designed and analyzed, and wrote the results.

Chapter 5 Single-Step Synthesis of Highly Conductive Na_3PS_4 Solid Electrolyte for Sodium All Solid-State Batteries

5.1. Introduction

All solid-state batteries (ASSB) are regarded as a promising alternative to replace state-of-the-art liquid electrolyte-based batteries. This is due to their improved safety from the use of non-flammable components, wider operating temperature range, as well as the potential to achieve high energy density by enabling metallic anodes.[105] The key component of an ASSB is its solid electrolyte, which serves as a physical barrier between the cathode and anode, and allows transport of active ion(s) between them.

Despite the rich research history of solid-state electrolytes (SSEs) for energy storage and conversion materials applications,[106] widespread adoption of SSEs has fallen behind their liquid counterparts, mainly due to their inferior power capabilities and expensive processability. However, recent discoveries of some sulfide SSEs such as $Li_{10}GeP_2S_{12}$ and Na_3PS_4 are challenging this status quo. As a sulfide-based SSE, it can be synthesized and sintered at low temperatures compared to oxide-based analogs, significantly lowering the processing cost. Furthermore, with its power capabilities rivaling that of liquid electrolytes (>10 mS cm^{-1}), sulfide-based SSE are slated to front the future of energy storage technologies.[64]

Lithium-ion containing electrolytes are undoubtedly the most successful chemistries to date. However, taking material abundance into consideration, lithium sources are relatively limited and thus the lithium compounds are costly to produce. In contrast, sodium sources are considered virtually inexhaustible and readily accessible.[107,108] This makes sodium battery chemistries attractive and justifies their ongoing development mirroring that of lithium ion batteries.[109–115] Until recently, the most widely adopted sodium solid electrolytes are NASICON

and β-Alumina, with commercial applications of the latter in niche markets.[116–120] However, demands for high power and cheaper processing have made Na_3PS_4 a more promising solid-state electrolyte (SSE) candidate for energy storage and conversion applications.

The tetragonal polymorph Na_3PS_4, with the $P\bar{4}2_1c$ space group, was first studied in detail by Jansen et al. They suggested that a high temperature phase exists after observing a sharp change in the material's Arrhenius curve.[121] Hayashi et al. later stabilized this high temperature phase and determined it to be cubic Na_3PS_4, where they showed the superior sodium ion conductivity of cubic Na_3PS_4 compared to its tetragonal polymorph.[122] To achieve this, Hayashi et al. used ball milling to form an amorphous phase from crystalline precursors and subsequent heat treatment to stabilize the cubic Na_3PS_4 phase at room temperature. This two-step method, of ball milling followed by heat treatment represents the common general approach taken by almost all reports in the literature.[65–77] Table 1 summarizes all reported studies on Na_3PS_4 with their respective synthesis conditions. As shown in Table 1, there are still wide variations amongst its specific parameters, such as: precursor source, grinding media size and material, rotation speeds, milling time and heat treatment durations. As such, there is no established consensus on the parameters used to consistently achieve the desired properties of cubic Na_3PS_4, such as high conductivity on the order of 10^{-4} S cm^{-1}.

In this work, we systematically optimize synthesis conditions of Na_3PS_4 to produce the target phase and conductivity using a single-step synthesis technique. The synthesis conditions include total ball milling time, rotation speed, ball size, and secondary heat treatment. The results show that ball milling alone is sufficient to produce the Na_3PS_4 with the highest ionic conductivity. Using this material as a solid-state electrolyte, the TiS_2 cell is able to deliver 185 mAh g^{-1} and a modest capacity evolution with different current densities.

Table 5.1. Summarized synthesis conditions of the Na_3PS_4 solid electrolyte

Ball Mill Vendor	Na_2S Source	Media	Jar Size (mL)	Ball Size (mm)	Speed (RPM)	Total Milling Time	Heating Treatment	Conductivity ($S.cm^{-1}$)	Ref.
Retsch	Sigma Aldrich	ZrO_2	50	10	600	20 min	-	2×10^{-4}	This work
Fritsch	Sigma Aldrich	ZrO_2	45	4	510	20 h	270 °C, 2 h	1×10^{-4}	[122]
Fritsch	Sigma Aldrich	ZrO_2	80	3	500	48 h	270 °C, 12 h	1.5×10^{-4}	[123,124]
Fritsch	Sigma Aldrich	ZrO_2	45	4	510	15 h	220 °C, 2 h	1×10^{-4}	[125–127]
Fritsch	Nagao	ZrO_2	45	4	510	1.5 – 8 h	270 °C, 2 h	$1.7 – 4 \times 10^{-4}$	[128,129]
Retsch PM400	Aladdin Chem	ZrO_2	50	-	500	13.5 h	270 °C, 2 h	1.7×10^{-4}	[130]
Fritsch	Sigma Aldrich	ZrO_2	50	3	510	48 h	270 °C, 48 h	0.4×10^{-4}	[131]
Fritsch	Sigma Aldrich	ZrO_2	50	3	510	20 h	270 °C, 1 h	1×10^{-4}	[132]
Across International	Alfa Aesar	Agate	-	-	510	15 h	270 °C, 2 h	2×10^{-4}	[133]
Fritsch	-	ZrO_2	45	10	-	10 h	250 °C, 2h	-	[134]

5.2. Experimental Methods

5.2.1. Ball Milling of Na_3PS_4

Na_2S (Sigma Aldrich 98% or Nagao 99.6%) and P_2S_5 (Sigma Aldrich 99%) was loaded into a milling jar at a molar ratio of 75:25, respectively. The total mass of the mixture was 1 gram. The milling jar volume is 50 mL with an inner lining made of Y-ZrO_2 (Retsch). The jar was preloaded with ZrO_2 grinding media where an 8.7:1 jar to grinding-media volume ratio was maintained. The loaded jar was sealed in an Ar-containing glovebox and the milling proceeded under inert conditions using a Retsch PM100 planetary ball mill. Ball milling proceeded at 550

RPM unless stated otherwise. In the case where the effect of heat treatment was evaluated, the samples were loaded into a quartz tube and capped with a rubber septum. The tube was then flame-sealed and heat-treated in a box furnace (Lindberg Blue M). The temperature was ramped from room temperature to 270 ^{o}C at a rate of 10 ^{o}C min^{-1} and held for two hours at temperature. The sealed tube was then quenched in ice water and the sample extracted for characterization.

5.2.2. Electrochemical Impedance Spectroscopy (EIS)

The conductivity of the solid electrolyte material was evaluated by EIS. Pellets were formed with a custom-made PEEK die mold and titanium plungers. Na_3PS_4 powder was loaded into the 10 mm diameter PEEK pellet die and pressed at 360 MPa at room temperature. The two titanium plungers were used as blocking current collectors for the EIS measurements. Data was collected with a Solartron 1260 frequency response analyzer, with an excitation potential of 30 mV and a frequency range between 1MHz and 1Hz.

5.2.3. Materials Characterization

All X-ray diffraction (XRD) samples were loaded into boron-rich 0.5 mm diameter glass capillary tubes (Charles Supper) and flame-sealed to prevent exposure to ambient atmosphere. The samples were measured on a Bruker Kappa goniometer equipped with a Bruker Vantec 500 detector. XRD data was collected using Cu K_α radiation at 45 kV and 50 mA, over a 2θ range of 10 - 70°. Rietveld refinement was conducted using the GSAS software suite.[135,136] Raman (Renishaw inVia/Bruker Innova) was used with 514 nm illumination, provided by an Modu-Laser 50 mW Ar^+ ion laser. The samples were prepared by placing the powder onto a coverslip and sealed with Kapton tape. Data collection was made through the cover slip side.

5.2.4. Scanning Electron Microscopy (SEM)

Iridium was sputtered onto the electronically insulating SSE by an Emitech sputter coater for 7 seconds with a current of 85 μA. Images of particle morphology and size were taken with a FEI Quanta 250 SEM.

5.2.5. Electrochemical Characterization

DC polarization measurements were made with a Biologic SP-200 potentiostat with a low-current probe attachment. A pellet of Na_3PS_4 (ball milled for 1 hour at 550 rpm with 11 x 10 mm grinding media) was made in a PEEK die by pressing between titanium plungers at 360 MPa. The steady-state current was collected when varying polarization potentials to determine the electronic conductivity of the solid electrolyte. An all solid-state battery was constructed with TiS_2 (Sigma Aldrich 99.9%) as the cathode, Na_3PS_4 as the electrolyte, and $Na_{15}Sn_4$ alloy as the anode. TiS_2 was chosen for the cathode as it has sufficient electronic conductivity and does not require the addition of carbon. The anode alloy was formed by ball milling stoichiometric amount of Na and Sn in a 15:4 ratio under inert conditions, as outlined by Tanibata et. al. [23]. The alloy anode was chosen over sodium metal because the later is known to form a resistive interphase with Na_3PS_4.[137] $Na_{15}Sn_4$ is relatively more stable and used to evaluate the ball-milled Na_3PS_4 in an all solid-state cell. The composite cathode material consisted of 1:1 weight ratio of TiS_2 and Na_3PS_4, mixed together with agate mortar and pestle. The tri-layer all solid-state cell was constructed in a PEEK die mold and pressed to 360 MPa with titanium plungers. The titanium plungers were also used as the current collectors.

5.3. Results and Discussion

5.3.1. Ball milling time

Total ball milling time was the first synthesis parameter investigated in this work, as it presents the largest variation in the literature (Table 1). For this well-controlled exploration, rotational speed was fixed at 550 RPM and the material's conductivity was measured at intermittent ball milling time intervals. The results were collected and are presented in Figure 1. Two distinct stages of the ball milling process could be observed and assigned, namely the Formation and Saturation stages. During the Formation stage, the ionic conductivity of the SSE increases from 0.18 x 10^{-4} S cm^{-1} to a maximum of 1.7 x 10^{-4} S cm^{-1}, which was achieved within one hour of total ball milling at the given conditions. While in the Saturation stage, the ionic conductivity of the SSE does not increase with any additional milling and suggest the material synthesis has reached steady state. To understand the processes occurring during these two stages, the structural evolution of the mixture at each time interval was analyzed with XRD and Raman spectroscopy (Figure 2).

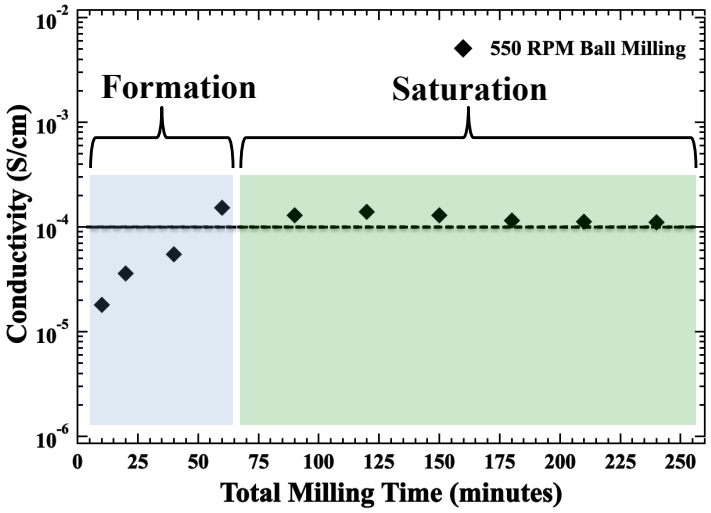

Figure 5.1. Conductivity evolution of the ball-milled 75Na2S-25P2S5 mixture as a function of total milling time at 550 RPM with 10 mm grinding media.

XRD and Raman analyses reveal that the ball milling process induces a reaction between starting precursors during the Formation stage, as shown in Figures 2a and 2b. The starting mixture of Na_2S and P_2S_5 are gradually consumed to form Na_3PS_4 and occurs as early as ten minutes into ball milling. In Figure 2a, markers indicate where cubic and tetragonal Na_3PS_4 phases can be identified and vertical dashed lines are used to distinguish the non-overlapping peaks of tetragonal Na_3PS_4. The intense peaks identified as Na_2S are also present with the SSE in the early stages of Formation. After ten minutes of ball milling, the diffraction peaks for P_2S_5 are no longer visible; it is presumed that P_2S_5 becomes amorphous and thus invisible to diffraction experiments. In this case, Raman spectroscopy was used as a complementary technique to XRD. Figure 2b depicts the Raman spectroscopy measurements collected on the ball milled sample. The Na_3PS_4 exhibits peaks at 280 cm^{-1}, 411 cm^{-1}, 536 cm^{-1}, and 567 cm^{-1} attributed to the tetrahedral PS_4^{3-}. The P_2S_5 exhibits Raman peaks at 159 cm^{-1}, 180 cm^{-1}, 191 cm^{-1}, 197 cm^{-1}, 270 cm^{-1}, 303 cm^{-1}, 385 cm^{-1}, 394 cm^{-1}, 405 cm^{-1} and was determined to be present during the first ten minutes of ball milling. This shows that P_2S_5 is indeed in the mixture and the reaction of Na_3PS_4 was determined to be incomplete during the early stages of Formation. From the XRD patterns in Figure 2a, the concentrations of Na_3PS_4 increases as starting precursors are being consumed; as shown by their decreasing relative peak intensities as ball milling progresses. Once sixty minutes of total ball milling time is reached, the XRD and Raman results show that only Na_3PS_4 is present and the starting precursors are completely consumed.

Sodium ion conductivities were also measured in parallel with XRD and Raman data collection at the respective milling intervals. During the Formation stage, the ionic conductivity increases with ball milling from 0.18 x 10^{-4} S cm^{-1}, 0.36 x 10^{-4} S cm^{-1}, 0.55 x 10^{-4} S cm^{-1}, until a maximum value of 1.7 x 10^{-4} S cm^{-1} is reached and all of the starting precursors are consumed at

the end of the Formation stage. Saturation begins at this stage, meaning any additional ball milling does not improve nor degrade the material's conductivity. Coupled with XRD and Raman, it is evident that there are no more structural changes, secondary phases, or precursor peaks detected with additional ball milling during the Saturation stage. As such, we can conclude that the Saturation stage is synonymous with reaction completion, as only the Na_3PS_4 phase is detected. The XRD and Raman results for after ninety minutes of ball milling are not shown for clarity.

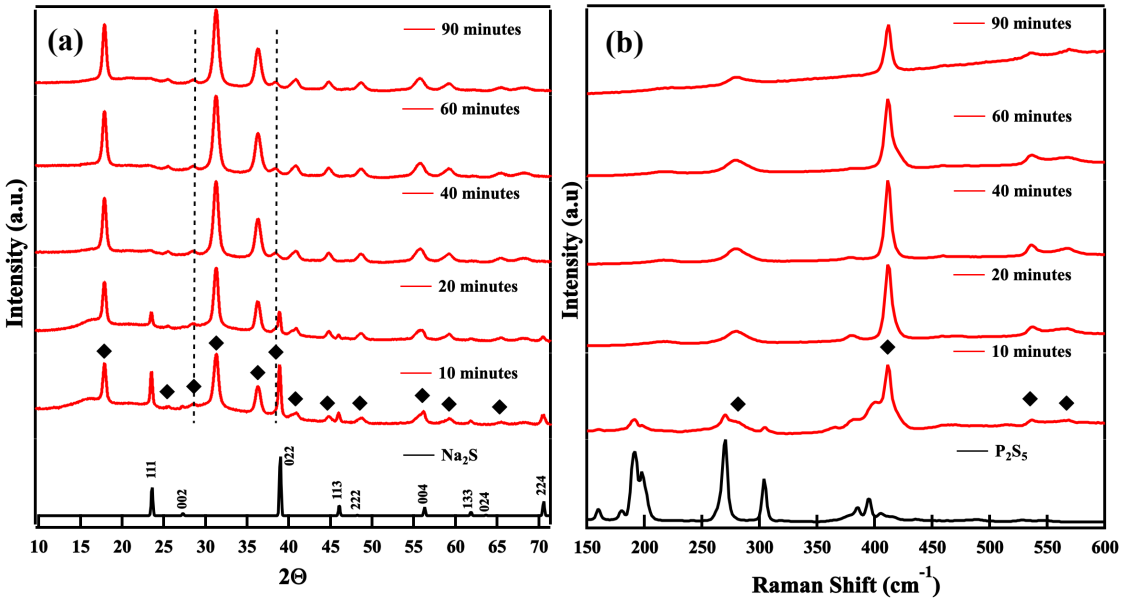

Figure 5.2. (a) XRD patterns of mixture at various milling times. (b) Raman spectra of the $75Na_2S$-$25P_2S_5$ mixture at various milling times. ◆Markers indicate overlapping peaks of cubic and tetragonal Na_3PS_4 phase and the dashed lines denote peaks from the latter phase.

Rietveld refinement was performed on the material ball milled for a total of one hour and the results are shown in Figure B1 and tabulated in Table B1 of the Supporting Information. The main phase was determined to be cubic Na_3PS_4 and the minor phase determined to be tetragonal Na_3PS_4, at 91% and 9% weight percent, respectively. The peaks of cubic and tetragonal Na_3PS_4 overlap except for the (201) ($2\theta = 24^o$) and (212) ($2\theta = 37^o$) peaks. These peaks are forbidden in

the $I\bar{4}3m$ space-group (No. 217) for the cubic phase, while they are allowed in the $P\bar{4}2_1c$ space group (No. 114) for the tetragonal phase, where the cubic symmetry is broken by the latter phase having a larger c-lattice parameter. The results determined in this work are consistent with Krauskopf *et. al.*, where they conducted a detailed structural analysis of the two phases of Na_3PS_4 being present in the SSE.[123] Interestingly, all the peaks of the Na_3PS_4 are present during the first ten minutes of milling. This suggests that the formation of both cubic and tetragonal Na_3PS_4 is simultaneous during the early stages of ball milling. Nonetheless, a higher percentage of cubic Na_3PS_4 phase was found at the latter stages and explains the high conductivities measured. The mechanism of this reaction has yet to be well understood and this presents a good direction for future work.

Our results show the crystalline phase Na_3PS_4 can be directly obtained from ball milling, which is contrary to findings by Hayashi *et al.* However, this is consistent with results reported by Berbano *et al.*, where crystalline phases were achieved via both ball milling and melt-quenching with a starting Na_2S-P_2S_5 mixture at molar ratios of 3 to 1.[122,138] Further analysis of the material was collected with differential scanning calorimetry (DSC) and is described in Figure B2 of the Supporting Information. The results are consistent with our XRD and Raman spectroscopy findings. By forming the desired structure without the need for post-synthesis heating of an amorphous phase, it is expected to reduce the time and energy cost needed to form the desired SSE.

5.3.2. Rotational speed and grinding media size

The influence of the rotational speed and the grinding media size was also investigated. It was found that the rotational speed of ball milling has a direct effect on the time required to complete the Formation stage. From Figure 3a, increased speeds is shown to reduce the time

required to complete the reaction of Na_3PS_4 and achieve maximum conductivity: going from 550 RPM to 600 RPM, the synthesis time can be reduced from one hour to as short as twenty minutes. A similar result was observed when the grinding media size was varied and the rotational speed was fixed at 550 RPM and shown in Figure 3b. The largest media size used was 10 mm diameter balls and maximum conductivity is achieved after one hour of total milling at 550 RPM. Longer milling times were needed as the size of grinding media was reduced, with the smallest grinding media (3 mm in diameter), 500 minutes of ball milling are required to complete the formation of Na_3PS_4. This can be attributed to the lower kinetic energy of the collisions resulting from the smaller grinding media; a decrease in energy means a longer milling time is required to complete the SSE reaction. It is important to note that the Formation and Saturation stages are always present regardless of which milling parameter is varied.

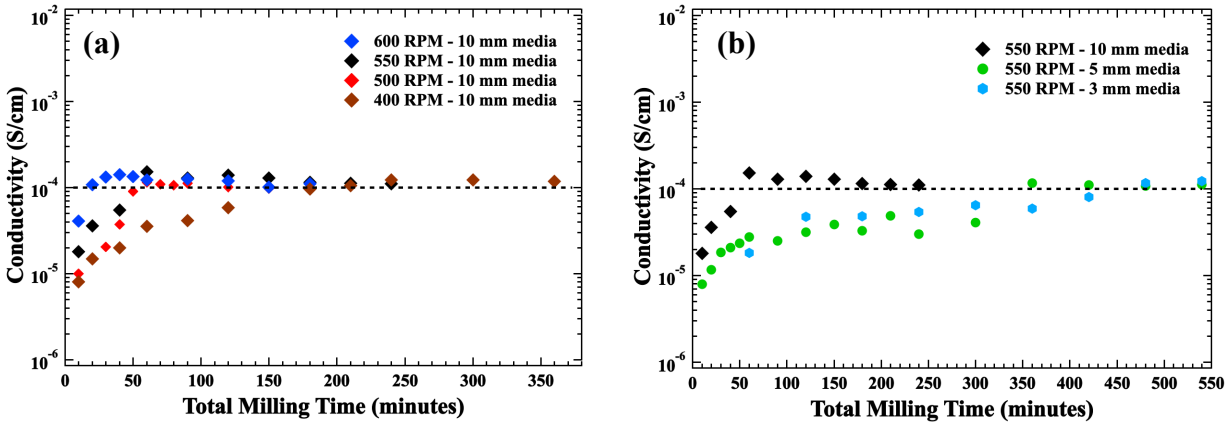

Figure 5.3. Evolution of the conductivity of the $75Na_2S$-$25P_2S_5$ mixture during the synthesis, when (a) varying the ball milling speed and (b) varying the grinding media size.

Ball milling is commonly used as a particle size reduction method to break down coarse materials into fine powders where smaller media sizes are expected to produce finer particles. At the same time it can also make particle sizes more homogenous. As such, SEM was used to examine the morphology and determine the particle size distribution of the Na_3PS_4 electrolyte

milled with varying media size at the end of each Saturation stage. Representative particles and their particle size distribution (evaluated from a sample size of 320 particles for each grinding media size) are shown in Figure B3. As shown on the SEM images, the grinding media size does not induce any modification of the morphology of the particles. On the other hand, the particle size distribution (tabulated in Table S2, described by the diameter of 10% (D10), 50% (D50) and 90% (D90) of the particles), is clearly influenced by the grinding media size. It appears that when switching from 10 to 3 mm grinding media, D10 is slightly reduced from 1.8 to 1.5 μm, D50 goes from 3.3 to 2.6 μm and D90 shrinks from 7.4 to 4.7 μm. This is also apparent on the average size of the particles, and most importantly on the standard deviation on the particle size distribution; when using 3 mm grinding media, the standard deviation is only 1.4 μm compared to 2.6 μm for the 10 mm media. The standard deviation is representative of the width of the particle size distribution and is expected for planetary ball milling, as using smaller grinding media reduces the size of the particles.

5.3.3. Heat treatment

In this work, we show that a crystalline Na_3PS_4 phase is formed during the ball milling process alone, achieving the desired material structure and conductivity without subsequent heat treatment. However, Hayashi *et al.* suggested that heat treatment of the amorphous phase (produced from the ball milling process) was necessary to form a crystalline structure.[129] This was explained to be an important process as the highly conductive cubic Na_3PS_4 could be only formed via low temperature heating, contrary to findings by Jansen *et al.* To investigate whether further heat treatment is needed once the formation stage has been completed, a structural comparison of ball-milled $75Na_2S$-$25P_2S_5$, without heat treatment and with subsequent heat treatment, was collected with XRD and shown in Figures 4a and 4b, respectively. In the case

where the starting precursors are only mixed, *i.e.* no ball milling, heating the mixture to 270°C for two hours resulted in the formation of tetragonal Na_3PS_4 with additional unidentified impurities. Na_2S is not found to be present in the XRD measurement and is believed to be completely consumed. The tetragonal polymorph is apparent in the XRD plot, as the signature peak splitting is present and caused by the c-lattice asymmetry compared with the cubic structure. In contrast, when the starting material is ball milled, as previously demonstrated, Na_3PS_4 is formed in the first ten minutes of ball milling as seen in Figure 4a. The peaks of Na_2S are identified in the sample that was ball milled for ten minutes, while the P_2S_5 peaks are believed to be amorphous and only detectable with Raman. Subsequently, the mixture having been ball milled for ten minutes, was heated at 270°C for two hours and the resulting product was found to be mostly tetragonal Na_3PS_4. The remaining milled samples were subjected to heating, and similarly, tetragonal Na_3PS_4 can be observed at up to forty minutes in Figure 4b. However, it can be seen that as ball milling progresses before the heat treatment, features of tetragonal Na_3PS_4 is reduced and more cubic Na_3PS_4 remains, when the samples are heated.

When the Saturation stage is reached after sixty minutes of ball milling, the main phase observed is cubic Na_3PS_4, as shown in Figure 4a. Figure 4b shows that subsequent heat treatment of this sixty-minute ball-milled mixture does not result in any impurities nor structural changes as opposed to mixtures that were subjected to shorter ball milling times, *i.e.* mixtures still in the Formation stage. Saturation is thus synonymous with the complete consumption of the starting precursors; none remain to form tetragonal Na_3PS_4 upon subsequent heat treatment. According to Figure 4b, if non-ball-milled Na_2S and P_2S_5 remain and are directly heated to 270°C, tetragonal Na_3PS_4 forms. However, ball milling forms majority cubic Na_3PS_4 and it is interesting to note that once the cubic phase forms, the phase transition from cubic to tetragonal appears to be

kinetically limited even at elevated temperatures. These results are also supported by the Rietveld refinement results in Figure B2 and Table B1.

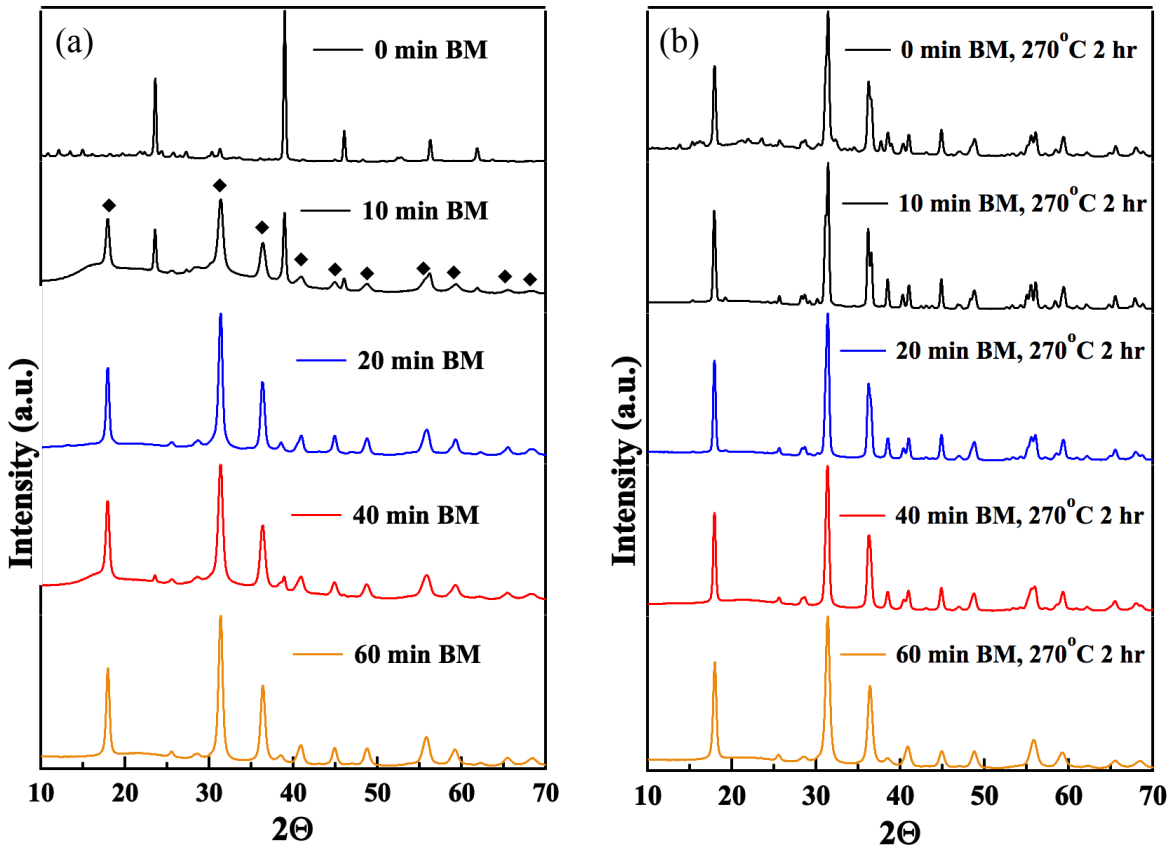

Figure 5.4. XRD patterns of $75Na_2S$-$25P_2S_5$ mixtures at various milling times (a) without and (b) with heat treatment at 270 °C for 2 hours. ◆ Markers indicate peaks belonging to the Na_3PS_4 phase.

A comparison of the material's overall ionic conductivity when subjected to ball milling, with and without heat treatment, is shown in Figure 5a and 5b. When the material is only ball milled, its overall conductivity follows the same progression discussed earlier and a maximum conductivity is achieved when the Saturation stage is reached. However, subsequent heat treatment of the ball-milled material does not have a significant effect on the material's overall conductivity at each milling and heating interval. When the mixture is ball milled for ten minutes and heated, its Na^+ conductivity does not differ from the mixture subjected to only ball milling.

Similar results were measured from the samples subjected to further synthesis, where ball milling only or ball milling with heating does not significantly alter the SSE conductivity. The measured conductivity is likely from the cubic phase, which has remained after ball milling and heating and the progressive increase in conductivity reflects the larger percentage of cubic Na_3PS_4 formed from the milling process. Therefore, the results in this work strongly suggest that synthesis of highly conductive Na_3PS_4 can be achieved through a one-step ball milling process without any subsequent processing.

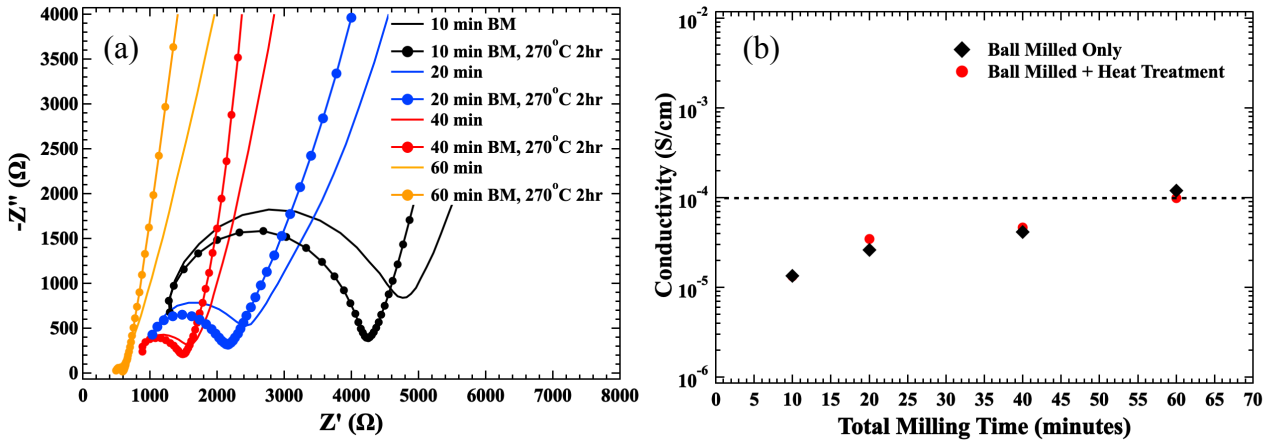

Figure 5.5. a) Nyquist plots and (b) corresponding conductivity measurements of $75Na_2S$-$25P_2S_5$ ball milled mixtures with and without heat treatment.

5.3.4. Sources of the Na_2S reactant

The final parameter that was varied is the source of Na_2S, or the purity of Na_2S. This has been argued to critically affect the properties of Na_3PS_4,[129] where high-purity Na_2S was suggested to produce high Na^+ conductivity. A comparison of the SSE conductivity synthesized from different precursor sources was tracked and shown in Figure 6. It can be seen that the synthesis trend between Na_2S sourced from Nagao (99.6%) or Sigma Aldrich (98%) are similar. The purity of the Na_2S source is found to not have a significant influence on the ionic conductivity of the synthetized Na_3PS_4.

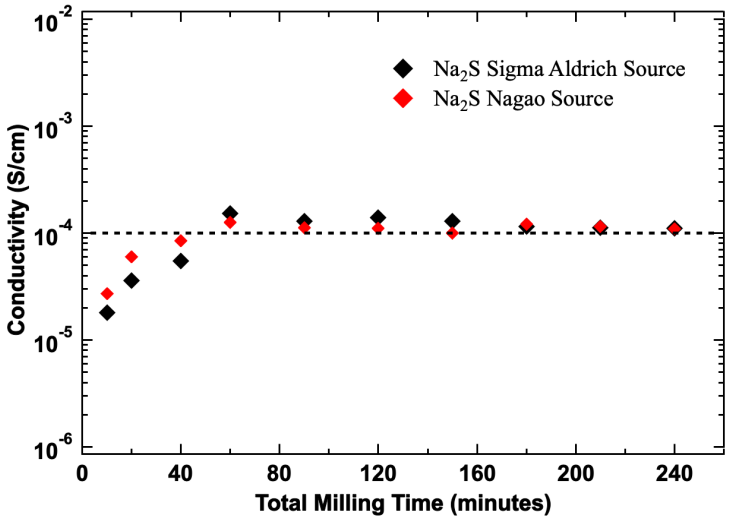

Figure 5.6. Ionic conductivity comparison of Na_3PS_4 made with Na_2S sourced from Sigma Aldrich (98%) and Nagao (99.6%)

5.3.5. Electrochemical performance evaluation

While the ionic conductivity (σ_i) of SSEs is an important property to evaluate how quickly the material can shuttle ions between electrodes, its electronic conductivity (σ_e) is an equally important but commonly overlooked characteristic. An ideal SSE should have a σ_e several orders of magnitude lower than its σ_i. Here, we measure the electronic conductivity by polarizing the synthesized SSE to a series of different potentials and holding at these potentials until a steady state current response is reached. The non-zero steady state current of the SSE with Ti blocking electrodes represents the electronic conductivity of Na_3PS_4. The linear response in the I-V relation is plotted in Figure 7a and the σ_e was determined from this slope. The σ_i was found to be six-orders of magnitude larger than the σ_e, and the comparison is shown in Figure 7b. The large difference between the two transport properties of the SSE makes it an ideal electrolyte material.

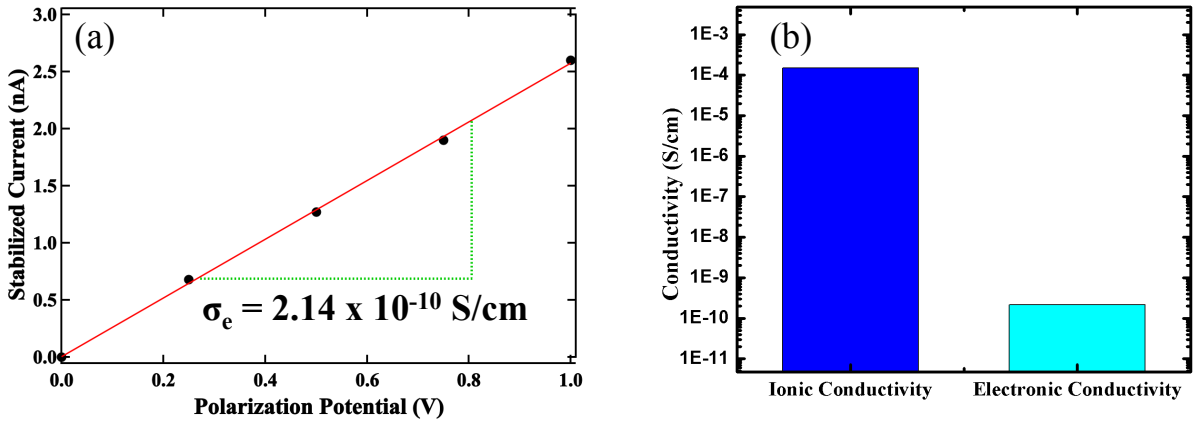

Figure 5.7. (a) Electronic conductivity of Na_3PS_4. (b) Ionic and electronic conductivity comparison of Na_3PS_4.

The performance of Na_3PS_4 was also evaluated in an all-solid-state battery using TiS_2 and a $Na_{15}Sn_4$ alloy as the cathode and anode, respectively. The first charge and discharge cycle is shown in Figure 8a where the ASSB was able to deliver 185 mAh g^{-1} on the first discharge. The ASSB rate performance was also evaluated and shown in Figure 8b. The ASSB is able to deliver a discharge capacity of 153, 138, 115, and 75 mA g^{-1} when subjected to current densities of 126, 189, 378, and 945 μA cm^{-2}, respectively. These results, in combination with the previous characterization results, show that Na_3PS_4, synthesized in this work by single-step ball milling, has proven to be functional as a SSE in an all-solid-state sodium ion battery.

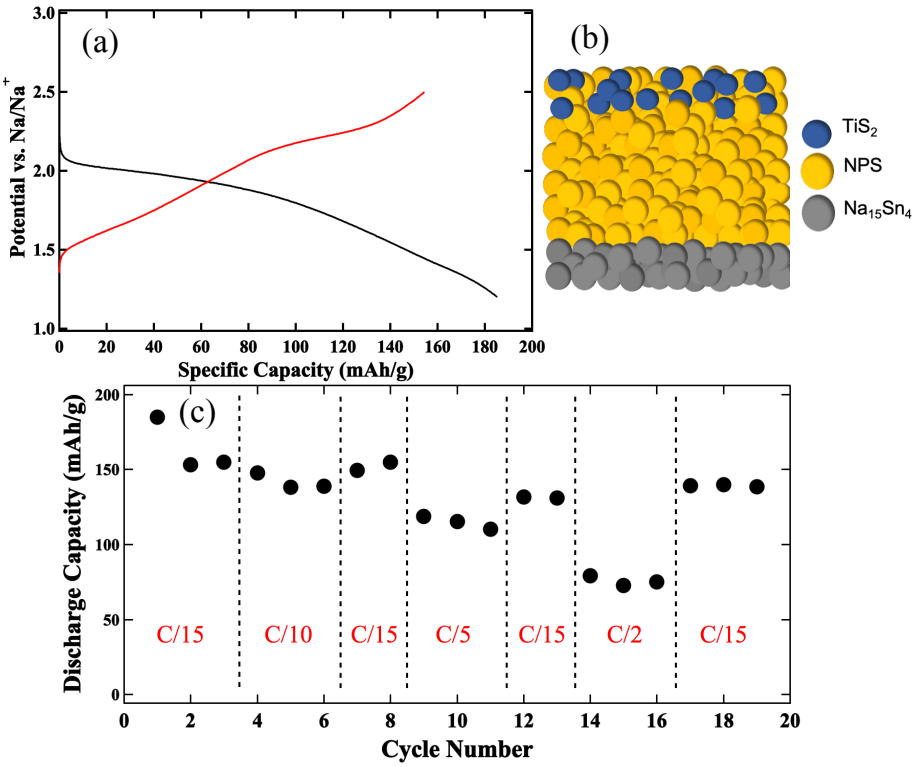

Figure 5.8. (a) Potential curve at the first cycle, (b) diagram of all-solid-state battery construction, and (c) rate performance of Na_3PS_4 in an all-solid-state battery. Current density to C-rate are: 126 µA cm^{-2} (C/15), 189 µA cm^{-2} (C/10), 378 µA cm^{-2} (C/5), 945 µA cm^{-2} (C/2).

5.4. Conclusions

Existing literature reports on Na_3PS_4 solid electrolyte synthesis shows large variations in synthesis conditions, all of which is achieved with multiple synthesis steps. Through systematic investigation of the various key synthesis parameters, we demonstrated that cubic Na_3PS_4 synthesis can be achieved in a single step. This is done by identifying the Formation and Saturation stages of Na_3PS_4 synthesis; once Saturation is reached, the reaction to form highly conductive Na_3PS_4 has completed and any additional processing has no effect on the material's conductivity or structural properties. The completion rate of the Formation stage is dependent on the rotational speed and grinding media size used during the milling process. Finally, electrochemical cycling of a $Na_{15}Sn_4$|NPS|TiS_2 cell demonstrates that Na_3PS_4 can be synthesized

in a facile one-step process and that subsequent heat treatment is not critical. A one-step, scalable ball-milling process is favorable for production of large batch sizes of solid-state electrolyte, one essential aspect for commercial viability.

Chapter 5, in full, is a reprint of the material "Single-step synthesis of highly conductive Na_3PS_4 solid electrolyte for sodium all solid-state batteries" as it appears in the Journal of Power Sources, Nguyen, H.; Banerjee, A.; Wang, X.; Tan, D.; Wu, E. A.; Doux, J.; Stephens, R.; Verbist, G.; Meng, Y.S., 2019. The dissertation author was co-primary investigator and author of this paper. The author performed all the experimental work and electrochemical tests.

Funding to support this work was provided by the Energy & Biosciences Institute through the EBI-Shell program.

We thank Dr. Curtis Moore and Dr. Milan Gembicky at the Crystallography Facility at the University of California, San Diego for assisting on the capillary XRD data collection. The characterization work was performed in part at the San Diego Nanotechnology Infrastructure (SDNI), a member of the National Nanotechnology Coordinated Infrastructure, which is supported by the National Science Foundation under Grant ECCS-1542148.

Chapter 6 Room-Temperature All-Solid-State Rechargeable Sodium-ion Batteries with a Cl-doped Na_3PS_4 Superionic Conductor

6.1. Introduction

Rechargeable all-solid-state sodium-ion batteries (ss-SIBs), which utilize ubiquitous sodium sources, are a promising low-cost, high-safety alternative to today's lithium-ion batteries, especially for large-scale energy storage applications.[67,116,117,139,140] However, a critical challenge in the development of ss-SIBs is the lack of a sodium solid electrolyte with high ionic conductivity at ambient temperatures and a wide electrochemical window. Although oxide solid electrolytes such as β-alumina and NAtrium (or sodium) Super Ionic CONductors (NASICON) are well known, they exhibit reasonable ionic conductivities only at higher temperatures.[13,109,141–144] Moreover, their synthesis requires high-temperature processing to reduce the grain-boundary resistance, which is incompatible with traditional cathode materials and thus requires special fabrication procedures.1

Chalcogenide-based (S, Se) chemistries offer the potential for higher ionic conductivities than oxides.[64,66,145–152] Though it is likely that sulfide and selenide-based solid electrolytes may exhibit lower intrinsic electrochemical stability, the formation of passivating phases at the electrode/solid electrolyte interface can potentially mitigate further reactions.[75,100,153] Sulfide electrolytes, particularly sodium sulfides, also tend to be softer than oxides,[154] which allows intimate contact between electrode and solid electrolyte to be achieved via cold pressing instead of high-temperature sintering.

In recent years, several sodium superionic conductors with ionic conductivities approaching that of traditional organic electrolytes have been identified. For example, the cubic phase of Na_3PS_4 (c-Na_3PS_4) was first reported by Hayashi and co-workers in 2012 with a

measured Na^+ conductivity of 0.2 mS cm^{-1}.[122] The crystal structure of c-Na_3PS_4 has the $I\bar{4}3m$ space group and is the high-temperature,[155] disordered polymorph of tetragonal Na_3PS_4 (t-Na_3PS_4) with space group $P\bar{4}2_1c$.[121] Since the discovery of c-Na_3PS_4, there have been a number of successful efforts at further enhancing the room temperature conductivity of Na_3PS_4 systems,[129,155,156]with the highest value thus far of 0.74 mS cm^{-1} achieved within the (1-x)c-$Na_3PS_{4-x}Na_4SiS_4$ pseudo-binary system at x around 0.06.[156] A recent first principles investigation by some of the authors of this work proposed that Na-excess-induced Na disorder is the reason for the high conductivity observed in c-Na_3PS_4, and that Sn^{4+} cation doping (for P^{5+}) may yield greater improvement in conductivity than Si^{4+} doping but at the expense of higher dopant formation energy.[84]

The introduction of defects via aliovalent doping is a common strategy to improve the ionic conductivity of materials. For Na_3PS_4, previous efforts have mainly focused on the cubic phase and the introduction of Na excess interstitials via substitution of P^{5+}. An alternative strategy of aliovalent doping is to introduce Na^+ vacancies in Na_3PS_4. Halide (X^-) anion doping (for S^{2-}) is a potential strategy for Na^+ vacancy creation.[157] However, previous experimental efforts with (1-x)c-Na_3PS_4-xNaI glass-ceramics achieved a Na^+ conductivity of ~0.1 mS cm^{-1},[128] which is lower than that of the undoped and Si-doped c-Na_3PS_4. Furthermore, an unknown phase was found as the major precipitant when NaI was introduced at $x \geq 0.1$, suggesting an intrinsic incompatibility of I^- ions with the S^{2-} host at such high doping levels.

In this work, we demonstrate the stable cycling of a TiS_2|t-$Na_{3-x}PS_{4-x}Cl_x$|Na ss-SIB at room temperature, with a capacity of about 80 mAh g^{-1} at a rate of C/10 over 10 cycles for the first time. The key enabler to this outstanding cell performance is a novel Cl-doped t-Na_3PS_4 solid electrolyte with formula $Na_{2.9375}PS_{3.9375}Cl_{0.0625}$, which was developed using a tightly

integrated combination of density functional theory (DFT) calculations, synthesis and characterization. From DFT calculations, we show that Cl^- exhibits good chemical compatibility with the S^{2-} host, with low dopant formation energy and similar ionic radius. The concomitant introduction of Na vacancies results in a predicted room-temperature Na^+ conductivity exceeding 1 mS cm^{-1}. These predictions are confirmed through experimental synthesis of tetragonal $Na_{2.9375}PS_{3.9375}Cl_{0.0625}$, and its demonstration in a ss-SIB architecture. We will also present evidence from DFT computations that suggest that the superior performance achieved in this cell is not only the result of the high Na^+ conductivity of the solid electrolyte, but also the formation of electronically-insulating, ionically-conducting passivation layers at the electrode-solid electrolyte interface due to the presence of the Cl^- anion.

6.2. Methods

6.2.1 Density functional theory calculations

All DFT calculations were performed using similar methodologies as previous works by the authors.[52,158]For the sake of brevity, we refer interested readers to those works and only briefly summarize the key parameters here.

All calculations were performed with the Vienna Ab initio Simulation Package (VASP),[52] within the projector augmented wave (PAW) approach.[46] The Python Materials Genomics (pymatgen) materials analysis library was used for all analyses.[50] All structural relaxations and total energy calculations were carried out using parameters similar to those used in the Materials Project.[48] The key parameters are the use of the Perdew-Burke-Ernzerhof (PBE) generalized-gradient approximation (GGA)[47] exchange correlation functional, an energy cutoff of 520 eV and a k-point mesh of at least 1000/atom. For the doped structures, an enumeration of all symmetrically distinct halide-vacancy orderings in a 2 × 2 × 2 supercell of Na_3PS_4 was carried

out,[159] and the lowest energy configuration was used for all subsequent calculations and analyses, including ab initio molecular dynamics (AIMD) simulations. For phase diagram construction,[82] the precalculated energies of all phases in the Na-P-S-X systems (X = F, Cl, Br, and I) other than those of primary interest in this work were obtained from the Materials Project database via the Materials Application Programming Interface.[49]

6.2.2 Dopability analysis.

To assess the likelihood of halide doping into Na_3PS_4, we estimated the neutral dopant formation energy using the formalism originally presented by Wei and co-workers,[84,160] $E_f[X] = E_{tot}[X] - E_{tot}[bulk] - \sum_i n_i\mu_i$, where $E_{tot}[X]$ and $E_{tot}[bulk]$ are the total energies of the structure with and without the neutral dopant X, respectively. μ_i is the atomic chemical potential of specie i that varies based on different experimental conditions; n_i indicates the number of atoms of specie i being added ($n_i > 0$) or removed ($n_i < 0$) from the pristine structure. In this work, the lower bound of the dopant formation energy was calculated, which is equal to the difference of decomposition energies between the doped and host materials.[84]

6.2.3 Electrochemical analyses

The electrochemical stability of the solid electrolytes in contact with the electrodes was estimated using the grand potential approach proposed by Ong et al.[82] which assumes that Na is the main mobile species. Under such conditions, the solid electrolyte-electrode interface is modeled as an open system with respect to Na. The relevant thermodynamic potential is then the grand potential, given as $\varphi \approx E - \mu_{Na}N_{Na}$, where E is approximated as the DFT total energy. It should be noted that the chemical potential of Na is related to the voltage vs. Na/Na^+ (V) via the following relation, with $V = -(\mu_{Na} - \mu^o_{Na})$ where μ^o_{Na} is reference potential of Na metal.

6.2.4 Ionic conductivity calculations

The diffusivity and conductivity of the Cl-doped t-Na_3PS_4 structure were calculated using AIMD simulations. Non-spin-polarized AIMD simulations were conducted in the NVT ensemble at 800 – 1400 K with a Nose-Hoover thermostat.[161,162] A smaller plane-wave energy cutoff of 280 eV and a minimal Γ-centered 1 × 1 × 1 k-point mesh were adopted. The time step of the simulations was 2 fs. The initial structure was fully relaxed at 0 K, and the volume was fixed for AIMD at elevated temperatures until the diffusivity was converged. No framework melting was observed in all simulations. All calculations were automated using automated in-house AIMD workflow software.[31,163] The Na^+ diffusivity (D) and conductivity (σ) can be extracted from the AIMD simulations using the following expressions: $D = \frac{1}{2dt}\langle[\Delta\vec{r}(t)]^2\rangle$, where d is the dimensionality of diffusion (= 3 for t-Na_3PS_4 structure); $\langle[\Delta\vec{r}(t)]^2\rangle$ is the average mean square displacement (MSD) over a time duration t. The diffusivity was obtained by performing a linear fitting of the MSD vs. 2dt. Arrhenius plots were constructed to determine the activation energies and obtain extrapolated room temperature diffusivities D_{300K}. The room temperature Na ion conductivity σ_{300K} can then be derived from the Nernst-Einstein equation, $\sigma_{300K} = \frac{\rho z^2 F^2}{RT} D_{300K}$, where ρ is the molar density of diffusing Na ions in the unit cell; z = 1 is the charge of Na ions; and F and R are the Faraday's constant and the gas constant respectively. T = 300 K was used in the above equation.

6.2.5 Synthesis

Pure t-Na_3PS_4 was synthesized from reagent-grade Na_2S (Alfa Aesar, 99%) and P_2S_5 (Sigma Aldrich, 99%). The precursors were ground in agate mortar and pestle in a molar ratio of 75:25, respectively. To introduce the chloride dopant, NaCl (Alfa Aesar, 99.99%) was mixed into the previous precursors following the chemical reaction $(1.5 - x)Na_2S + 0.5P_2S_5 + xNaCl \rightarrow$

$Na_{3-x}PS_{4-x}Cl_x$. The resulting mixtures were then sealed under vacuum in a quartz tube, heated to 1073 K (800 °C) for 4 hours, and then quenched in ice water. Subsequently, the sample was ground in a mortar and pestle and sealed in an ampoule to be heat treated at 693 K (420 °C) for 2 hours to stabilize the tetragonal phase. The samples were ground back into a powder with mortar and pestle, and re-pelletized. These pellets were then processed via spark plasma sintering (SPS). To prepare the sample, a 10 mm tungsten-carbide circular die was lined with graphite foil and the powder was placed in between two tungsten-carbide plungers, also coated with graphite. The entire setup was placed in the SPS chamber, and the sample was pressed to 100 MPa (100 MPa min^{-1}), heated to 573 K (100 K min^{-1}), and then allowed to dwell under these processing conditions for 5 minutes to reach a densified state. All synthesis steps were performed in a dry, inert (Ar) environment, unless otherwise stated.

6.2.6 Characterization of solid electrolytes

The structural characterization was performed via X-ray diffraction (XRD). The data was collected by a Rigaku diffractometer over a 2Θ range of 30 – 60°, with a step size of 0.02° and a dwell time of 2 seconds. The beam was generated by a Cu-K_α source (40 kV, 100 mA). The sample was sealed under Kapton tape to prevent degradation or side-reactions during measurements.

Cross-sectional images of the SPS pellets were obtained using a Phillips XL30 scanning electron microscope (SEM). Pristine and doped pellets were suspended in an acrylic matrix that was polished for imaging. Iridium was sputtered onto the surface of the sample using an Emitech sputter chamber operating at 85 mA for 7 seconds. The sample was imaged using a 10 kV beam. Additionally, an elemental mapping analysis was conducted using an energy dispersive X-ray spectroscopy (EDX) aperture in the SEM. SEM and EDX were conducted under high vacuum.

6.2.7. Electrochemical characterization.

The electrochemical performance was evaluated via electrochemical impedance spectroscopy (EIS). The data was collected using a Solartron 1260 impedance analyzer operating from 1 MHz to 1 Hz with a DC bias of 0 V and an applied AC voltage of 25 mV. Carbon was used as blocking electrodes. The pellet was held between two titanium plungers serving as current collectors. The temperature dependence of conductivity was obtained by placing the cell in an electric furnace. The cell was ramped to 453 K (180 °C) from room temperature in 25 K increments. Prior to each measurement, the cell was held at the temperature for one hour to allow the system to reach thermal equilibrium. The sodium ion-migration activation energy was calculated from the slope of the Arrhenius plot. All measurements were taken in a dry, inert (Ar) atmosphere.

A full cell was assembled using a TiS_2 composite cathode against a Na metal anode. TiS_2 was mixed with t-$Na_{3-x}PS_{4-x}Cl_x$, x = 6.25% in a 1:2 weight ratio. The doped (x = 6.25%) solid electrolyte (200 mg) was cold-pressed at 360 MPa in a 13 mm polyetheretherketone (PEEK) die. The cathode blende (10 mg) was cold-pressed at 360 MPa on top of the electrolyte layer. Pure Na metal was attached to a titanium current collector and cold-pressed into the die at approximately 30 MPa. The cell was cycled using Arbin battery cycler at room temperature. Cycling was performed at a C/10 rate for 10 cycles over a voltage window from 1.2 V to 2.4 V. The cell was cycled inside an Ar glovebox.

6.3 Results

Using DFT calculations, we first performed a systematic investigation of the dopability of potential halide X^- (X = F, Cl, Br, and I) into both the tetragonal and cubic phases of Na_3PS_4. As the DFT predictions for both phases are extremely similar, we will henceforth present only the

results of the more stable tetragonal phase for brevity, and interested readers are referred to the Supplemental Information for the results on the cubic phase.

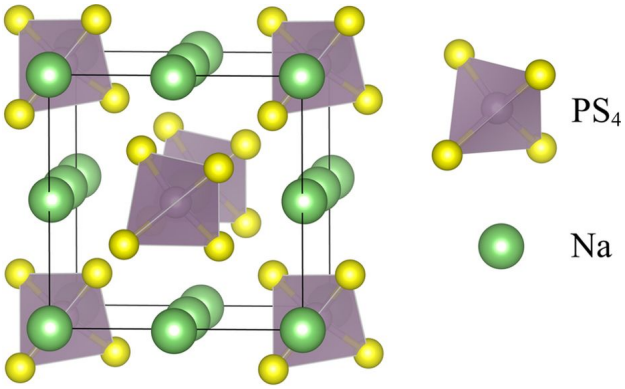

Figure 6.1. Crystal structure of pristine t-Na_3PS_4. The tetragonal polymorph of the Na_3PS_4 crystal. There are symmetrically distinct Na sites in t-Na_3PS_4, Na2 (4d) and Na2 (2a), and the PS_4 tetrahedral are centered at the 2b positions

6.3.1. Dopability of Na_3PS_4.

Figure 1 shows the crystal structure of t-Na_3PS_4. There are two symmetrically distinct Na sites in t-Na_3PS_4, Na1 (4d) and Na2 (2a), and the PS_4 tetrahedra are centered at the 2b positions.[121] The symmetrically distinct Na sites in c-Na_3PS_4 are labeled similarly as cubic Na1 (6b) and Na2 (12d). The Na1 (4d) and Na2 (2a) sites in t-Na_3PS_4 essentially occupy the same positions as the Na1 (6b) sites in c-Na_3PS_4.[157]

Table 6.1. Dopant formation energies E_f and ratio of halide to sulfide ionic radii (R_x/R_s) of the t-$Na_{3-x}PS_{4-x}X_x$ (X = F, Cl, Br, and I) at x = 6.25%

Dopant	R_x/R_s	x (%)	E_f (eV/dopant)
F	0.7	6.25	0.76
Cl	0.98	6.25	0.96
Br	1.07	6.25	1.11
I	1.21	6.25	0.99

A single halide dopant was introduced into a 2 × 2 × 2 supercell of t-Na_3PS_4 by replacing one of the S atoms with X, and simultaneously a Na vacancy was introduced to form

$Na_{47}P_{16}S_{63}X$, or t-$Na_{3-x}PS_{4-x}X_x$ with x = 0.0625. All symmetrically distinct $V'_{Na} - X^{\boxtimes}_S$ configurations (Kröger–Vink notation is adopted) were evaluated, and the lowest energy configuration was used for subsequent analyses.

Table 1 summarizes the halide dopant formation energies. We find that all halides (F, Cl, Br, and I) are predicted to have relatively low formation energies at a doping level of x = 0.0625. Fluoride doping is predicted to be the most favorable (E_f = 0.76 eV/F^-), followed by chloride (E_f = 0.96 eV/Cl^-) and iodide (Ef = 0.99 eV/I^-). Bromide doping is by far the least favorable with E_f = 1.11 eV/Br^-. Higher doping levels result in a significantly higher dopant formation energy, e.g., E_f= 1.77 eV when doping Cl^- in the same supercell size at x = 0.125. For all doped structures, the lowest energy structure has the X^- anion substituted in the S^{2-} (8e) site with a vacancy on the Na2 site. Nevertheless, the energy differences between different $V'_{Na} - X^{\boxtimes}_S$ orderings are generally small (<10 meV/atom), which suggest that the dopants and vacancies are likely to be disordered at room temperature.

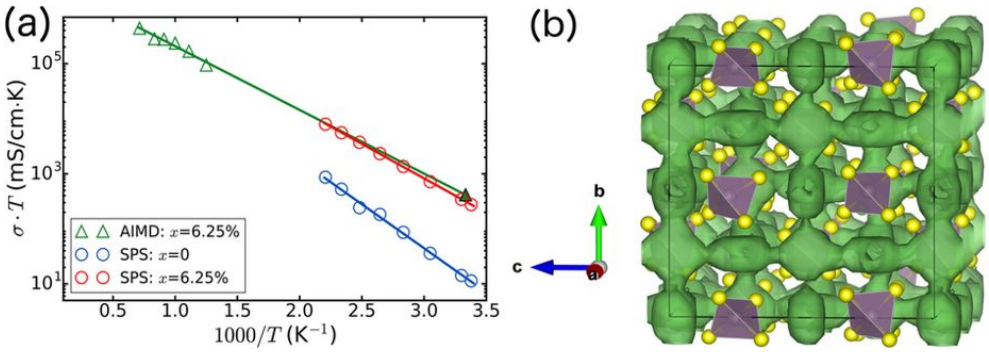

Figure 6.2. Arrhenius plots of the t-$Na_{3-x}PS_{4-x}Cl_x$ with x = 0 (blue) and 6.25% (red) obtained from SPS measurements, and x = 6.25% (green) from AIMD simulations. The filled green triangle indicates the extrapolated ionic conductivity at 300 K from AIMD simulations. (b) Isosurface of the Na^+ probability density distribution (P, in green) in the t-$Na_{3-x}PS_{4-x}Cl_x$ (x = 6.25%) at 800 K, with P = 0.0001 a_0^{-3} (a_0 is the Bohr radius).

Despite the fact that F^- doping is predicted to be the most favorable, we have selected Cl^- doping for further investigation due to several considerations. First, NaCl, also known as table salt, is by far a more commonly available precursor than NaF. Second, fluoride chemistry

inherently comes the possibility of HF exposure. Finally, the Cl^- anion has an ionic radius that is closest to S^{2-}, which would minimize the local structural distortion introduced at the substituted site. The doping concentration of Cl is fixed at x = 0.0625, given that previous work in doping I^- (which has a similar dopant formation energy at the same concentration) into c-Na_3PS_4 at x > 0.1 resulted in formation of unknown phases.[128]

6.3.2. Ionic conductivity of Cl-doped t-Na_3PS_4.

As demonstrated in recent work by some of the co-authors,[84] pristine c-Na_3PS_4, i.e., without interstitial or vacancy defects, is predicted to be an extremely poor ionic conductor in AIMD simulations. Using AIMD simulations (see Methods section), a similar result is obtained with t-Na_3PS_4 in this work, which is not surprising given that the small differences in lattice parameters and atomic positions between the cubic and tetragonal polymorphs. Figure 2a shows the Arrhenius plot of the log of the conductivity-temperature product ($\sigma \cdot T$) versus 1/T for t-$Na_{2.9375}PS_{3.9375}Cl_{0.0625}$ obtained from AIMD simulations. With the introduction of a $V'_{Na} - Cl^{\boxdot}_S$ defect pair, the Na^+ conductivity at 300 K is predicted to be 1.38 mS $cm^{-1}$with an activation barrier of 232 meV (see Table 2). During the preparation of this article, it has come to our attention that Klerk et al. has also performed AIMD simulations on halide doping in t- and c-Na_3PS_4.[157] Though the qualitative conclusions of vacancy-induced conductivity are similar, we note that Klerk et al. only performed relatively short AIMD simulations at a single temperature of 525 K; room-temperature Na^+ conductivities and activation energies were therefore not obtained.

From the Na^+ probability density distribution (Fig. 2b), we may observe that t-$Na_{2.9375}PS_{3.9375}Cl_{0.0625}$ is predicted to be a 3D diffuser comprising of chains of Na1 sites along the c direction interconnected via the Na2 sites, which form a body-centered cubic sub lattice. Such

a 3D diffusion network is expected to be highly robust against the potential introduction of blocking defects.[164]

6.3.3. Electrochemical stability of t-$Na_{3-x}PS_{4-x}Cl_x$

Besides high ionic conductivity, an effective solid electrolyte candidate should also exhibit good electrochemical stability against the electrodes. Electrochemical stability may be achieved in two ways. First, the solid electrolyte can be intrinsically inert against any reaction with the electrodes. However, due to the high reactivity of Na metal and the highly oxidizing nature of the most charged high-voltage cathodes, it is difficult to find a material that is intrinsically stable over such a wide range of sodium chemical potential.[75,151]A second, more achievable option is to optimize the electrode-solid electrolyte chemistry as a whole such that good passivation layers are formed at the electrode-solid electrolyte interfaces that act as a barrier against further reaction. A good passivation layer should have a reasonable Na^+ conductivity, and low electronic conductivity.

Table 6.2. Calculated AIMD and experimental Na^+ conductivity and activation energy of the t-$Na_{3-x}PS_{4-x}Cl_x$ superionic conductor. Values in the square brackets indicate the error range of the calculated ionic conductivity.

x (%)	AIMD simulations		Experiment	
	σ_{300K} (mS cm^{-1})	E_a (meV)	σ_{300K} (mS cm^{-1})	E_a (meV)
0	N/A	N/A	0.05	317
6.25	1.38 [1.04, 1.82]	232	1.14	249

Figure 3 shows the Na grand potential phase stability plot of the t-$Na_{2.9375}PS_{3.9375}Cl_{0.0625}$ solid electrolyte as a function of Na chemical potential. We find that at the Na-metal anode ($\mu_{Na} - \mu^0_{Na}$ = 0 eV), the predicted phase as equilibrium comprises Na_2S, NaCl and Na_3P in the ratio of 63:1:16. The dominant phase Na_2S is a good electronic insulator with PBE band gap of 2.4 eV, and NaCl has a PBE band gap of 5.0 eV.[48] Na_3P has a small PBE band gap of 0.4 eV (the screened hybrid HSE functional[89,165] gives a band gap of 0.76 eV), but is not expected to dominate the conductivity characteristics of the anode/electrolyte interface. The predicted phase equilibrium is very similar to those of pristine t-Na_3PS_4 that consists of Na_2S and Na_3P in the ratio of 4:1. It should be noted that the PBE functional tends to severely underestimate band gaps, and the true band gaps are likely to be even higher. These phases are expected to exhibit moderate Na^+ conductivity, particularly in an amorphous solid-electrolyte interphase (SEI) layer.

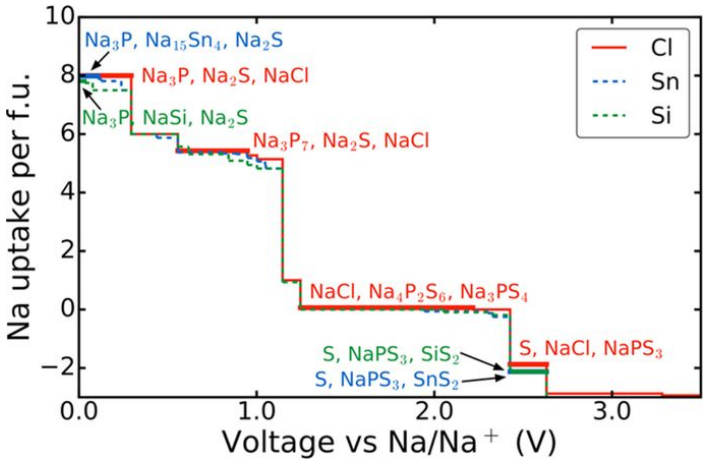

Figure 6.3. Plots of Na uptake per formula unit of t-$Na_{2.9375}PS_{3.9375}Cl_{0.0625}$ (red solid), c-$Na_{3.0625}Sn_{0.0625}P_{0.9375}S4$ (blue dashed) and c-$Na_{3.0625}Si_{0.0625}P_{0.9375}S_4$ (green dashed) solid electrolytes against voltage vs Na/Na$^+$. At low voltage (high Na chemical potential), each solid electrolyte undergoes reduction and uptakes Na, while at high voltage (low Na chemical potential), each solid electrolyte is oxidized and loses Na. Text indicates the predicted phase equilibrium at corresponding regions of the profile. Only selected regions are annotated for brevity

At voltages above 2.4 V versus Na/Na+, we find that the t-$Na_{2.9375}PS_{3.9375}Cl_{0.0625}$ solid electrolyte is predicted to be unstable against Na extraction to form $NaPS_3$+ S + NaCl. However,

if the operating voltage is kept below 2.4 V, the predicted phase equilibrium at the charged cathode-solid electrolyte interface retains t-Na_3PS_4 + NaCl as the primary component.

6.3.4 Synthesis and characterization of t-$Na_{3-x}PS_{4-x}Cl_x$

Pure t-Na_3PS_4 was synthesized from Na_2S and P_2S_5 precursors. The Cl^- dopant was introduced by adding NaCl following the chemical reaction:

$$(1.5 - x)\ Na_2S + 0.5P_2S_5 + xNaCl \rightarrow Na_{3-x}PS_{4-x}Cl_x.$$

The resulting pellets were then densified via spark plasma sintering (SPS) to minimize porosity of the solid electrolyte. The synthesis details are given in the Methods section, and the dimensions and density of the pristine and doped pellets are provided in Appendix C (see Table C1).

Figure 4a shows the XRD data for the two compositions, t-$Na_{3-x}PS_{4-x}Cl_x$ with x = 0% and 6.25%. At x = 0%, we identify the crystalline phase formed to be t-Na_3PS_4, and the XRD pattern is in excellent agreement with the previous study by Jansen et. al.[121] With the addition of chloride via NaCl at x = 6.25%, the tetragonal phase is retained with trace amounts of unreacted NaCl, and no reflections from unknown crystals are present in the spectra. Additionally, we observe a slight increase in the peak intensities of all the XRD reflections, with the most significant change occurring in the high index peaks, (112) and (211), at about 31°. This observation is the first indication that aliovalent substitution of S^{2-} by Cl^- was successful, because the halogen has a higher scattering factor than sulfur.

Rietveld refinement calculations were first conducted for t-$Na_{3-x}PS_{4-x}Cl_x$. To obtain a baseline of the crystal parameters, a refinement calculation was performed on the pristine (x = 0%) structure. The refined XRD pattern of the pristine structure is shown in Fig. 4b. The refined lattice constants for the pristine structure are in excellent agreement with the previously reported

values.[121] These parameters were then used as an initial model to study the aliovalent substitution of S^{2-} by Cl^{-}. Figure 4c shows the refined pattern of doped t-$Na_{2.9375}PS_{3.9375}Cl_{0.0625}$. No unknown phase was detected in the crystal, and no side reactions were observed during the synthesis. Although a trace amount of NaCl was detected in the spectrum, our refinement results show that it comprises less than 1 at%.

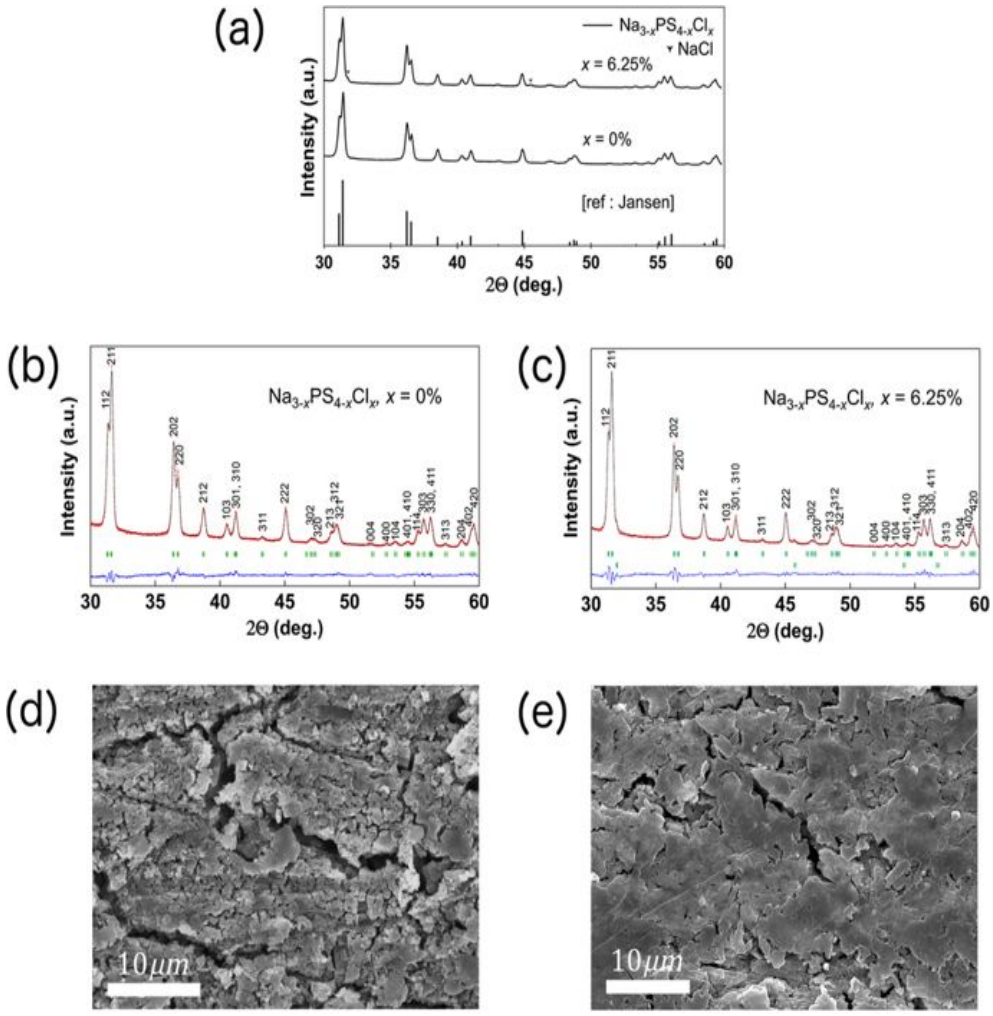

Figure 6.4. (a) XRD patterns for t-$Na_{3-x}PS_{4-x}Cl_x$ with x = 0% and 6.25%, and previous study in ref. 27. (b) Refinement plot of the pristine t-Na3PS4. (c) Refinement plot of Cl^{-}doped t-Na_3PS_4. Solid red and black lines denote the observed and calculated XRD patterns, while the green ticks mark the position of the reflections allowed by the space groups of t-Na_3PS_4 ($P\bar{4}2_1c$) and NaCl ($Fm\bar{3}m$). The difference between the observed and calculated patterns is signified by the blue line. (d) SEM image of pristine t-Na_3PS_4 SPS sample, and (e) SEM image of SPS sample of doped t-$Na_{3-x}PS_{4-x}Cl_x$ (x = 6.25%). Scale bar is 10 μm.

Table 3 summarizes the crystallographic parameters (lattice constants, thermal factors, and atomic occupancies) of the pristine and doped solid electrolyte from the Rietveld refinement and DFT calculations, which are in excellent agreement. From the refinement calculations, we estimated an increase in the lattice volume associated with the substitution of S^{2-} by Cl^{-}. This volumetric change is very small and also agrees well with the DFT values. With the introduction of Cl^{-}, there is a corresponding decrease in sodium and sulfur occupancies and increase in their respective isotropic thermal factors (B_{iso}). These observations can be attributed to the formation of the Na^{+} vacancy. In summary, the Rietveld refinement supports the successful incorporation of Cl^{-} into the S^{2-} sublattice, with the concomitant introduction of Na^{+} vacancies. More advanced characterization techniques such as solid-state nuclear magnetic resonance (NMR) may be employed to confirm the success of the doping in future work. Cross-sectional SEM images of the pristine t-Na_3PS_4 and doped t-$Na_{2.9375}PS_{3.9375}Cl_{0.0625}$ SPS samples under identical processing conditions are shown in Fig. 4d,e, respectively. We note that the Cl^{-} doping does not lead to any significant morphology changes. The images show that the local morphology of the pellets is densely formed due to SPS processing in both compounds. An EDX measurement was collected from the doped sample (see Figure C1 in Appendix). From the EDX measurement, we determined that sulfur and chlorine are uniformly distributed throughout the sample, with no noticeable aggregation of element-rich domains. In conjunction with the refinement results, the majority of the chloride dopant is found to be integrated into the host crystal lattice.

Table 6.3. Rietveld refinement results of t-$Na_{3-x}PS_{4-x}Cl_x$ systems, where a, b and c are lattice constants, and V, Occ., and B_{iso} are normalized cell volume, site occupation numbers, and isotropic atomic displacement parameters, respectively. Residual factors, R_b and R_{wp}, for the pristine (x = 0%) composition are 3.86% and 4.97%, respectively; and for the doped (x = 6.25%) are 4.29% and 5.31%. For the pristine t-Na_3PS_4, the DFT calculated cell parameters are a = b = 6.99 Å, c = 7.12 Å, V = 348 Å3, in excellent agreement with the refinement results as well as those by Jansen et al. (ref. 27): a = b = 6.952 Å, c = 7.076 Å, V = 341.97 Å3.

Pristine (x = 0%), Space Group $P\bar{4}2_1c$					
a=b= 6.956(5) Å, c=7.088(6) Å, V = 342.9 (5) $Å^3$					
R_b = 3.86%, R_{wp} = 4.97%					
	x	y	z	Occ.	Biso ($Å^{-2}$)
Na1 (4d)	0	0.5	0.426 (4)	2	2.54 (9)
Na2 (2a)	0	0	0	1	3.2 (1)
P (2b)	0	0	0,5	1	0.5 (6)
S (8e)	0.315 (3)	0.345 (2)	0.167 (2)	4	1.1 (6)
Doped (x= 6.25%), Space Group $P\bar{4}2_1c$					
a=b= 6.970(5) Å, c=7.092(6) Å, V = 344.5 (5) $Å^3$					
R_b = 34.29%, R_{wp} = 5.31%					
	x	y	z	Occ.	B_{iso} ($Å^{-2}$)
Na1 (4d)	0	0.5	0.428 (4)	1.99	3.0 (9)
Na2 (2a)	0	0	0	0.99	3.4 (1)
P (2b)	0	0	0,5	1	0.1 (6)
S (8e)	0.316 (4)	0.344 (3)	0.165 (2)	3.94	1.19 (9)
Cl (8e)	0.316 (4)	0.344 (3)	0.165 (2)	0.02	1.19 (9)

6.3.5 Conductivity measurements of t-$Na_{3-x}PS_{4-x}Cl_x$

The experimental measurement of pristine t-Na_3PS_4 shows a low ionic conductivity of 0.05 mS cm^{-1} at 303 K, with an activation energy value of 317 meV (see Fig. 2a and Table 2). The t-$Na_{2.9375}PS_{3.9375}Cl_{0.0625}$ solid electrolyte, on the other hand, shows an extremely high conductivity of 1.14 mS cm^{-1} at 303 K and a low activation barrier of 249 meV.

The measured conductivity and activation barrier are in excellent agreement with the calculated values (see Table 2). The room temperature Nyquist plots for the pristine t-Na_3PS_4 and doped t-$Na_{2.9375}PS_{3.9375}Cl_{0.0625}$ are given in Figure S2, where the total impedance in each structure was used to calculate the room temperature conductivities of each material. A significantly larger semi-circle is observed for the pristine t-Na_3PS_4 compared to doped t-$Na_{2.9375}PS_{3.9375}Cl_{0.0625}$, indicating a much larger total resistance in the pristine t-Na_3PS_4.

6.3.6 Electrochemical performance

A full cell was constructed using a TiS_2 charged cathode and a Na-metallic anode. The choice of the TiS_2 cathode is motivated by its suitable operating voltage (~1.7 V versus Na/Na^+), which is well within the limits of the DFT predicted stability window of the t-$Na_{2.9375}PS_{3.9375}Cl_{0.0625}$ solid electrolyte, as well as its fast kinetics for Na^+ intercalation.[115] The cell was galvanostatically cycled from 1.2 V to 2.4 V. The cell was held for two minutes between switching from charging to discharging. A current density of 0.149 mA cm^{-2} was applied, corresponding to a C/10 rate. The theoretical capacity of the $NaTiS_2$ active material is 198 mAh g^{-1}. The discharge and charge capacity of the first cycle were ~240 mAh g^{-1} and 80 mAh g^{-1}, respectively. The source of the excess capacity as well as the large irreversible capacity of the first cycle is currently under investigation, and will be the evaluated in a subsequent study of the interface stability and its effects on cyclability and longevity. Currently, impedance

measurements during the first cycle clearly indicate the formation of stable interfacial phases at the solid-electrolyte/electrode interfaces (see Figure C3 in Appendix C). The subsequent charge and discharge capacities of the cell over 10 cycles were ~80 mAh g^{-1}, with a coulombic efficiency above 98% (see Fig. 5). Such a stable performance is consistent with the cyclic voltammetry results (see Figure C3 in Appendix C) in which Cl-doped t-Na_3PS_4 is found electrochemically stable against the Na anode for up to 5 V. Strong polarization, common in Na-ion cells, was also observed at the point of switching from charging to discharging, and vice versa.

6.4 Discussion

The design of an all-solid-state rechargeable battery is a multi-component, multi-property optimization effort; it is therefore insufficient to merely focus on bulk ionic conductivity of the solid electrolyte as the only target parameter. In this work, we have demonstrated how an integrated computational and experimental effort can significantly accelerate such multi-component, multi-property optimization, resulting in a promising new t-$Na_{2.93\ 75}PS_{3.9375}Cl_{0.0625}$ solid electrolyte that has been demonstrated in a full ss-SIB cell with good cyclability and capacity. Aliovalent doping is a common strategy to introduce defects (vacancies or interstitials) into a solid electrolyte candidate to further enhances its conductivity. Surprisingly, we find halide doping in Na_3PS_4 to be somewhat more favorable than cation (Si^{4+}, Ge^{4+} and Sn^{4+}) doping, with slightly lower dopant formation energies of 0.76 – 1.11 eV vs. 1.04 – 1.32 eV for cation.[84] Though dopant formation energies of 0.76 – 1.11 eV might appear at first glance to be relatively high, it should be noted that these values depend strongly on the chemical potential references used. At the elevated temperatures during synthesis, Na_2S loss is likely to lower the chemical potentials of Na and S, significantly promoting $V'_{Na} - X_S^{\boxtimes}$ formation.

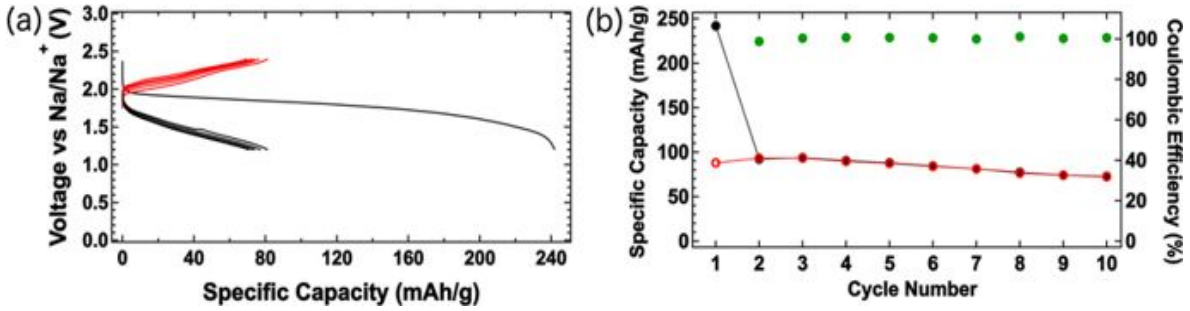

Figure 6.5. Charge- discharge profile of TiS_2|t-$Na_{2.9375}PS_{3.9375}Cl_{0.0625}$/Na full cell at room-temperature. Cell was cycled under constant current conditions with a current density of 0.149 mA cm^{-2} (C/10 rate) from 1.2 V to 2.4 V. The cell was able to routinely deliver 80 mAh g^{-1} over 10 cycles. Red and black lines in the charge-discharge profile denote charging and discharging, respectively. Similarly, red and black markers signify charge and discharge capacities, while the green circles mark the coulombic efficiency by cycle.

Both the cation + interstitials and anion + vacancies doping strategies are predicted to be effective in enhancing the ionic conductivity of Na_3PS_4. In fact, we find no evidence of any significant difference in the predicted bulk Na^+ conductivities between the cubic and tetragonal Na_3PS_4, which is not surprising given the very small differences in lattice parameters between the two polymorphs.[166] We speculate that the nature of the defects present would promote the formation of one polymorph over another. Excess Na interstitials would need to occupy the cubic Na2 (12d) sites, promoting the formation of the disordered cubic phase, while Na vacancies with halide substitution would result in slight lattice expansion (due to reduced electrostatic attraction) and promote the formation of the tetragonal phase. Indeed, our attempts at synthesizing a phase-pure Cl-doped c-Na_3PS_4 phase have been unsuccessful, while the Cl-doped t-Na_3PS_4 was readily obtained.

The fundamental difference between cation M^{4+} and anion X^- doping is in the interfacial products that are predicted to form at the Na anode. For Si or Sn-doped Na_3PS_4, small-gap compounds such as Na_4Si_4 (space group of C2/c; PBE band gap of ~1.2 eV) and $Na_{15}Sn_4$ (space group of $I\bar{4}3d$; PBE band gap of ~0 eV) as well as Na_2S and Na_3P are predicted to form at the

anode/solid electrolyte interface (see Fig. 3). For Cl-doped Na_3PS_4, on the other hand, the anode/solid electrolyte interface comprises predominantly Na_2S with smaller amounts of NaCl and Na_3P. Alkali halides are well-known components in the solid-electrolyte interphase (SEI) of rechargeable lithium-ion batteries, where LiF is formed from the reaction between the $LiPF_6$ salt and the electrodes. Indeed, the "salting" of the SEI is likely to improve its ionic conductivity as Cl^- dopants will similarly be introduced to the amorphous Na_3P + Na_2S SEI. It should be noted that in all cases (undoped, cation-doped, and halide-doped), the small-gap compound Na_3P (PBE band gap of ~0.4 eV) is also predicted to form at the Na anode, though it is not the dominant phase. Based on the achieved cycling performance in this work as well as in previous works on c-Na_3PS_4,[122] we would surmise that the effect of Na_3P on the interfacial stability is small.

Ultimately, the total conductivity of a solid electrolyte depends not only on its bulk conductivity, but also the grain boundary contributions. In this respect, the specifics of the synthesis procedure are critically important. In this work, spark-plasma sintering was used to achieve a fully dense solid electrolyte with reduced grain boundary resistance, and an overall conductivity exceeding 1 mS cm^{-1} that is very close to the DFT predicted bulk conductivity (see Fig. 2). This overall conductivity is higher than that of Si-doped c-Na_3PS_4 (0.74 mS cm^{-1})[156] and is the highest value for sodium thiophosphates achieved thus far. Although the recently reported Na_3PSe_4 and Na_3SbS_4 have higher conductivities, the more expensive and less stable Se^{2-} anion is utilized in Na_3PSe_4,[148] while Na_3SbS_4 requires a more complicated electrolyte bilayer approach using c-Na_3PS_4 to stabilize the interface at the Na anode.[152]

We have demonstrated the potential of the t-$Na_{2.9375}PS_{3.9375}Cl_{0.0625}$ solid electrolyte by integrating it in a ss-SIB full cell. In a full cell, the choice of the cathode and anode must be given careful consideration, as well as their interactions with the solid electrolyte. From the DFT

grand potential analysis, we find that the t-$Na_{2.9375}PS_{3.9375}Cl_{0.0625}$ electrolyte is predicted to be relatively stable up to ~2.4 V vs Na/Na^+, while passivation is predicted to occur at the Na anode. Therefore, TiS_2 was chosen as the cathode. At a current density of 0.149 mA cm^{-2}, a cell capacity of ~80 mAh g^{-1} was achieved over 10 cycles of the TiS_2|t-$Na_{2.9375}PS_{3.9375}Cl_{0.0625}$|Na full cell. The increase in internal cell resistance, leading to capacity decay after subsequent cycling, is common when forming a SEI layer. Though the reversible capacity reported by Hayashi et al. for the c-Na_3PS_4 solid electrolyte is similar,[122] that performance was achieved with a much lower current density (0.013 mA cm^{-2}) against a Na-Sn alloy as the anode. Though the Si-doped c-Na_3PS_4 and Na_3PSe_4 solid electrolytes have higher measured conductivities than c-Na_3PS_4, their room-temperature performance in a full ss-SIB cell has not yet been demonstrated.[148,156]To our knowledge, this is the first time that cycling at a rate as high as C/10 has been demonstrated in a full ss-SIB with a Na metal anode at room temperature.

6.5 Conclusion

In conclusion, we have demonstrated the prediction and synthesis of a novel Cl-doped tetragonal Na_3PS_4 solid electrolyte, or t-$Na_{2.9375}PS_{3.9375}Cl_{0.0625}$, and its good cycling performance in a full all-solid-state rechargeable sodium-ion cell at a rate of C/10. The predicted bulk and measured total conductivities of the t-$Na_{2.9375}PS_{3.9375}Cl_{0.0625}$ solid electrolyte exceed 1 mS cm^{-1}, which is one of the highest conductivity reported for any sodium superionic conductor thus far. More importantly, the "salting" of Na_3PS_4 is predicted to improve the characteristics of the interfacial phase equilibria at the anode/solid electrolyte interface, forming an electronically insulating and ionically conducting solid-electrolyte interphase. We also demonstrate the potential of spark-plasma sintering as a technique for achieving a dense sulfide electrolyte with reduced grain boundary resistance.

Chapter 6, in full, is a reprint of the material "Room-Temperature All-solid-state Rechargeable Sodium Ion Batteries with a Cl-doped Na_3PS_4 Superionic Conductor" as it appears in Scientific Reports, I.-H. Chu, C. S. Kompella, H. Nguyen, Z. Zhu, S. Hy, Z. Deng, Y. S. Meng, and S. P. Ong, 6, 33733, 2016. The dissertation author was the co-primary investigator and author of this paper. The author performed all the experimental work and electrochemical tests

Chapter 7 Nanoscale Solid-Solid Interfacial Engineering to Enable High Energy All-Solid-State Batteries

7.1. Introduction

All-solid-state batteries (ASSBs) have attracted enormous attention over recent years because they have many advantages over their liquid counterparts including, but not limited to, enhanced safety, absence of electrolyte leakage, and improved energy density by enabling the use of metallic anodes.[1] Solid-state electrolytes with high lithium ion conductivity have been developing rapidly over the last few years, and include both oxide and sulfide electrolytes.[2] Sulfide-based superionic conductors are considered more practical as they have higher ionic conductivities, facile synthesis procedures, can be fabricated at room temperature, and have favorable mechanical properties that allow intimate contact with cathode and anode materials.[3,4] Recently, sulfide superionic conductors have achieved an ionic conductivity close to or higher than conventional liquid electrolytes (~9 mS/cm), for instance, $Li_7P_3S_{11}$ (17 mS cm^{-1}), $Li_{10}GeP_2S_{11}$ (12 mS cm^{-1}) and $Li_{9.54}Si_{1.74}P_{1.44}S_{11.7}Cl_{0.3}$ (25 mS cm^{-1}).[5-7] However, the electrochemical performance of these sulfide superionic conductors, especially the power capability of the ASSBs, is still not comparable with the conventional liquid electrolytes as severe interfacial problems arise in the ASSBs.[8] This originates from the electrochemical reaction of the solid electrolyte, and a chemical reaction between the electrode material and sulfide solid electrolyte.[9,10] The SSEs have a narrow electrochemical stability window; they begin to decompose at a relatively lower voltage to form a resistive solid electrolyte interphase (SEI). For instance, $Li_{10}GeP_2S_{12}$ (LGPS) and $Li3_PS_4$ (LPS) are oxidized at 2.15 and 2.41 V versus Li/Li^+, respectively.[11] The decomposition becomes more severe when the SSEs are coupled with the high-voltage oxide cathodes such as $LiCoO_2$ (LCO). As a result, a very thick

SEI forms and the ASSB experiences high polarization.[10] However, the dynamic electrochemical decomposition of the electrolyte and its resultant passivation effect is still unknown. Understanding the decomposition processes and their progression with continued cycling is essential towards practical ASSBs; constructing a stable interface is crucial for sulfide-based SSEs.

To explore the chemical reaction between SSEs and high-voltage oxide cathodes, both computational and experimental methods were applied. First-principles simulations have emerged as an important complementary tool for demonstrating the mechanism of reaction occurring at the interface. For example, density functional theory (DFT) calculation results show that the interionic diffusion between Co and P at the $LiCoO_2/Li_2S$-P_2S_5 interface is energetically favorable, suggesting the thermodynamic instability between LCO and Li_2S-P_2S_5.[12,13] Ceder et al. further demonstrated the inherently incompatibility between a number of known SSEs and the high-voltage oxide cathodes.[14] Although DFT calculations provides a pool of the potential decomposition products effectively, experimentally determining the presence and distribution of these decomposition products is still a challenging and rarely-addressed problem. Electrochemical techniques, such as cyclic voltammetry and impedance measurements, cannot provide chemical information at the interface. Previous experimental evidence by the transmission electron microscopy (TEM) showed the interionic diffusion between Co and P at the $LiCoO_2/Li_2S$-P_2S_5 interface up to 50 nm in thickness after cell charge.[10] However, none of previous experimental results provided the exact chemical species at the interface, rather than elemental distribution which are summarized in Table 7.1. Identification of chemical species at the interface is very important, as its chemical and physical property directly governs the charge transfer resistance at the interface. It is also important to note that the above TEM

characterization was performed on the interface after charge, which mixed the reaction products from both electrochemical decomposition of SSE and a chemical reaction between the SSE and cathode. Both of these processes occur simultaneously, and therefore it is difficult to deconvolute their individual contributions. Isolating these phenomena is important to design and adopt the proper approach to mitigate the interface problem.

In this work, we succeeded to construct a stable interface between the electrolyte Li_6PS_5Cl (LPSCl) and the cathode $LiNi_{0.85}Co_{0.1}Al_{0.05}O_2$ (NCA) by investigating the chemical reaction and the electrochemical decomposition of LPSCl separately (Figure 7.1). The reaction products were probed by various characterization techniques such as X-ray diffraction (XRD), X-ray absorption spectroscopy (XAS) and cryogenic electron microscopy (cryo-EM) along with surface-sensitive X-ray photoelectron spectroscopy (XPS) and Raman. In addition, first-principles simulations of the model system were conducted to probe the phase equilibrium at the interfaces as well as the dynamics, which provides an atomic-scale visualization of interfacial reactions. These results show that NCA is thermodynamically unstable with LPSCl, especially at charged state. We are able to identify the chemical products at the interface whereas $LiNbO_3$ (LNO) coating NCA prevents the chemical reactions between LPSCl and NCA; the redox activity of Li_6PS_5Cl happens only at the first charge and forms a passivation layer. This self-limiting interfacial reaction along with LNO coating helps to construct a stable interphase and enables to achieve a long-life high-energy all solid-state battery.

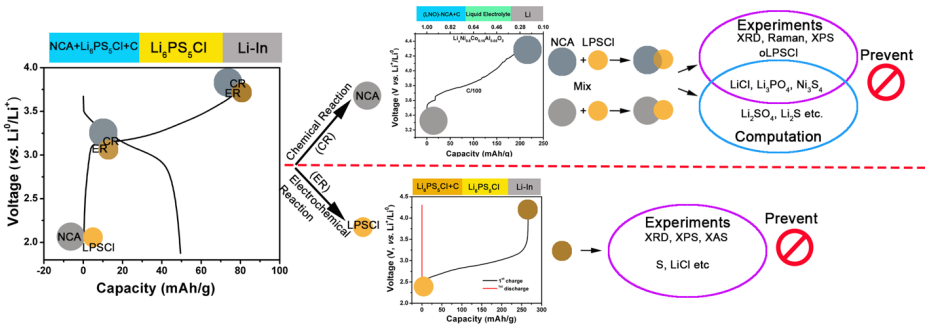

Figure 7.1. Schematic picture of the interfacial study in this work. The chemical reaction between NCA and LPSCl, and the electrochemical decomposition of LPSCl were segregated and their reaction products were explored by both experimental characterization and computation.

Table 7.1. Summarized efforts on exploring the interface between cathode and sulfides solid electrolyte by different methods. The oLPSCl refers to the oxygen oxidized LPSCl.

Cathode	Solid Electrolytes	Initial Interfacial products	Interfacial products at the charge state	Methods	Reference
LiCoO2	80Li2S-20P2S5	N/A	Co, P and S diffusion across the interface, but no chemical	FIB/TEM	10
LiCoO2	80Li2S-20P2S5	N/A	CoS/Unknown	XAS	15
LiNbO3@ LiCoO2	70Li2S-30P2S5	N/A	New interface between LNO and LCO/ Unknown	TEM	16
LiCoO2	Li3.15Ge0.15P0.85S4	N/A	Co, P and S composed interface/Unknown	TEM	10
LiCoO2	Li3PS4	Li depletion layer/ Space charge layer		DFT	17
LiCoO2	Li3PS4	Co(PO3)2 + CoS2 + S		DFT	14
LiMnO2	Li3PS4	Mn2S3 + Mn2P2O7 + S		DFT	14
LiNiO2	Li3PS4	Li4P2O7 + Ni3S4 + Li2SO4		DFT	14
LiNi0.85Co0.1Al0.05O2 (NCA)	Li6PS5Cl	P-O bond formation, NiS2,	Li3PO4, Ni3S4, LiCl, oLPSCl	Raman, XRD, XPS, DFT, AIMD	This Work
	$Li_6PS_5Cl/LiNbO_3$	No reaction		XPS/DFT	

7.2. Electrochemical performance of all-solid-state batteries:

Pure LPSCl was synthesized by ball milling and its synthesis details can be found in the Supporting Information (SI). All of the peaks present in the XRD pattern (Figure D1a) belong to LPSCl without any additional peaks. Its ionic conductivity was measured to be 1.03 mS cm^{-1} at RT (Figure D1b), consistent with the previous reference.[18] The ASSBs were fabricated with NCA-LPSCl-carbon composite (11:16:1 in weight) as the cathode, LPSCl as the electrolyte, and Li0.5In (0.62 V vs. Li/Li+) alloy as the anode. Figure 7.2a shows the potential curves of the ASSBs. The bare NCA delivers a capacity as low as 52 mAh/g, corresponding to less than 1/3 utilization of the active material (NCA). The low capacity of bare NCA is likely caused by the parasitic reactions at the electrode/electrolyte interface, which significantly increases the interfacial resistance as indicated by the Impedance measurements (Figure 7.2b). To mitigate the interfacial resistance, 2 wt% LiNbO3 (LNO) was coated on the surface of the NCA, which is denoted as LNO-NCA. The presence of the LNO on the surface of NCA is evidenced by scanning transmission electron microscopy (STEM) (Figure 7.2c) and XPS (Figure 7.2d). The STEM mapping (Figure 7.2c) clearly shows a conformal amorphous LNO coating layer on the NCA cathode and its average thickness is about 5 nm. Strong signal from Nb is found in the XPS spectra and the peak position of $3d_{5/2}$ at 207.55 eV is indicative of its +5 oxidation state. As a result, LNO-NCA achieves a much higher capacity of 161 mAh g^{-1} (Figure 1a), which is close to that in the liquid cell (Figure D2). It is worth mentioning that LNO-NCA exhibits much superior rate performance than bare NCA (Figure D3). Impedance measurements (Figure 7.2b) demonstrate that the LNO coating helps reduce the cathode charge transfer resistance by an order of magnitude, as evidenced by the dramatic reduction of the low frequency semicircle.

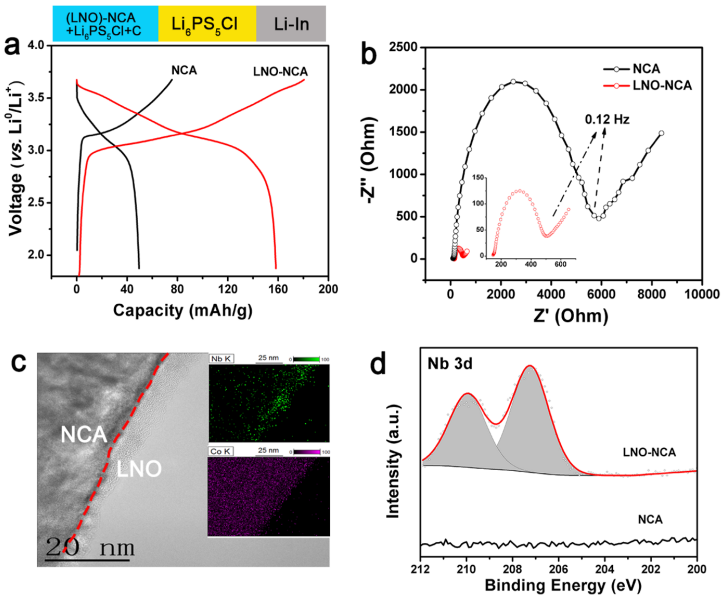

Figure 7.2. Comparison between bare and LNO coated NCA. (a) Potential curve and (b) EIS spectra of the bare and LNO-NCA. (c) STEM image and (d) XPS spectrum of Nb 3d of LNO-NCA. The inset images in (c) corresponds to the distribution of elemental Nb (green) and Co (violet), measured via energy-dispersive X-ray spectroscopy (EDX).

Although the similar positive effect of the coating layers on the high-voltage oxide cathodes was reported before, their role on reducing the charge transfer resistance is quite controversy and unclear.[9,19,20] This is mostly due to the very limited understanding of the reaction by-products at the interface, which haven't been properly identified by the experimental characterization tools as well as the computational calculation (Table 7.1). Here we proposed an effective strategy to separate the chemical and electrochemical reactions, probe their products by both bulk and surface-sensitive characterization tools, and further validate it with computational prediction at the cathode/electrolytes interfaces.

7.3. Chemical reaction between LPSCl and NCA:

To separate the contribution of the chemical reaction to the cathode interfacial resistance, the chemical reaction between NCA and LPSCl was isolated by mixing the LPSCl with the bare NCA and LNO-NCA separately (Figure 7.3a), in both the pristine and charged state (the charged

NCA was harvested from a cell containing a liquid electrolyte (Figures 7.3a)). To probe the reaction products between LPSCl and NCA, XRD, Raman and XPS were performed.

When the bare pristine NCA cathode was in contact with LPSCl, new diffraction peaks were observed in the XRD (labeled with star marks in Figure 7.3b) besides the peaks belonging to NCA and LPSCl, albeit the intensity is low. The presence of these new diffraction peaks is indicative of new phases that formed after mixing the bare NCA with LPSCl. In contrast, no new peaks were found in the XRD pattern of the LNO-NCA/LPSCl mixture, indicating that the LNO coating is able to suppress the chemical reactions that occur between bare NCA and LPSCl. Considering that the chemical reactions occurring at the interface, XPS was conducted to verify the interfacial reactions. The results show that the Ni $2p_{3/2}$ peak in the bare NCA shifts from 857.3 eV to 853.7 eV (shown in Figure D4a) after mixing it with LPSCl, suggesting the reduction of Ni and the formation of nickel sulfide (Ni_3S_4 or NiS_2).[21] In contrast, both S and P are partially oxidized since new peaks appear at a higher binding energies in their XPS spectra (Figure D4). According to the binding energy, the new peak in the S 2p spectrum is assigned to nickel sulfide (Ni_3S_4 or NiS_2) and phosphorus polysulfide (P_2S_x) while those in the P 2p spectrum are from the P_2S_x and P-O bond.[22,23] Therefore, both the Ni and S spectra reveal that nickel sulfide is one of the interfacial products formed by the chemical reaction between NCA and LPSCl. These observations are in good agreement with the computational phase equilibrium at the NCA/LPSCl interface, which will be discussed later.

The chemical reaction becomes more severe when the LPSCl was mixed with the charged NCA (to 4.3 V vs. Li/Li^+). This is expected as the charged NCA is more reactive than the pristine bare NCA due to the higher oxidation state of the transition metals. The aforementioned new peaks in the XRD pattern of the bare NCA/LPSCl mixture are also present

in the charged NCA/LPSCl mixture but are much more intense (Figure 3b). Some of these new peaks can be assigned to LiCl, Ni_3S_4 and Li_3PO_4 (Figure 7.3c) along with the formation of other unknown phases. In order to highlight these reaction products, the unreacted LPSCl was removed by washing the NCA/LPSCl mixture with ethanol; in ethanol, LPSCl is soluble, LiCl and Li_3PO_4 is sparingly soluble, and Ni_3S_4 is insoluble. After washing, the XRD peaks of the LPSCl disappear while those new peaks are retained; LiCl, Ni_3S_4 and Li_3PO_4 were clearly identified (Figure 7.3c). Thus, these three phases are confirmed as the major interfacial products at the charged NCA/LPSCl interface. The additional XRD peaks along with these three major components at the interface will be discussed later.

All of these interfacial compounds are expected to form when charging the ASSBs as the LPSCl gradually reacts with the charging NCA. These compounds will act as a resistive interfacial layer, which leads to high polarization, low capacity and poor rate capability. To mitigate this aggressive chemical reaction, LNO coating is used to protect the interface of NCA. None of the previously mentioned byproducts are found in the XRD pattern of the charged LNO-NCA/LPSCl mixture (Figure 7.3b and 7.3c). The uniform LNO coating layer serves as a barrier for the parasitic reactions between the cathode and electrolyte at both the pristine and charged states, enabling a stable interface.

Raman spectroscopy was performed to examine the short-range structural changes that may occur at the cathode/electrolyte interface. As shown in Figure 7.3d, the LPSCl has the t_{1g}

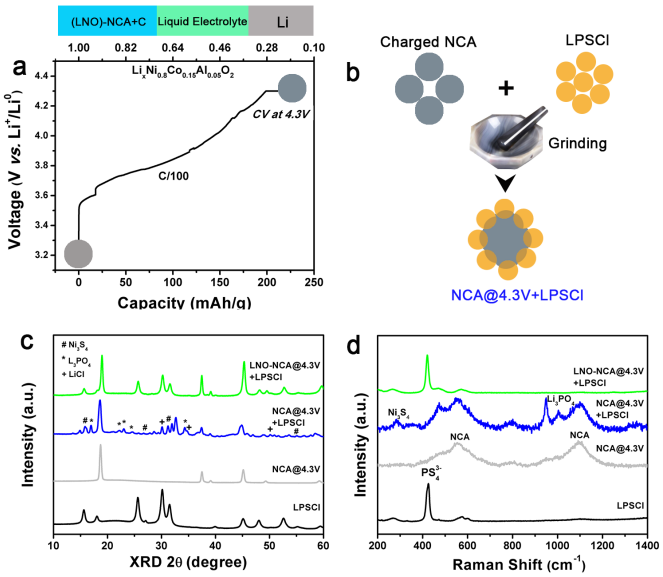

Figure 7.3. . Chemical reaction between the LPSCl and the (LNO-) NCA cathode. The schematic procedure images (a), XRD patterns (b) of the (LNO-)NCA, LPSCl and their mixtures at different reaction states, phase identification of reaction products after charge (c). Raman spectra of (LNO-)NCA, LPSCl and their mixtures at different reaction states along with Li_3PO_4 reference (d).

symmetric stretching mode (PS_4^{-3}) centered at 425 cm^{-1} and the NCA shows several vibrational modes at around 470, 550 and 1100 cm^{-1} which relate to the vibrations between the transition metals and oxygen.[24] When the LPSCl was mixed with the pristine and charged NCA, no visible new peaks appeared. This may due to the low concentration of interfacial products that are buried by the unreacted NCA and LPSCl. After removal of the LPSCl by washing, the vibrational peaks of NCA are enhanced while the signal from LPSCl disappears. More importantly, two vibrational peaks show up at 284 and 940 cm^{-1}, which belong to Ni_3S_4 and Li_3PO_4, respectively.[25,26] This is consistent with the XRD results. However, no evidence of the Ni_3S_4 and Li_3PO_4 was found in the charged LNO-NCA/LPSCl mixture; this is another direct confirmation of the effectiveness of the LNO coating to prevent side reactions between NCA and LPSCl.

7.4. DFT Insights

In order to understand the reaction mechanism between NCA and LPSCl, DFT calculations were carried out to evaluate the thermodynamically stable phases formed at the interface. The computational phase diagram is able to sort out the potential interfacial products through different reaction pathways (the reaction equations labeled in Figure 7.4a and 7.4b are tabulated in Table D1 and D3). As shown in Figure 7.4a, the negative formation energy of these reactions suggests the thermodynamic instability between NCA and LPSCl regardless the reaction pathways. LiCl, Li_3PO_4 and nickel sulfide (Ni_3S_4 or NiS_2) are formed based on the Reaction 1-3 labeled in Table D1, which presence is evidenced by the above experimental characterizations (XRD, XPS, Raman and TEM). Besides, some other reaction products are predicted to be there, such as Li_2S and Li_2SO_4 but they haven't been identified by experiments probably due to their low concentration or kinetically not favorable to form. In contrast, the driving force of interfacial reactions between NCA and LPSCl has been greatly reduced from more than 10 eV/f.u. (reaction 3 in Figure 7.3a) to around 1 eV/f.u. with LNO coating (see all labeled reactions in Table D2). Thus, we may conclude that LNO coating effectively blocks the contact between LPSCl electrolyte and NCA cathode and greatly stabilizes the interface.

The electrochemical stability windows of the interfacial products were checked and summarized in Figure 7.4b, in which the blue bar indicates the electrochemically stable window of the LPSCl and the orange bar indicates the working window of the NCA.[27] The mismatch of the above two windows suggests the intrinsic incompatibility between LPSCl and NCA. As a result, some byproducts such as LiCl, Li_3PO_4, Ni_3S_4 and P_2S_5 are present at the interface. According to their electrochemical stability window, these interfacial products are electrochemically stable during the charge and discharge processes of the NCA, which will passivate the interface and increase the interfacial resistance.

The dynamic changes at the interface at the half-discharged state (50% Li extracted) were simulated through ab initio molecular dynamics (AIMD) and the variation of structure was tracked using radial distribution function g(r) (RDF) (Figure D5). Within the first 2 ps, the characteristic P-O bond (1.5 Å) in the $[PO_4]^{3-}$ tetrahedral, M-S (M = Co, Ni) and Li-Cl bond suggest the formation of Li_3PO_4, M_xS_y (M = Co, Ni), and LiCl (Figure D5). These observations are consistent with the aforementioned interfacial products. In addition, elemental S is formed along with the Ni and Co sulfide species (Figure 7.4c and D5), which will be further discussed later. Figure 7.4c and 7.4d compare the interface model at the beginning and the end of the AIMD simulation. The results clearly show that the interionic diffusion among Ni, Co, P, S and O happens at the NCA/LPSCl interface and P-O, Ni-S, Co-S and S-S bonds form consequently.

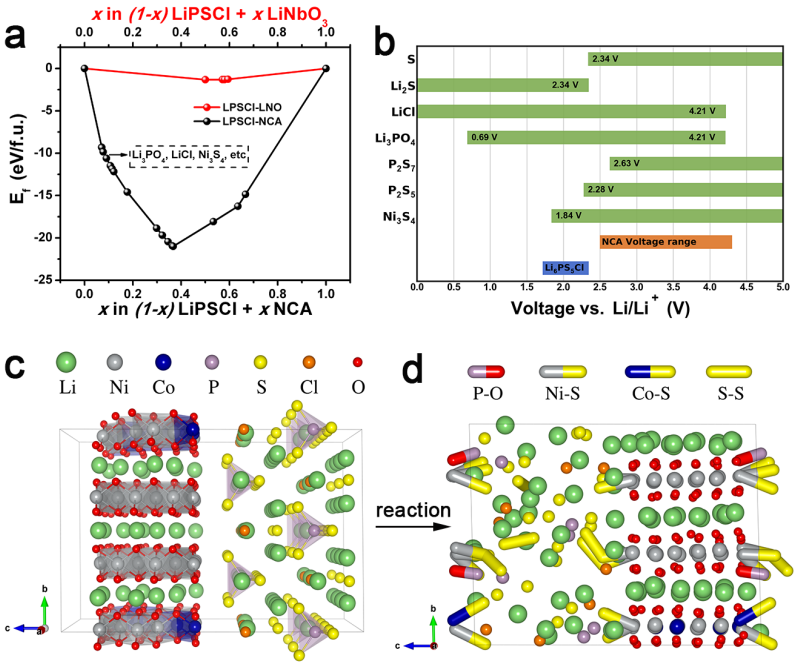

Figure 7.4. (a) pseudo-binary phase diagram between Li_6PS_5Cl electrolyte and NCA cathode and $LiNbO_3$ at different states. Labeled reactions are tabulated in Supporting Information Table D2-4. (b) electrochemical stability window of interfacial products; the atomic structure of the pristine (c) and half-discharged (d) NCA/LPSCl interface at 0 ps and 50 ps

7.5. New interfacial product oLPSCl

Although DFT calculation is a powerful tool to narrow down the potential reaction products from the well-known material databases, some unknown materials may still exist at the interface. This is true in the case of NCA/LPSCl. Aside from the appearance of new Raman peaks belonging to Ni_3S_4 and Li_3PO_4, there is a slight blue shift of the LPSCl Raman peak (PS_4^{-3}) when it is mixed with the pristine and charged bare NCA (Figure 7.5a). A similar blue shift was observed in PS_4^{-3} in the structure of the $Li_{10}GeP_2S_{12}$, where it was partially substituted by oxygen.[28] Therefore, we hypothesized that this Raman blue shift is a consequence of the PS_4^{-3} polyhedra of LPSCl reacting with oxygen contained in NCA (Figure 7.5b). To verify the oxygen reactivity with LPSCl, pure LPSCl was oxidized via purging it with dry oxygen, and the resultant sample is denoted as oLPSCl (Figure D6). Figure 7.5a compares the Raman spectra of LPSCl at different states. The peak shift of both the pristine and the charged bare NCA/LPSCl mixture matched very well with that of oLPSCl.

Further examination of the oLPSCl XRD shows that majority of its peaks match up with the charged bare NCA/LPSCl mixture, along with the products Ni_3S_4, LiCl and Li_3PO_4 (Figure 7.5b). Therefore, both Raman and XRD suggest that the oxygen in the NCA indeed participates in the chemical reaction with LPSCl to form oLPSCl; further work is required to recognize the reaction mechanism and identify the structure of the oLPSCl. The ionic conductivity of the oLPSCl was measured to be 10^{-6} S/cm, three orders of magnitude less than that of bare LPSCl (Figure 7.5d). The presence of such a low ionic-conducting phase in addition to Ni_3S_4, LiCl and Li3PO4 results in a high interfacial impedance after charging. However, the LNO coating (on both pristine and charge NCA) prevented the above reaction; no significant blue shift was observed when the electrolyte was mixed with LNO-NCA.

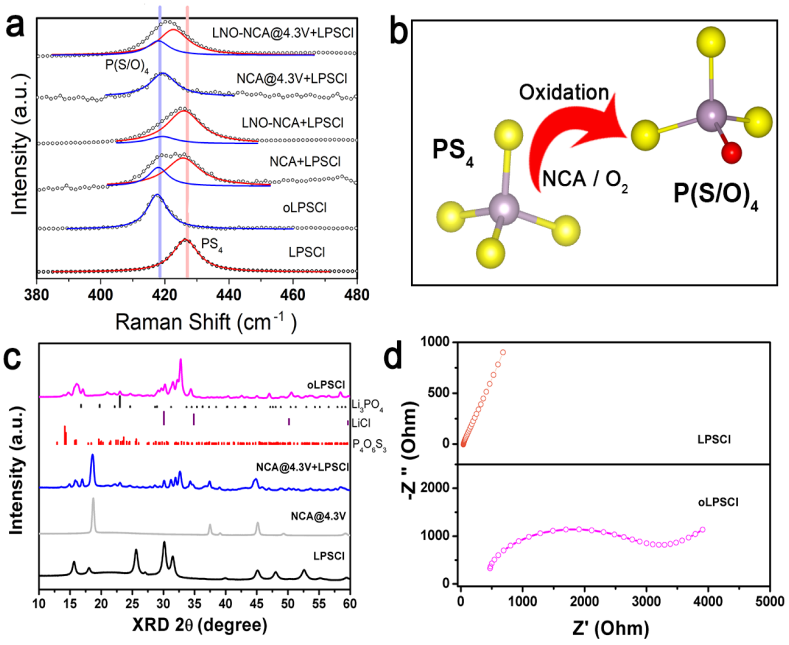

Figure 7.5. (a) Raman spectra of the oLPSCl, mixtures of the LPSCl/bare and LNO-NCA at both charged and discharged state, (b) schematic structural illustration of O doped LPSCl to form oLPSCl, (c) XRD of the oLPSCl compared with the mixture of the charged bare NCA/LPSCl and charged NCA, (d) EIS comparison between LPSCl and oLPSCl.

Although LNO coating has been proven to eliminate the chemical reaction between NCA and LPSCl, the ASSBs still have higher polarization and lower Coulombic efficiency than the liquid cell (Figure 7.6a). The charge of the ASSBs start from 3.3 V before reaching the 3.6 V plateau, where the liquid cell begins to charge. These behaviors suggest that the LPSCl is electrochemically decomposing from the beginning of the charging step since it has a narrow electrochemical stability window as predicted by the previous computational work (Figure 4b).[11]

In order to highlight the redox activity of LPSCl, LPSCl was solely used as the cathode (LPSCl/C 70:30 wt.%) of the ASSBs. A high weight percentage of carbon was used to increase the decomposition kinetics. Figure 7.6b clearly shows that the LPSCl is oxidized upon charging and delivers ~250 mAh/g capacity when the cell is charged to 4.3 V, corresponding to about 50%

of the theoretical capacity of LPSCl (449 mAh/g, assuming all lithium ions are extracted from the structure). The charging potential onset of LPSCl is similar to that of the above ASSBs. Nevertheless, it is worth noting that the oxidation of LPSCl only occurs during the first charge and no reversible capacity is achieved when the cell is discharged to 2.3V. The decomposed species produced during the charge process is suspected to terminate the continuous electrochemical decomposition of LPSCl (Figure 7.4d), indicative of a passivating, stable interphase formed by the self-limiting electrochemical decomposition of LPSCl.

XRD and in situ XAS was performed to determine the decomposed products of LPSCl (Figures 7.6c and 7.6d). The XRD pattern (Figure 7.6c) shows that sulfur (S) and LiCl are formed when the LPSCl is charged to 4.3 V while half of the LPSCl remains unreacted. In the S K-edge XANES spectra (Figure 7.6d), the gradual shift of the pre-edge to higher energy and the enhancement of the new peak at 2470 eV, assigned to elemental S,[29] suggest that the part of S in the LPSCl is continually oxidized to elemental S during charging.

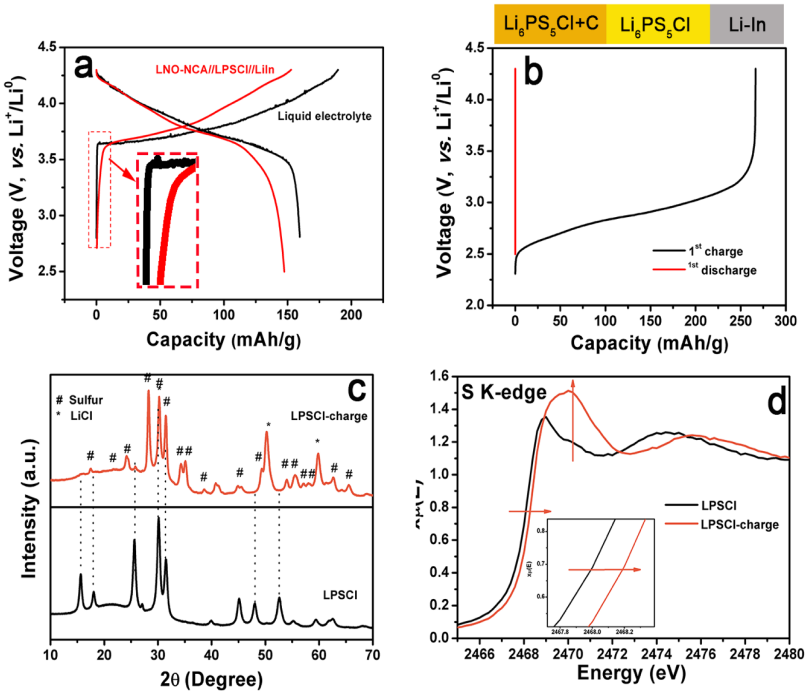

Figure 7.6. (a) Voltage profile of the LNO-NCA with solid-state electrolyte and liquid electrolyte at the first cycle, (b) voltage profile of LPSCl-conductive carbon composite (70:30, wt%), (c) XRD of bare and the charged LPSCl and (d) XAS spectra of LPSCl at different charge states.

7.6. Stable interface between LNO-NCA and LPSCl after first charge:

The above results demonstrate that a combination of the LNO coating NCA and self-limiting reaction of LPSCl will construct a stable interface between LNO-NCA and LPSCl after the first cycle. In order to visualize the cathode interface, cryogenic scanning transmission electron microscopy (cryo-STEM) was performed; cryo-protection is essential to reduce the beam damage to the sulfide electrolyte and its interface.[30,31] The results are present in Figure 7.7. Without LNO coating, part of Ni (Figure 7.7b), Co (Figure 7.7c), P (Figure 7.7d), S (Figure 7.7e) and Cl (Figure 7.7f) is prone to aggregate on the surface of the NCA particle, indicative of the interfacial reaction between NCA and LPSCl. This reaction is severe since the thickness of this interface is larger than 25 nm. Moreover, the inter-diffusion of the Co seems easier when compared with the Ni, which indicates that the Co-rich oxide cathodes, such as $LiCoO_2$ would have severer interfacial reaction than the Ni-rich oxides when they are coupled with sulfide-

based electrolyte.[10] In contrast, with LNO coating, all the elements in the cathode distribute homogeneously, suggesting the negligible interfacial reaction.

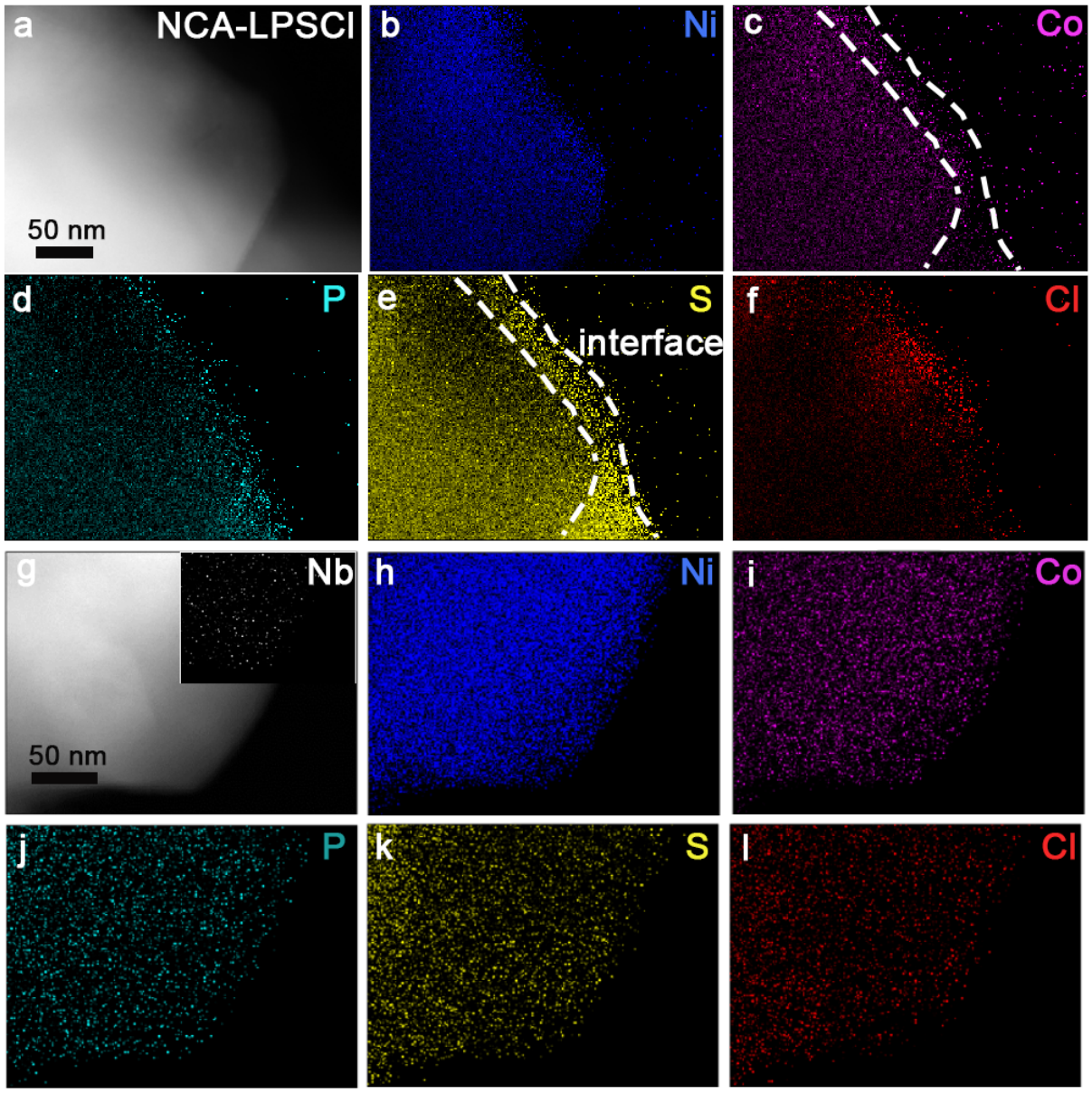

Figure 7.7. Visualized cathode interface by cryo-STEM EDS. The STEM image (a and g) and the corresponding elemental Ni (b and h), Co (c and i), P (d and j), S (e and k) and Cl (f and l) distribution at the cathode interface of the bare (a-f) and the LNO-coating (g-l) NCA.

The interface stability as a function of cycles was further explored by the XPS. As shown in Figures 7.8a and b, new peaks are found in the XPS spectra of both S 2p and P 2p after 1st

charge, which is assigned to Li_2S_x and P_2S_x species, from the electrochemical decomposition of LPSCl.[32] The intensity of these new peaks is not increased significantly after the 3rd and 50th cycle, indicating that the concentration of these decomposed products remains almost the same as after the 1st cycle. This confirms that a stable interphase formed after the 1st cycle and maintained after multicycles, a combined result from the LNO coating and the self-limiting decomposition of LPSCl. The LNO coating was evidenced to be stable to mitigate chemical reaction at the LNO-NCA/LPSCl interface and the Nb in LNO remains the same chemical state to the pristine one (Figure D7). As a result, the initial charge slope between 2.3-3.6V that originates from the electrochemical decomposition of LPSCl vanishes at the 2nd cycle (Figure 7.8c) and is absent in consecutive cycles, suggesting the presence of stable interphase between LNO-NCA and LPSCl after the 1st cycle. This ASSB cell shows excellent cycling stability with a capacity retention of (93%) for more than 100 cycles (Figure 7.8d), which exceeds all the known literature reports (Table 2).

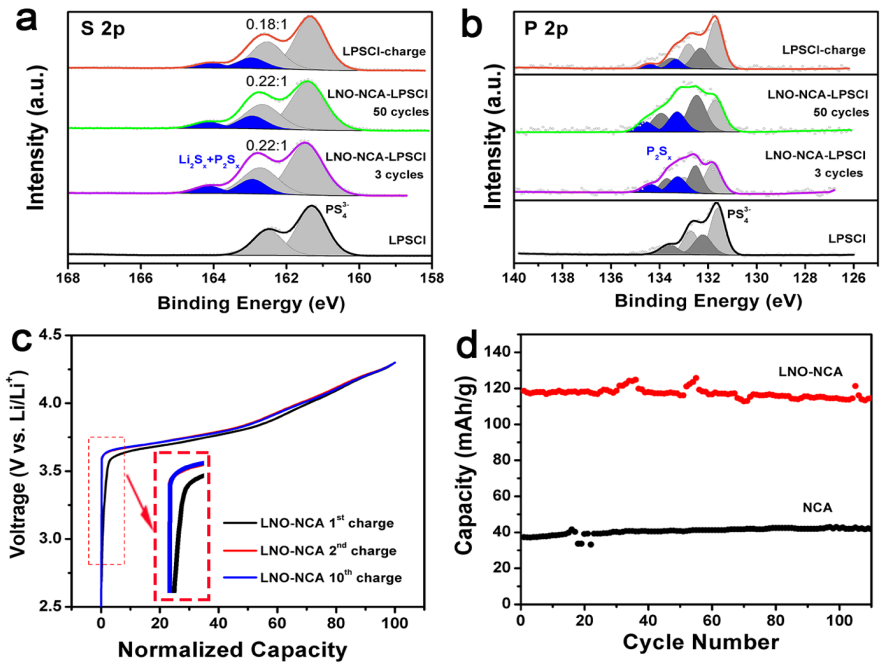

Figure 7.8. XPS spectra of S (a) and P 2p (b) of the LPSCl at different states, the charging profile (c) of LPSCl and NCA-LPSCl ASSBs at the 1st, 2nd and 10th cycle; cycling stability (d) of ASSBs for LNO-coated and bare NCA at C/3.5.

Table 7.2. Summarized electrochemical performance of the ASSBs based on the sulfide electrolytes in the literatures

Cathode	Coating	Electrolyte	Anode	Loading mg/cm2	Performance	Reference
LiNi0.8Co0.15Al0.05O2	Li2O-ZrO2	Li2SeP2S5 (80:20 mol%)	Graphite	6.8	115 mAh/g at C/10; 80 % after 100 cycle at 0.1C	33
LiNi0.8Co0.15Al0.05O2	Diamond Like carbon	Li2S-P2S5 (75:25 mol%)	Graphite	6.8	123 mAh/g at 0.05C; 91% after 100 cycle	34
LiNi0.8Co0.15Al0.05O2	Li2ZrO3	Li2S-P2S5	Li-Carbon composite	1.5	100 mAh/g at C/40; 98% after 100 cycle at C/40	35
LiNi1/3Mn1/3Co1/3O2	ZrO2	Li3PS4	Li4.4Si	1.5	120 mAh/g at 0.1 mA/cm2; 96% after 50 cycle	36
LiNi1/3Mn1/3Co1/3O2	Not mentioned	Li6PS5Cl	LiIn alloy	2.87	80 mAh/g at C/10; 75% after 300 cycles	37
LiNi0.8Co0.15Al0.05O2	Not mentioned	Li10GeP2S12	LiIn alloy	8.9	121 mAh/g at C/10; 87% after 30 cycles	38
LiNi1/3Mn1/3Co1/3O2	Not mentioned	75Li2S-25P2S5	In metal	Not mentioned	100 mAh/g at 0.13 mA/cm2; 80% after 50 cycles	39
LiNi0.8Mn0.1Co0.1O2	Not mentioned	Li3PS4	In metal	30	125 mAh/g at 0.1C; 60% after 50 cycles	40
LiNi0.8Co0.15Al0.05O2	LiNbO3	Li6PS5Cl	LiIn alloy	3.36	119 mAh/g at C/3.5; 98% after 110 cycles	This work

7.7. Discussion:

The electrochemical performance of ASSBs is mainly governed by the properties of the interfaces between the electrode and electrolyte rather than the ionic conductivity of the electrolytes. The ionic conductivity of sulfide electrolytes (e.g. 1.03 mS/cm for LPSCl) is sufficient to operate the ASSBs. Electrolytes with higher ionic conductivity but lower interphase stability will ultimately yield low Coulombic efficiency and poor cycling performance, detrimental for practical ASSBs. Therefore, constructing a stable interface with a low charge transfer resistance is essential for long-term operation of ASSBs.

The high interfacial resistance between the high-voltage oxide cathode and sulfide electrolyte can be originated from both the electrochemical decomposition of electrolyte, and the chemical reaction between electrode material and electrolyte (Figure 7.10). Our results show that the LPSCl is intrinsically incompatible with bare NCA and worse with the charged NCA, resulting in instant chemical reactions between them. Ni_3S_4, LiCl, Li_3PO_4 and oLPSCl are formed as a consequence, suggesting interionic diffusion between NCA and LPSCl, instead of solely the non-Faradic diffusion of Li^+ proposed previously.[41] The presence of these species contributes to large charge transfer resistance at the interface. This can be avoided when LNO was coated on the surface of the NCA which prevented the direct contact between NCA and LPSCl, and highlights the importance of such a buffer layer.

The properties and other potential coating materials were further screened by the DFT calculations (Figure 7.9) in terms of the reaction energies with NCA (E_{rxn}^{NCA}) and with LPSCl SE (E_{rxn}^{SE}) in eV/atom, volume change after reacting with NCA (ΔV^{NCA}) and SE (ΔV^{SE}), diffusion channel radius (R_c) in Å as an indicator of ionic diffusivity, bandgap (E_g) in eV and energy above hull (Ehull) in eV/atom.[42] A good coating candidate should be chemical and electrochemical stable with both cathode (e.g. NCA) and electrolyte (e.g. LPSCl), and ability to conduct both Li ion and electron. Based on these criteria, $Li_4Ti_5O_{12}$, $LiAlO_2$, Li_2SiO_3 and $Li_2La_2Ti_3O_{10}$ are also promising alternatives with a high oxidation limit and negligible (electro)chemical reaction with high-voltage cathodes and sulfide electrolytes. By contrast, Li_2PNO_2 is not stable with NCA while the $Li_7La_3Zr_2O_{12}$ has a low oxidation window (2.9 V). Among them, addition to the sluggish kinetics at this coated interface, the higher oxidation limit 3.88V vs. Li/Li^+ making LNO an outstanding coating materials for high-voltage cathode.

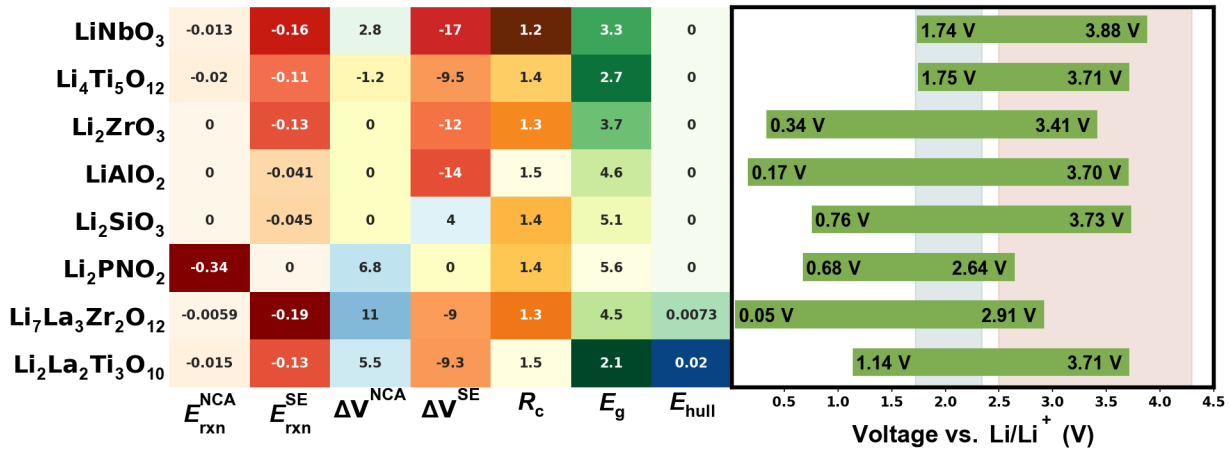

Figure 7.9. Screen of some coating materials at NCA/LPSCl interface. Left: Properties related to interfacial reactivity. From left to right, the terminologies are reaction energies with discharged NCA (E_{rxn}^{NCA}) and with LPSCl SE (E_{rxn}^{SE}) in eV/atom, percentages of volume change after reacting with NCA (ΔV^{NCA}) and SE (ΔV^{SE}), diffusion channel radius (R_c) in Å, bandgap (E_g) in eV and energy above hull (Ehull) in eV/atom. Right: The electrochemical windows of selected coatings; the LPSCl electrochemical window and NCA voltage range are labeled as blue and red ribbons for reference purpose.

Due to the nature of the sulfide electrolytes with narrow electrochemical stability windows, the electrochemical decomposition of sulfides is inevitable. Although it is unfavorable to lose some of the electrolyte, it is very beneficial to form a stable passivation layer which blocks the continuous decomposition of the electrolyte. The insulating nature of the SEI (LiCl, S and P_2S_x) as well as the sluggish kinetics for further decomposition (Figure 7.4d), helps to effectively widen the operating potential and elongate the cycling life.[27]

Overall, both the chemical reaction between NCA and LPSCl and the electrochemical decomposition of LPSCl contribute to increasing the interfacial resistance between the cathode and sulfide electrolyte (Figure 10). LNO coating is able to prevent the chemical reaction between NCA and LPSCl but not the electrochemical decomposition of LPSCl, which is inevitable, but self-passivating after the first charge. As a result, this combination of the LNO coating and self-passivation of LPSCl forms a stable interphase in the subsequent cycles, leading to excellent

cycling stability of the ASSBs. If we can further optimize the cell configuration, an energy density up to 400 Wh/kg is achievable according to the estimation based on Table D4.

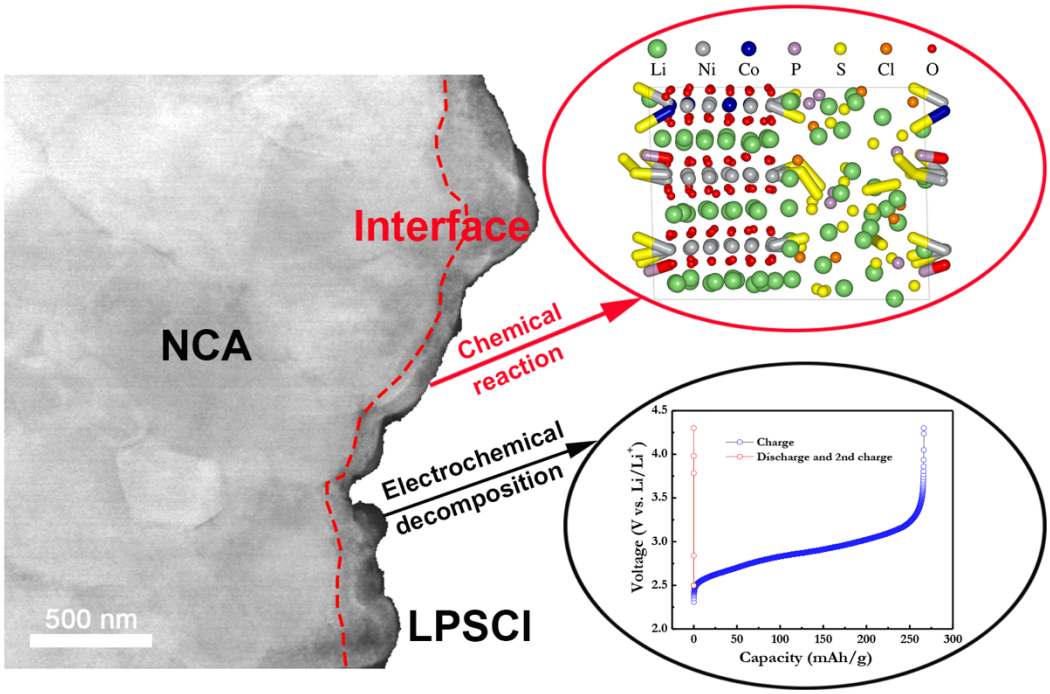

Figure 7.10. Schematic image demonstrating the chemical reaction between NCA and LPSCl and the electrochemical decomposition of LPSCl.

7.7. Conclusion

In conclusion, this work succeeded to contrast a stable interface between NCA and LPSCl and separated the contribution from the chemical reaction between NCA and LPSCl and the electrochemical decomposition of LPSCl. A combination of XRD, XAS, XPS, Raman and cryo-TEM was used to identify the interfacial reaction products. Ni_3S_4, LiCl, Li_3PO_4 and oLPSCl are formed as a consequence of spontaneous chemical reaction between NCA and LPSCl, which was shown to be thermodynamically favorable DFT calculation. Coating NCA with LNO prevented such chemical reactions. The electrochemical decomposition of LPSCl occurs at the first cycle and will be passivated by its interfacial products at the subsequent cycling. Therefore, a stable interphase between NCA and LPSCl will form, leading to excellent cycling stability of

the ASSBs. These findings clarify the reaction mechanism of both the electrochemical decomposition of NCA and the chemical reaction between NCA and LPSCl for the first time. The approaches to mitigate the side reactions highlight the importance of the buffer layer and self-limiting decomposition of electrolyte, and enlighten the capability to engineer a stable interphase between the solid electrolyte and cathode materials.

The authors acknowledge the funding support from Seeding fund from Sustainable Power and Energy Center (SPEC). XPS and TEM was performed at the University of California, Irvine Materials Research Institute (IMRI) using instrumentation funded in part by the National Science Foundation Major Research Instrumentation Program under Grant CHE-1338173. We thank Dr. Curtis Moore and Dr. Milan Gembicky at the Crystallography Facility at the University of California, San Diego for assisting on the capillary XRD data collection. The characterization work was performed in part at the San Diego Nanotechnology Infrastructure (SDNI), a member of the National Nanotechnology Coordinated Infrastructure, which is supported by the National Science Foundation under Grant ECCS-1542148. S.P.O. and H.T. acknowledge funding from the Shell, as well as computing resources provided by Triton Shared Computing Cluster (TSCC) at the UC San Diego, the National Energy Research Scientific Computing Center (NERSC) supported by U.S. Department of Energy Office of Science User Facility under the contract No. DE-AC02-05CH11231, and the Extreme Science and Engineering Discovery Environment (XSEDE) supported by the National Science Foundation under Grant ACI-1548562. XAS measurements were carried out at beamline 9-BM of the Advanced Photon Source, a U.S. Department of Energy (DOE) Office of Science User Facility operated for the DOE Office of Science by Argonne National Laboratory under Contract No. DE-AC02-06CH11357.

Chapter 7, in full, is currently being prepared for submission for publication "Nanoscale Solid-Solid Interfacial Engineering to Enable High Energy All-Solid-State Batteries." Banerjee, A., Tang, H., Wang, X., Cheng, J., Zhang, M., Nguyen, H., Wynn, T., Wu, E., Doux, J.M., Dsouza, M., Ong, S.P., Meng, Y.S. The dissertation author was a co-author of this paper. The dissertation author performed XRD and Raman experiments, and discussed results of this paper.

Chapter 8 Enabling A Room Temperature All Solid State Lithium Metal Battery Through Critical Stack Pressure

8.1. Introduction

Lithium metal anode is considered to be the "Holy Grail" electrode to be used in batteries due to its low reduction potential (-3.04 V) and high specific capacity (3800 mAh/g). However, many technical and fundamental hurdles are still left resolved with the use of this metal for secondary batteries. Such issues still prevalent are dendritic formation of the metal leading to internal shorts. This could have catastrophic consequences as the cell can overheat through the uncontrolled energy release and thermal runaway ensues, jeopardizing consumer safety.

All solid-state electrolytes (SSE) are considered the best solutions to address many of the problems associated with the metal anode cells. It was first postulated by Monroe-Neumann that the electrolyte with a shear modulus twice that of lithium metal, would impede the propagation of the metallic dendrite and prevent internal shorting.[167,168] This set the stage for SSE as a candidate to address all cell performance issues associated with Li mental anodes. However, reports of cell failures due to internal shorting still impede progression of utilizing metallic anodes for battery applications. Failure of an all solid state cell using lithium metal as the anode range from: shorts observed in plating and stripping, first cycle short in high voltage lithium ions, internal shorting after a short series of cycling, etc. Most of which, are cells cycled at room temperature. These results clearly show that there are other parameters not accounted for with the use of lithium metal in an ASSB, and that the shear modulus is not the only parameter of importance.[169–176]

SSE, namely the inorganic thiosulfide class, has seen a lot of research interest owing to its low high ionic conductivity and low Young's modulus. This SSE is most popular to use as an

inorganic green powder and can be formed into dense separator layers. The density of the SSE can be in excess of 80% relative density. This introduces pores and grain-boundaries within the electrolyte layer. The pore size and grain boundary composition have been of great interest to materials scientist and the like, because reports have shown, that this is likely where the dendrites propagate and terminate.[169] However the scale of these features present a significant challenge to characterize.

This work focuses on the stack pressure of an ASSB of a particular form factor as a parameter to mitigate cell failure and to use lithium metal as anode.

8.2. Results and Discussion

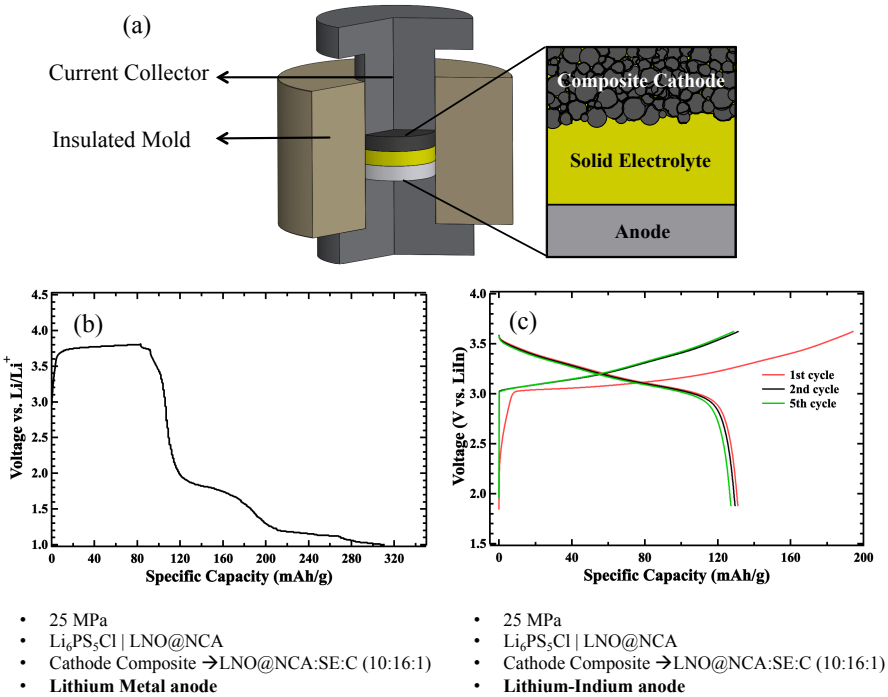

Figure 8.1. (a) Trilayer assembly of ASSB. (b) Shorting of ASSB during first charge. (c) ASSB can cycle with Li-In alloy as the anode

Figure 8.1a illustrates a typical ASSB design used to study its electrochemical performance. The pellet mold and plungers are designed to also be used as an insulating cell holder and current collectors, respectively. This design is popular because all of the solid-state

battery constituents start as loose powder and compression is needed compact them together. The higher magnification image of Figure 8.1a shows the typical tri-layer composition of the assembled ASSB. The solid electrolyte is usually compressed first to from the physical barrier between the two electrodes. The SSE is typically compressed in excess of 300 MPa to form a thin and dense layer. The composite cathode electrode is generally a mix of: active cathode material, electronic percolation diluent such as carbon, and SSE. This composite is mixed together and compressed onto one side of the SSE layer. This mixture is necessary to increase the contact area between the cathode and SSE. Unlike the conventional liquid electrolytes, the SSE is not believed to flow and adhere to surfaces of the active material. Therefore, the SSE is artificially penetrated and made into contact with the active material of the composite electrode. Therefore, cell holders are designed, such that, it provides and maintains a restoring force on the cell during cycling should contact of an interface be lost and contact is maintained. However, there are little reports of the pressure applied or it is uncontrolled.[177–180]

The anode is attached to the opposite face of the SSE and completes the battery construction. A metallic anode or alloy would be pressed on this face to form a good interface contact, while a composite anode will be made if non-metallic anodes are used, such as graphite or silicon. The pressure applied on the anode is generally lower than the cathode, if a metallic anode is used. A lower pressure is important due to the metal yielding and plastically deforming, and often result in mechanically shorting the cell.

Figure 8.1b shows a cell performance of an ASSB-Li battery held at a high stack pressure, specifically in this work, at 25 MPa. The ASSB is charged and initial platting of lithium metal proceeds. The cell is capable of delivering approximately 80 mAh/g capacity. Shortly after, the charging profile deviates from the expected of the cathode material. The

voltage profile has a sudden drop from 3.8 V to 3.7 V vs Li/Li^+ and further charging only exacerbate the behavior as the cell voltage declines to 1.0 V vs Li/Li^+ despite a charging current being applied. This cell failure is consistent with various cells reported in literature using lithium metal as the anode, and has been attributed to internal short.[180]

Figure 8.1c compares an ASSB cell constructed and tested under similar conditions, with the exception that lithium metal is replaced with lithium-indium alloy. It can be seen that the ASSB using the alloy can complete the first cycle and continued cycling without shorting. The alloy is generally chosen over the metal anode for several reasons: (1) internal shorting is avoided as the lithium remains in its ion form and plating does not occur, (2) there is also the addition that lithium-indium alloy operates 0.62 V above lithium plating potential thus guaranteeing lithium remains an ion, (3) the alloy as an anode has been shown to be chemically more stable than lithium metal at the interface.[181]

Note, the difference between the 1^{st} and 2^{nd} cycle of the ASSB with lithium-indium alloy, is due to cathodic reaction of the SSE, a phenomenon that is described in the literature and future work. The polarization of the cells after the first cycle remain the same, this is apparent due to the construction of the composite cathode and the good contact formation considerations of the cell construction.

Lithium metal is an extremely ductile metal, such that it can be easily formed or processed into any shaped. This ability of the metal to plastically deform with little resistant has led to this investigation of the stack pressure as a possible cause to the internal shorting.

A pressure monitor was added to the ASSB cell design, such that the stack pressure on the cell can be controlled, as shown cross section Figure 8.2a. A lithium metal symmetric cell

was constructed to determine if the stack pressure has a consequence on the cycling ability of the lithium metal anode with the SSE. It assembly is shown in the high magnification image.

A series of galvanostatic plating and stripping test was collected at various pressures and the results are shown in Figure 8.2b. When the stack pressure is held at 25 MPa the symmetric cell can plate and strip lithium for 40 hours total, and then a shorting event is observed from the sudden drop in the cell polarization to nearly zero. This result is the first indication that high stack pressure beyond the yield strength of lithium metal.[182] Not shown for clarity, with very high pressures in excess of 70 MPa, the cell is capable of mechanically shorting without the electrochemical cycling lithium ions through the SSE. This is attributed to lithium being very malleable at room temperature and could be forced through the SSE and internally short.

The stack pressure on the cells was lowered at 5 MPa increments and the observed platting and stripping duration is extended as a result. However, shorting is still observed down to 10 MPa and this suggest that the applied stack pressure could modulate the time required for internal shorting to occur, where higher stack pressures led to shorter internal shorting. Interestingly, as the load on the cell is reduced, the time it takes to short the cell appears to approach an asymptotic pressure of 5 MPa, and the symmetric cell set to 5 MPa was able to cycle without shorting. This implies that a critical stack pressure is required to allow long term lithium metal cycling to occur, and a maximum pressure to be applied to an ASSB using lithium metal anode is 5 MPa. The symmetric cell held at 5 MPa was able to plate and strip lithium metal at room temperature for 50 cycles with no drop in polarization signaling an internal short.

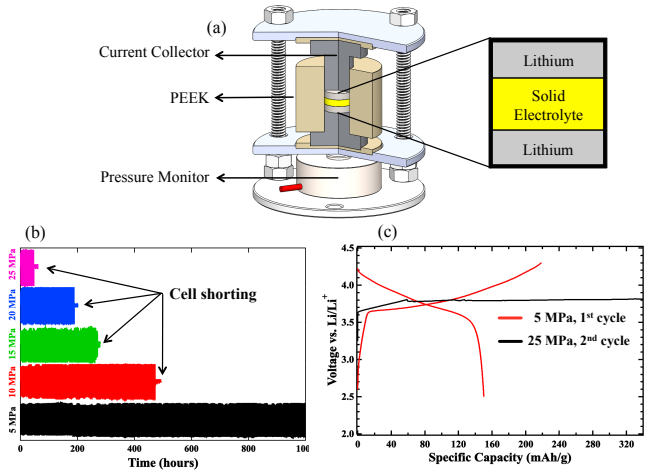

Figure 8.2. (a) ASSB with pressure monitor assembly. (b) Plating and stripping of symmetric lithium cells with varying stack pressure. (c) 1st cycle at critical stack pressure compared to 2nd cycle at high stack pressure

An ASSB was constructed as previous in Figure 1b with the exception that the stack pressure was set to 5 MPa, Figure 8.2c. Contrasting the previous cell, this ASSB successfully completed the first cycle, delivering a specific capacity of 150 mAh/g and a first cycle coulombic efficiency of 71%. The first cycle efficiency not being of 100% is due to the cathodic electrolyte decomposition occurring on the only the first cycle as mentioned above. Upon the 2nd cycle, the stack pressure was then set to 25 MPa and the ASSB was subjected to the same cycling protocol. Similar to the cell performance in Figure 8.1b, the cell was able to deliver a charging capacity of 60 mAh/g and then a drop in sudden drop at the cell voltage of 3.8 V vs Li/Li^+ was observed, and the cell failed to charge to the prescribed high voltage cutoff of 4.3 V vs. $Li\backslash Li^+$. The potential profile traced out the shorting behavior is attributed as a micro-short. Clearly, the pressure on lithium metal anode has an effect on the cyclability of ASSB and the result strongly encourages a maximum stack pressure of 5 MPa when utilizing metallic lithium as the anode.

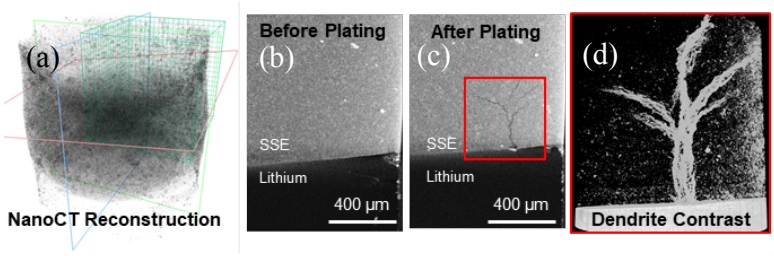

Figure 8.3. (a) X-ray computed tomography reconstruction of symmetric lithium cell. (b-c) Before and after comparison of symmetric cell. (d) Increased magnification of dendritic growth from interface

Characterization of the interfaces all-solid-state cells are non trivial as the area in question are buried in between the SSE and electrode. The buried nature of the interface proves to be a challenge to conventional surface and localized area characterization, where the area of interest will be perturbed to characterize.

X-ray computed tomography (CT) imaging is a non-destructive technique that can show the underlying changes that are occurring with continued plating and stripping of the cells, as shown in Figure 8.3. A 3D reconstructed image of the SSE LPSCL in the pellet form factor is shown in Figure 8.3a, where the dark region is the SSE and the lighter regions at top and bottom are lithium metal. The metal anode has a very low density compared to LPSCL (0.534 g cm^{-3}), and has similar scattering density as the cell holder, polycarbonate. Therefore, the contrast of the metal is very difficult to discern through this technique. Nonetheless, the SSE can be seen in the contrast image and a clear microscopic change can be observed in Figure 8.3b and 8.3c. The boundary of SSE and lithium metal can be seen in Figure 8.3b before the cell is cycled. The lighter region is determined to be the SSE and show a clean interfacial contact at this scale with lithium metal. The cell was then cycled, under 25 MPa, and shorted, and a micro structural change was observed in the same region shown in Figure 8.3c. A dendritic structure can be seen to protrude from the interface layer, into the SSE. At the base of the structure, it can be seen that

a dense base is been formed. Interpretation of this image is consistence with mossy like platting of lithium metal. Protrusion of the structure into the SSE appear to create fissures in the layer.

A magnification image in Figure 8.3d indicates that the structure not only propagates in the 2D projection, but depth direction of the SSE. This is the benefits of X-ray CT as we can reconstruct the material and find new features of dendritic growth, without destroying the material.

The fissures are attributed to the growth of lithium metal dendrites into the SSE and propagation across the SSE results in the shorting seen in the plating and stripping of symmetric cells.

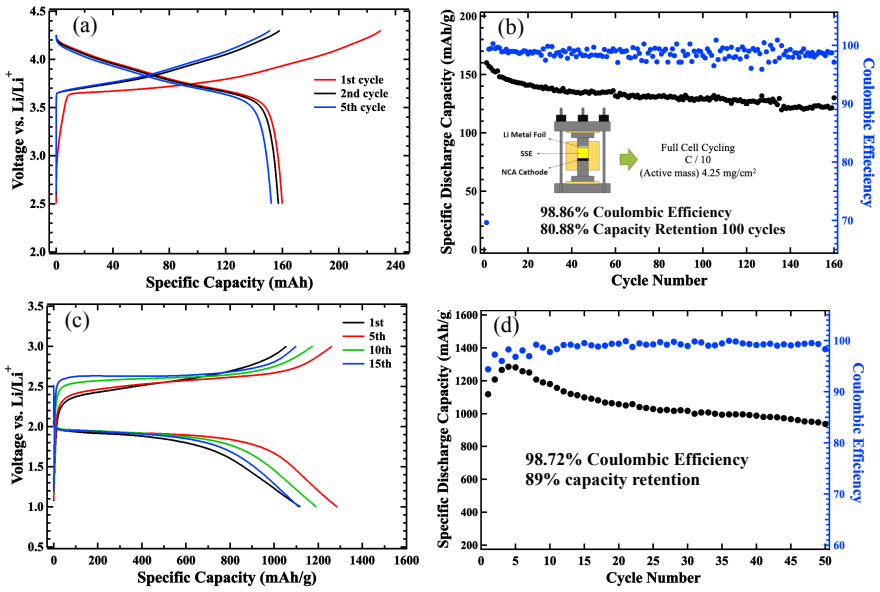

Figure 8.4. (a) NCA-Li ASSB charge/discharge and (b) prolonged cycling behaveior. (c) Room temperature Li-S and (d) prolonged cycling behavior

All solid-state lithium metal batteries were constructed at the determined critical stack pressure shown in Figure 8.4. The cell constructed with NCA cathode from Toda, Inc delivered a practical specific capacity of approximately 160 mAh/g, shown in Figure 8.4a, which is similar capacity and to the cell made with the lithium-indium alloy in Figure 1c. The cell also

demonstrated that it was capable of cycling at room temperature for more than 100 cycles without fail with a practical capacity retention of 75%, Figure 8.4b. To the best of the author's knowledge, this is the longest an ASSB has been shown to cycle with lithium metal anode.

In addition, separate cathode chemistry was demonstrated with lithium metal ASSB to ensure that the cathode is not the limiting factor along with pressure. Li-S cells were constructed and held at 5 MPa. The cell is able to cycle at room temperature providing > 900 mAh/g specific capacity with good cycling with lithium metal as the anode. This cycling behavior is very similar to work conducted by Junek et. al. where an ASSB with LiIn as the anode was demonstrated. Thus showing the lithium metal can be utilized in the ASSB at room temperature where it had been previously shown to be only achievable with other anode material.

8.3. Conclusion

This work has shown how pressure should be a consideration when constructing pelletized ASSB from powder constituents. Lithium metal is a ductile and malleable metal and its ability to plastically deform under high mechanical strain is detrimental to battery operations. A critical stack pressure of the cell was determined to be 5 MPa. This would had demonstrated that lithium metal is capable of long term cycling in ASSB construction, thereby increasing the overall energy density of the cells. The work here is to demonstrate that cycling lithium metal in ASSB is now capable.

This work does not claim to have prevented dendrite formation and shorting the cell, instead fact we wish to submit this work to inform the battery community that the stack pressure applied to a lithium metal cell needs to be considered and it's likely mitigated through pressure conditions.

8.4. Experimental Section

All materials synthesis, processing, and testing was conducted in an Argon glovebox (mBruan) with H_2O and O_2 levels below 0.1 and 0.5 ppm, respectively.

Li_6PS_5Cl solid-state electrolyte used in this work was purchased directly from NEI Corporation. Lithium metal electrodes were punched to size from ribbons (FMC Lithium, 0.5 mm thick). The high voltage cathode material used in this study was $LiNi_{0.80}Co_{0.15}Al_{0.05}O_2$ (NCA) (Toda, Inc.) and coated with $LiNbO_2$ (LNO) by an in-house wet synthesis method. Sulfur (Sigma Aldrich, 99.99%) cathode was prepared by ball milling with AB for 550 rpm and 1 hour. Li_6PS_5Cl was then hand mixed in with the sulfur-carbon mix to form a composite cathode electrode.

Symmetric cell construction consisted of 200 mg of solid-electrolyte powders compressed into a 13 mm diameter PEEK mold with titanium plungers. The electrolyte thickness was found to be approximately 1 mm. The powder was compressed to 360 MPa at room temperature. The solid-electrolyte separator was determined to be 80% dense compared to theoretical. Lithium metal was cleaned, punched to size, and added to both sides of the solid-electrolyte. The constructed cell was then pressed to 25 MPa and quickly released to form a good interfacial contact at the solid-electrolyte/electrode interface. The cell stack pressure was then set to prescribed values of 5, 10, 15, 20, 25 MPa during plating and stripping test. The current density was 75 uA/cm^2 for all stack-pressures.

All solid-state battery full cell construction consisted of 200 mg solid electrolyte powder loaded into a 13 mm PEEK mold and compressed to 360 MPa at room temperature. Composite cathodes were then compressed to 360 MPa on one side of the solid-electrolyte to form good contact with the solid-electrolyte/cathode interface. Lithium metal was cleaned and cut to a

diameter of 13 mm was then added onto the other face of the solid-electrolyte and pressed to 25 MPa and released, to form good interfacial contact. The pressure on the cell was then brought back to and held at either 25 MPa or 5 MPa during cycling.

All cells were cycled using Landhe battery cyclers.

Chapter 8, in full, is currently being prepared for submission for publication ―Enabling A Room Temperature All Soild-State Lithium Metal Battery. **Nguyen, H.,** Doux, J.M., Tan, D., Banerjee, A., Wang, X., Wu,, E.A., Jo, C., Meng, Y.S. The dissertation author is the co-primary investigator and author of this paper. The author conducted all the experimental test and analysis in this work.

Chapter 9 Summary and Future Work

SSE has been demonstrated as an ideal alternative of LE and making LIBs safe and potentially achieves higher energy densities than current advanced batteries. The former can be achieved because SSE is non-flammable and considered to be thermally stable where LE have been shown to have catastrophic results. The latter can be achieved because SSE can suppress dendrite propagation to prevent internal shorting and reversibly cycle with lithium metal anodes.

Chapter 3 and 4, introduces new classes of SSE, Na_3OBr and $Li_7P_3S_{11}$ have shown that their power capabilities can be improved or processed to comparable performance as advance LE. SSE consists of rigid anion framework thereby mobile cation species can diffuse. However, it is important that point defects are present in the material such that ions have a vacant position to traverse to. It was shown that reduction of grain-boundary impedance will improve the overall conductivity of the SSE and is an important process to measure true bulk properties of the SSE. In the SSE containing the sulfur chemistry, post processing has very beneficial results owing to their larger polarizability and it makes it easier to process.

In Chapter 5, the optimal synthesis and processes conditions were determined for Na_3PS_4 SSE and make it viable for scale-up process to make large batch of materials. A comparison of the SSE electronic and ionic conductivity showed that its former property is six orders of magnitude lower, which make the SSE ideal insulator for ASSB. Through the careful analysis of the each parameter of SSE synthesis, an optimized protocol was determined and increased the yield of Na_3PS_4 by 50 through a single-step synthesis.

In chapter 6, strategies to improve the ionic conductivity of an SSE was demonstrated with the combine effort of computation and experiment. Tetragonal Na_3PS_4 was discovered as an electrolyte for sodium battery applications, however it was shown to have low ionic conductivity

when first evaluated. A common strategy to improve the overall conductivity of SSE are to dope the bulk structure and increase the point defects of the SSE, thereby increasing its power capability, without altering its overall microscopic structure. Through aliovalent doping with halogen ions, production of point defects to increase the concentration of mobile sodium ions. Through the high-throughput prediction from First-Principles, aliovalent doping with halogen ions was predicted to increase NPS conductivity to the order of 10^{-3} S cm^{-1}. Leveraging the prediction from simulation it was demonstrated to match experimental observations.

In chapter 7, the complex reactions occurring at the cathode/SSE interface was eluded. The cell can suffer from severe oxidative parasitic reactions between the cathode and SSE and adversely degrade the overall ASSB performance by increased resistance and active species lost. The interface decomposition can be reduced through proper buffer layer and carbon considerations. It was also determined that the electrolyte decomposes much earlier than reported in literature, through the use of modified cell design. The true electrolyte decomposition onset of sulfur containing SSE was determined to be ~2 V vs. lithium, and contributes to excess charging capacity, only on the first charge.

In chapter 8, lithium metal anode is demonstrated with ASSB for reversible long-term cycling by determining the critical stack pressure on the cell. With the use of x-ray tomography, evidence of the internal processes occurring with ASSB and lithium was eluded under normal plating and stripping conditions. Fissures were observed in the interior of the SSE and cell shorting as a result. Through in-situ XRD of the cells, the complex SEI produced from the chemical reactions of lithium metal and SSE was determined and matches predictive computation.

Given the findings in the work towards a safe and reliable ASSB, there are several aspects of the ASSB that can still be improved on and reserved for future work.

The overall energy density of ASSB is significantly dependent on the thickness of the SSE layer. Thin and flexible SSE layers are ideal for easy adoption into current battery manufacturing.

Versatile geometries of ASSB form factors are now possible with formability of the SSE layer can be made to fit any individual needs and designs. New form factor of ASSB could see applications in wearable electronics.

Sodium metal has very similar properties as lithium metal. It is a ductile and malleable metal just as lithium. It's standard reduction potential is -2.71 V vs. SHE compared to lithium metals -3.04 V vs. SHE. Similar dendritic growth and shorting results are shown with all-solid-state sodium metal batteries. Therefore, it is reasonable that all mechanical considerations with lithium metal can be transferred to sodium ASSB.

Moreover, sodium metal is detectable with nearly all techniques in use for my dissertation, where lithium proved difficult due to its low density. Sodium metal is more aggressive metal than lithium and can readily reacted with SSE electrolytes, however, it is expected that the SEI produces from the chemical reaction are similar chemistries, such as, Li_3P and Na_3P are expected to form. Through the aggressive nature of Na, there will need to be a mitigation strategy to stabilize not only dendrites, but also the chemical stability.

Appendix A Supporting Information for Chapter 3

A.1. Phonon Spectrum

Figure A.1a and A.1b show the phonon spectrum and projected phonon density of states for $Li_7P_3S_{11}$. In the low frequency regime that is less than 5 THz, S atoms provide the dominant contributions over those from P and Li atoms. This is likely due to the larger atomic mass of S than Li and P, and also the fraction of S in the unit cell is much higher than that of P. Note that Figure A.1a shows that the lowest-frequency band contains negative values between Z and Y. These are known as the imaginary frequencies, of which the phonon modes tend to introduce instability to the compound studied when the atoms are displaced along those phonon modes. We confirmed that such imaginary frequencies are indeed due to the numerical errors using the approach of structure modulation (see Figure A.1c). In particular, we modulated the structure by displacing the atoms along the direction of a given phonon mode associated with the imaginary frequency, and the total energy calculations were performed for the modulated structures. It is clear from the figure that the initial structure is energetically stable against the modulation. Therefore, we conclude that the obtained imaginary frequencies are due to the numerical errors and that $Li_7P_3S_{11}$ is indeed thermodynamically stable.

A.2. Calculation of Thermodynamical Properties

For the solid at fixed volume, the thermodynamic properties can be estimated using the phonon energies that depend on the frequencies, and the lattice internal energy from density functional theory (DFT) calculation at 0 K. The Gibbs free energy at temperature T and volume V reads $G(V, T) = U_L(V) + U_v(V, T) - TS(V, T) + PV$, where $U_v(V, T)$ and $S(V, T)$ are the vibrational internal energy and vibrational entropy from phonon contributions, respectively. $U_L(V)$ is the lattice internal energy and P is the external pressure. Uv and S can be expressed as follows,[183]

$$U_v(V, T) = \sum_{qj} \hbar\omega_{qj} \left[\frac{1}{2} + \frac{1}{\exp[\hbar\omega_{qj}/k_b T]-1}\right] \quad (1)$$

$$S(V, T) = -k_b \sum_{qj} \log[1 - \exp(-\hbar\omega_{qj}/k_b T)] - \frac{1}{T}\sum_{qj} \frac{\hbar\omega_{qj}}{\exp[\frac{\hbar\omega_{qj}}{k_b T}-1]} \quad (2)$$

Here, $\omega_{q,j}$ is the phonon frequency at wave vector q and band index j. Its dependence on the volume is not shown for simplicity. k_b and $\hbar$ are Boltzmann constant and Planck constant, respectively. When estimating the transition temperature of $Li_7P_3S_{11}$ from γ-Li_3PS_4 and P_2S_5, we first computed the phonon energies for each compound. Then the Gibbs free energy change $\Delta G(V, T)$ was calculated in which the P V term is neglected due to its small contribution.

A.3. Van Hove Correlation Function

The van Hove correlation function (G) is often adopted for the investigations of the highly correlated ionic motions.[84] G can be split into the self-part G_s and the distinct-part G_d and expressed as follows.

$$G_s(r, t) = \frac{1}{4\pi r^2 \rho N_d} \langle \sum_{i=1}^{N_d} \delta(r - |r_i(t_o) - r_i(t + t_o)|) \rangle_{t_o} \quad (3)$$

$$G_d(r, t) = \frac{1}{4\pi r^2 \rho N_d} \langle \sum_{i\neq j}^{N_d} \delta(r - |r_i(t_o) - r_j(t + t_o)|) \rangle_{t_o} \quad (4)$$

Here, δ() is the one-dimensional Dirac delta function. The angular bracket stands for the ensemble average over the initial time t_0, $r_i(t)$ denotes the position of the i_{th} particle at time t. N_d, r are the number of particles, i.e. diffusing lithium ions in the unit cell and radial distance, respectively. For given r and t, $G_s(r,t)$ describes how probable a particle diffuses away from its initial position by a distance of r after time t, whereas Gd(r,t) describes the radial distribution of N - 1 particles after time t with respect to the initial reference particle. In particular, $G_d(r,t)$ is reduced to the static pair distribution function when t = 0.

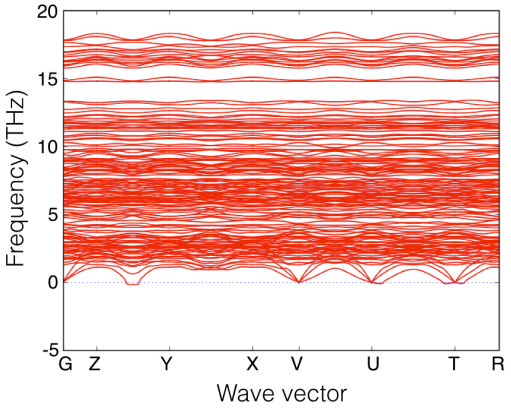

(a)

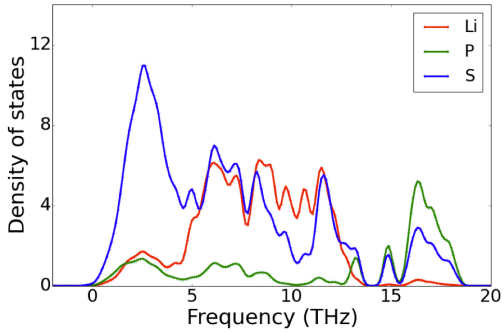

(b)

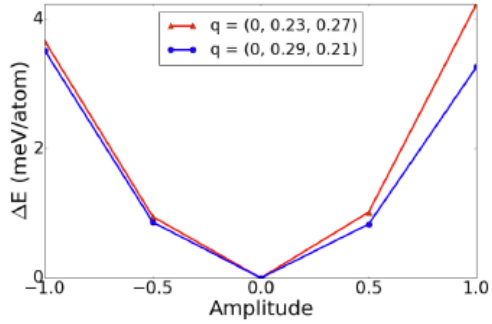

(c)

Figure A.1. (a) Phonon spectrum and (b) projected phonon density of states of $Li_7P_3S_{11}$. (c) Total energy versus amplitude associated with the structural modulation using two randomly selected unstable phonon modes.

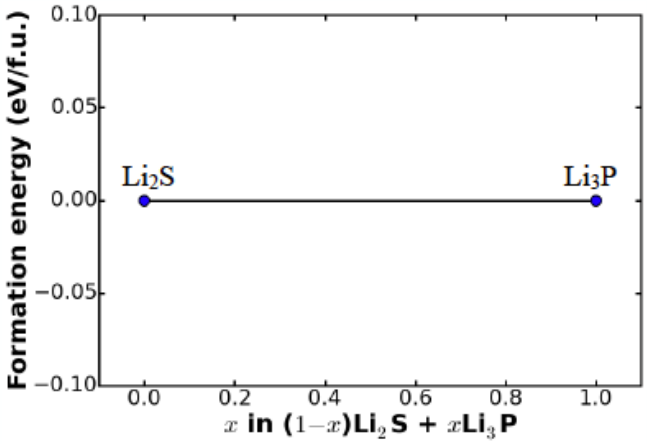

(a)

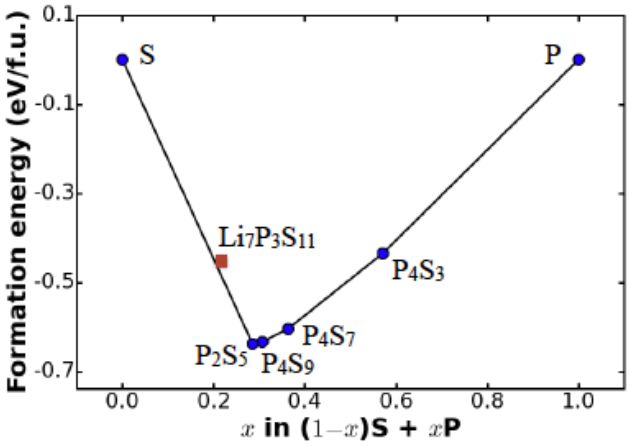

(b)

Figure A.2. Lithium grand potential phase diagrams at (a) Li metallic anode with $\mu = \mu^0$, and (b) a charged 5V cathode with $\mu = \mu^0 - 5eV$. Here μ^0 is the chemical potential of bulk Li.

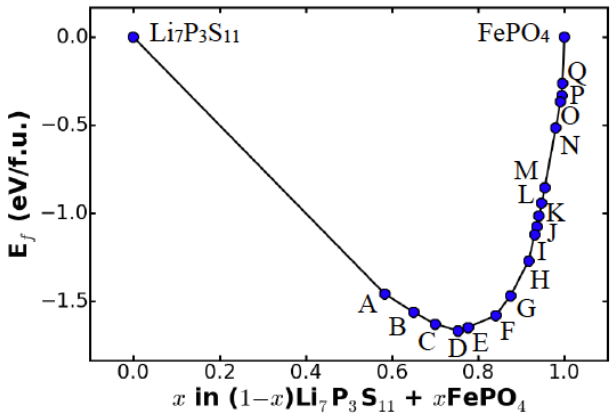

Figure A.3.Pseudo-binary phase diagram between $Li_7P_3S_{11}$ and olivine $FePO_4$ charged cathode.

Table A.1 Phase equilibra of $Li_7P_3S_{11}$ at olivine $FePO_4$ charged cathode as labeled in Figure A.3

Label	x	Phase equilibra
A	0.5833	$0.2917\ Li_4P_2S_6 + 0.3333\ P_2S_5 + 0.5833\ FeS_2 + 0.5833\ Li_3PO_4$
B	0.6500	$0.2000\ P_4S_9 + 0.1250\ Li_4P_2S_6 + 0.6500\ FeS_2 + 0.6500\ Li_3PO_4$
C	0.7000	$0.1625\ P_4S_9 + 0.0625\ P_4S_7 + 0.7000\ FeS_2 + 0.7000\ Li_3PO_4$
D	0.7538	$0.0481\ P_4S_9 + 0.1096\ P_4S_7 + 0.4308\ Li_4P_2O_7 + 0.7538\ FeS_2$
E	0.7765	$0.1294\ P_4S_7 + 0.3176\ Li_4P_2O_7 + 0.2941\ LiPO_3 + 0.7765\ FeS_2$
F	0.8400	$0.0255\ P_4S_7 + 1.1200\ LiPO_3 + 0.7909\ FeS_2 + 0.0491\ FeP_2$
G	0.8750	$0.7292\ LiPO_3 + 0.1458\ LiFe(PO_3)_3 + 0.6875\ FeS_2 + 0.0417\ FeP_2$
H	0.9167	$0.0833\ Li_2Fe_3(P_2O_7)_2 + 0.2083\ LiPO_3 + 0.2083\ LiFe(PO_3)_3 + 0.4583\ FeS_2$
I	0.9310	$0.0690\ Li_2Fe_3(P_2O_7)_2 + 0.1724\ LiFeP_2O_7 + 0.1724\ LiFe(PO_3)_3 + 0.3793\ FeS_2$
J	0.9355	$0.2258\ LiFeP_2O_7 + 0.1290\ LiFe_2P_3O_{10} + 0.0968\ LiFe(PO_3)_3 + 0.3548\ FeS_2$
K	0.9412	$0.0882\ Fe(PO_3)_2 + 0.2941\ LiFeP_2O_7 + 0.1176\ LiFe_2P_3O_{10} + 0.3235\ FeS_2$
L	0.9474	$0.0789\ Fe(PO_3)_2 + 0.3684\ LiFeP_2O_7 + 0.1053\ Fe_2P_2O_7 + 0.2895\ FeS_2$
M	0.9545	$0.3182\ LiFeP_2O_7 + 0.0682\ Fe_3(P_2O_7)_2 + 0.0909\ Fe_2P_2O_7 + 0.2500\ FeS_2$
N	0.9800	$0.1350\ Fe_3(P_2O_7)_2 + 0.2500\ Fe_2P_2O_7 + 0.0750\ FeS_2 + 0.0700\ Li_2SO_4$
O	0.9909	$0.0955\ Fe_3(P_2O_7)_2 + 0.3182\ Fe_2P_2O_7 + 0.0682\ FeSO_4 + 0.0318\ Li_2SO_4$
P	0.9931	$0.1207\ Fe_3(PO_4)_2 + 0.1931\ Fe_3(P_2O_7)_2 + 0.0517\ FeSO_4 + 0.0241\ Li_2SO_4$
Q	0.9953	$0.0814\ Fe_7(PO_4)_6 + 0.1302\ Fe_3(P_2O_7)_2 + 0.0349\ FeSO_4 + 0.0163\ Li_2SO_4$

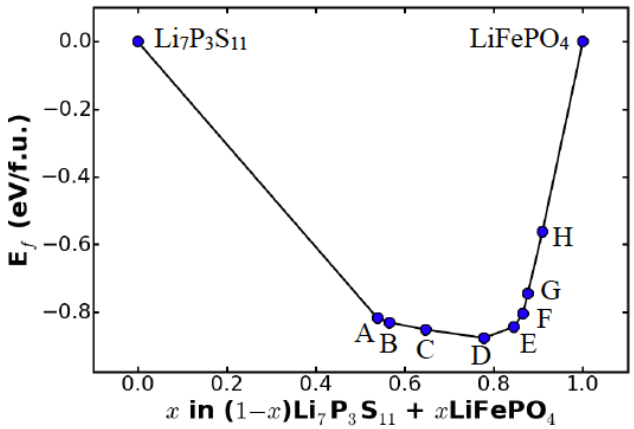

Figure A.4. Pseudo-binary phase diagram between $Li_7P_3S_{11}$ and olivine $FePO_4$ discharged cathode.

Table A.2. Phase equilibra of $Li_7P_3S_{11}$ at olivine $FePO_4$ discharged cathode as labeled in Figure A.4

Label	x	Phase equilibra
A	0.5385	$0.5385\ Li_4P_2S_6 + 0.1538\ P_2S_5 + 0.5385\ FeS_2 + 0.5385\ Li_3PO_4$
B	0.5652	$0.0870\ P_4S_9 + 0.4783\ Li_4P_2S_6 + 0.5652\ FeS_2 + 0.5652\ Li_3PO_4$
C	0.6471	$0.1176\ P_4S_7 + 0.2941\ Li_4P_2S_6 + 0.6471\ FeS_2 + 0.6471\ Li_3PO_4$
D	0.7778	$0.1414\ P_4S_7 + 0.7273\ FeS_2 + 0.0505\ FeP_2 + 0.7778\ Li_3PO_4$
E	0.8448	$0.0329\ P_4S_7 + 0.4828\ Li_4P_2O_7 + 0.7382\ FeS_2 + 0.1066\ FeP_2$
F	0.8652	$0.3933\ Li_4P_2O_7 + 0.2360\ LiPO_3 + 0.7416\ FeS_2 + 0.1236\ FeP_2$
G	0.8761	$0.3451\ Li_4P_2O_7 + 0.3628\ LiPO_3 + 0.6814\ FeS_2 + 0.1947\ FeP$
H	0.9091	$0.0887\ Li_2Fe_3(P_2O_7)_2 + 0.3420\ Li_4P_2O_7 + 0.5000\ FeS_2 + 0.1429\ FeP$

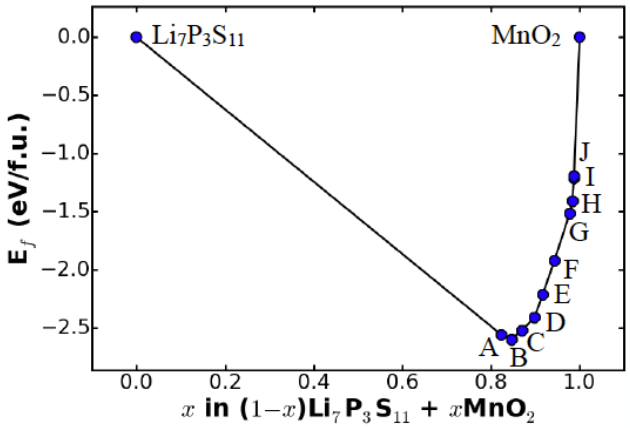

Figure A.5. Pseudo-binary phase diagram between Li7P3S11 and spinel Mn2O4 charged cathode. Note that the compositional ratio is referenced to MnO2 rather than Mn2O4 when constructing the phase diagram.

Table A.3. Phase equilibra of Li7P3S11 at spinel Mn2O charged cathode as labeled in Figure A.5.

Label	x	Phase equilibra
A	0.8235	$0.8235\ MnS_2 + 0.0588\ P_2S_5 + 0.4118\ Li_3PO_4$
B	0.8462	$0.1538\ Li_4P_2O_7 + 0.8462\ MnS_2 + 0.1538\ Li_3PO_4$
C	0.8696	$0.1739\ LiMnPO_4 + 0.0435\ Li_2SO_4 + 0.6957\ MnS_2 + 0.2174\ Li_3PO_4$
D	0.8980	$0.3265\ Mn_2S_3 + 0.2449\ LiMnPO_4 + 0.1429\ Li_2SO_4 + 0.0612\ Li_3PO_4$
E	0.9167	$0.2500\ Mn_2S_3 + 0.2500\ LiMnPO_4 + 0.1667\ Li_2SO_4 + 0.1667\ MnO$
F	0.9429	$0.1429\ Mn_2S_3 + 0.2000\ Li_2SO_4 + 0.4000\ MnO + 0.0857\ Mn_3(PO_4)_2$
G	0.9778	$0.1667\ MnSO_4 + 0.0778\ Li_2SO_4 + 0.7111\ MnO + 0.0333\ Mn_3(PO_4)_2$
H	0.9836	$0.2623\ Mn_3O_4 + 0.1230\ MnSO_4 + 0.0574\ Li_2SO_4 + 0.0246\ Mn_3(PO_4)_2$
I	0.9870	$0.4156\ Mn_2O_3 + 0.0974\ MnSO_4 + 0.0455\ Li_2SO_4 + 0.0195\ Mn_3(PO_4)_2$
J	0.9873	$0.0382\ Mn_2PO_5 + 0.4076\ Mn_2O_3 + 0.0955\ MnSO_4 + 0.0446\ Li_2SO_4$

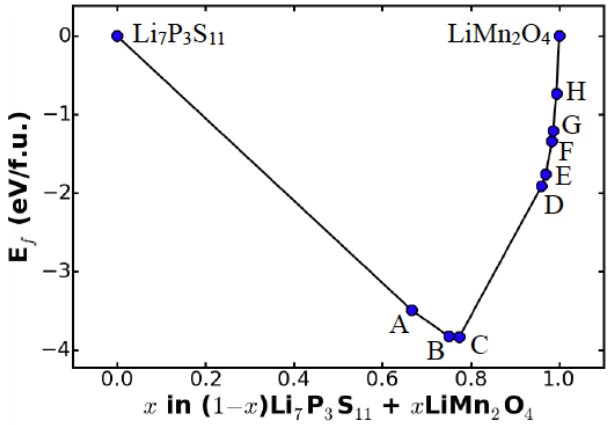

Figure A.6. Pseudo-binary phase diagram between Li7P3S11 and spinel Mn2O4 discharged cathode.

Table A.4. Phase equilibra of Li7P3S11 at spinel LiMn2O4 discharged cathode as labeled in Figure A.6.

Label	x	Phase equilibra
A	0.6667	$0.3333\ Mn_2S_3 + 0.3333\ Li_3PS_4 + 0.6667\ MnS_2 + 0.6667\ Li_3PO_4$
B	0.7500	$0.3750\ Mn_2S_3 + 0.7500\ MnS_2 + 0.1250\ Li_2S + 0.7500\ Li_3PO_4$
C	0.7742	$0.7742\ Mn_2S_3 + 0.0968\ Li_2SO_4 + 0.0645\ Li_2S + 0.6774\ Li_3PO_4$
D	0.9600	$0.3600\ Li_2SO_4 + 1.9200\ MnO + 0.0800\ Li_2S + 0.1200\ Li_3PO_4$
E	0.9697	$0.2424\ LiMnO_2 + 0.3333\ Li_2SO_4 + 1.6970\ MnO + 0.0909\ Li_3PO_4$
F	0.9836	$0.4590\ Mn_3O_4 + 0.5902\ LiMnO_2 + 0.1803\ Li_2SO_4 + 0.0492\ Li_3PO_4$
G	0.9863	$0.5479\ Mn_3O_4 + 0.1507\ Li_2SO_4 + 0.3288\ Li_2MnO_3 + 0.0411\ Li_3PO_4$
H	0.9935	$0.7843\ Mn_2O_3 + 0.0719\ Li_2SO_4 + 0.4183\ Li_2MnO_3 + 0.0196\ Li_3PO_4$

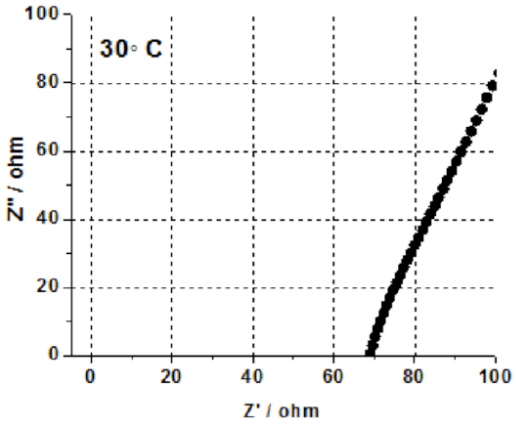

Figure A.7. Cold-pressed Li7P3S11 glass-ceramic Nyquist curve

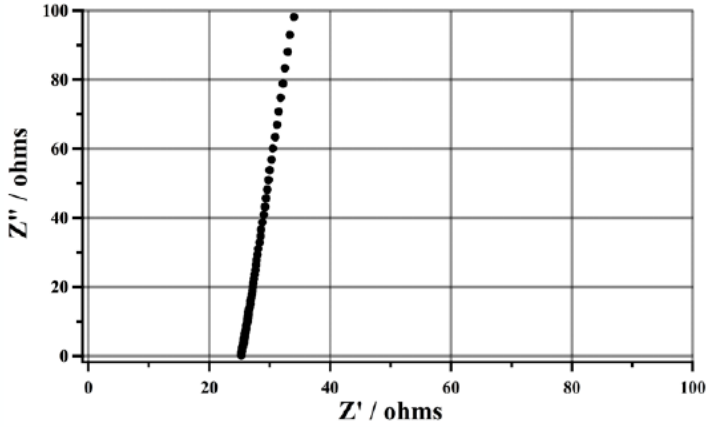

Figure A.8. SPS Li7P3S11 glass-ceramic Nyquist curve.

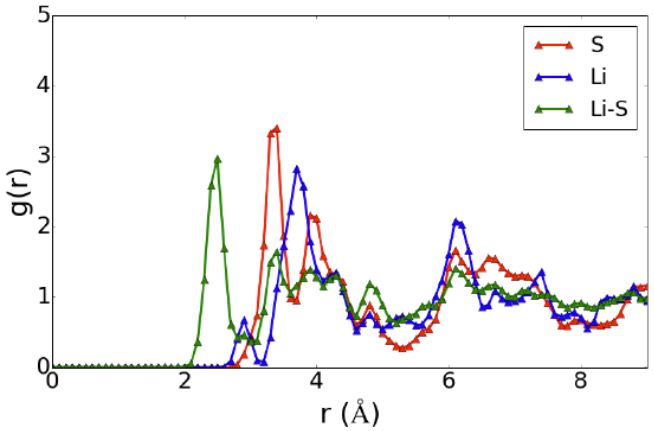

Figure A.9. Static pair distribution function of the initially relaxed Li7P3S11

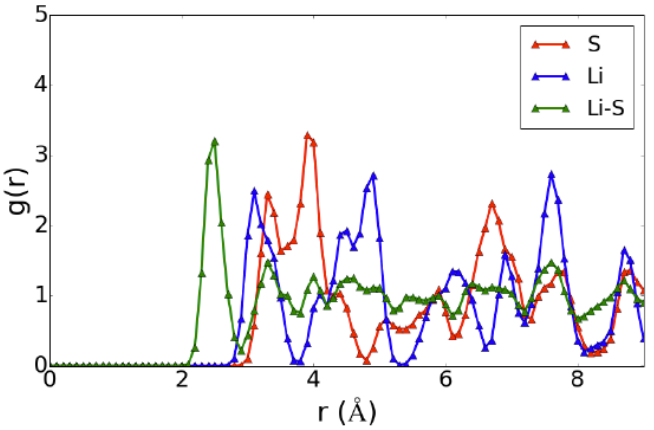

Figure A.10. Static pair distribution function of the initally relaxed Li10GeP2S12

Appendix B Supporting Information for Chapter 4

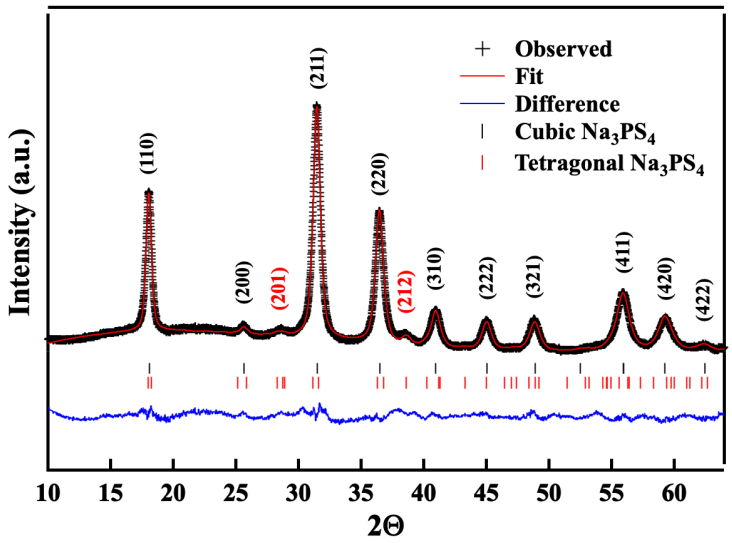

Figure B.1. Rietveld refinement pattern of Na_3PS_4

Table B.1. Rietveld refinement results of ball milled Na_3PS_4

Structural Symmetry	a (nm)	c (nm)	α
Cubic	6.988	-	90
Tetragonal	6.935	7.123	90
Rb = 4.27		Rwp = 3.78	

Cubic Na_3PS_4				
	x	y	z	Uiso
Na1	0.5	0.5	0	0.0546
Na2	0.75	0.5	0	0.0990
P	0	0	0	0.0473
S	0.1699	=x	=x	0.0394
Weight percent ≈ 91%				

Tetragonal Na_3PS_4				
	x	y	z	Uiso
Na1	0	0.5	0.4206	0.0432
Na2	0	0	0	0.0782
P	0	0	0.5	0.0593
S	0.3124	0.34755	0.1650	0.0831
Weight percent ≈ 9%				

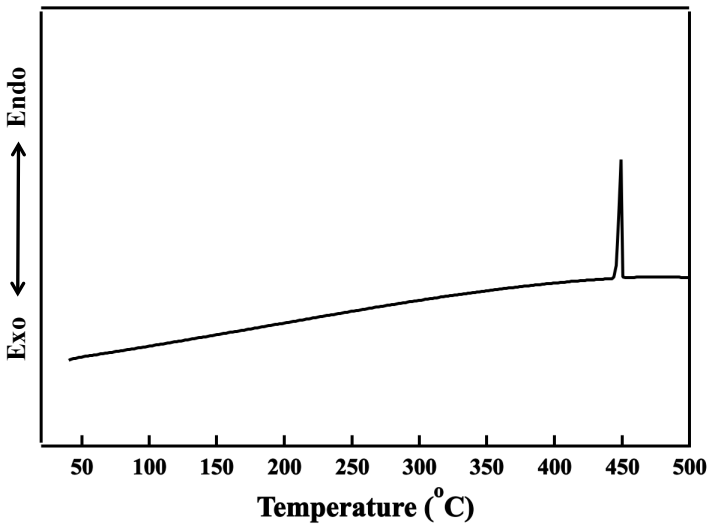

Figure B.2. Differential scanning calorimetry (DSC) results of ball milled Na_3PS_4 upon completing the formation stage. An endothermic process was detected near 450^{0}C and is attributed to remnant tetragonal Na_3PS_4 converting to cubic Na_3PS_4. DSC measurements was conducted with PerkinElmer Pyris Diamond from 30^{o}C to 500^{o}C at a rate of 20^{0}C/min.

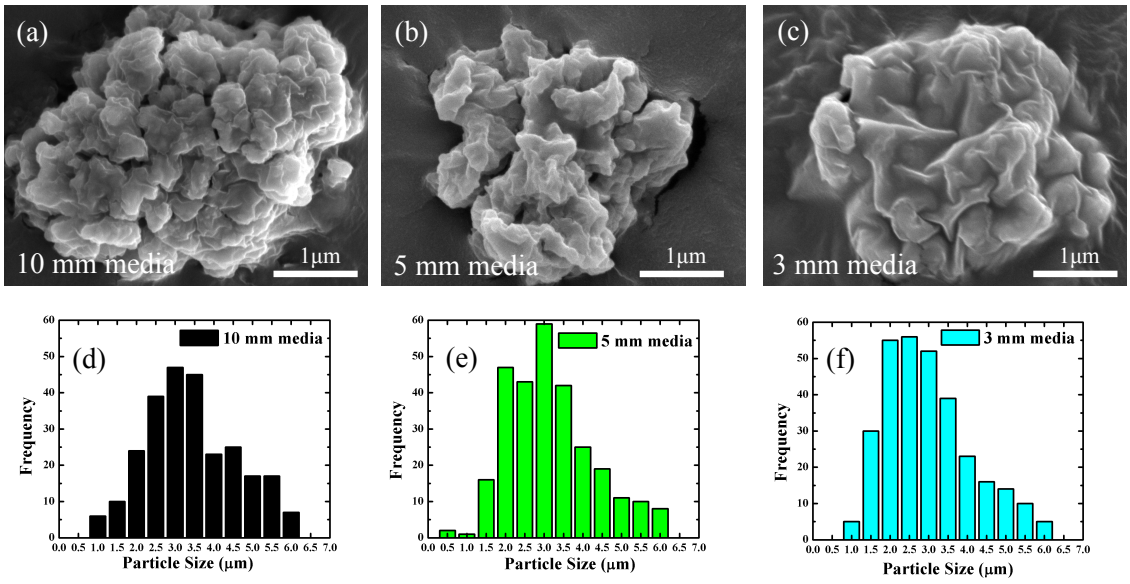

Figure B.3. (a-c) SEM image of Na_3PS_4 particle with varying grinding media size. (d-f) The particle size distribution evaluated from 320 particles for each grinding media size.

Table B.2. Statistical comparison of particle size with varying grinding media size. A sample size of 320 particles has been used for each analysis.

Grinding Media Size	10 mm	5 mm	3 mm
Average (μm)	4.17	3.44	2.90
Standard Deviation (μm)	2.60	2.09	1.40
D10 (μm)	1.83	1.68	1.48
D50 (μm)	3.34	2.90	2.62
D90 (μm)	7.41	6.29	4.72

Appendix C Supporting Information For Chapter 5

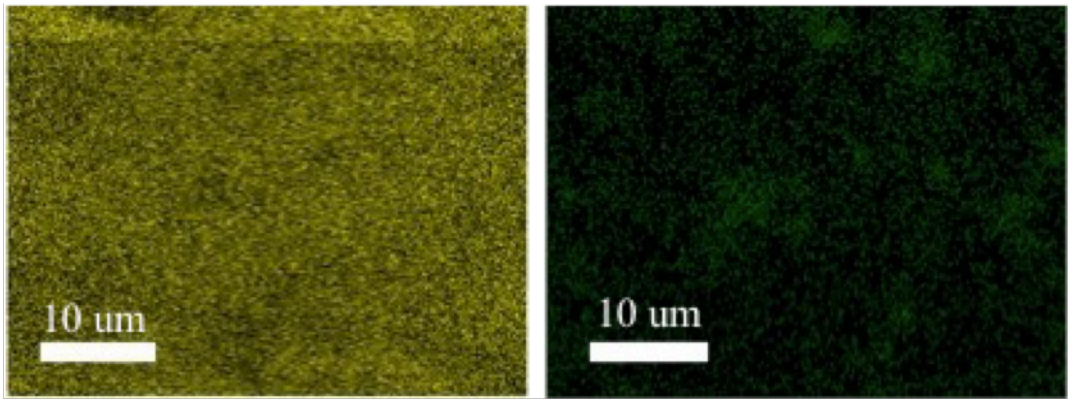

Figure C.1 EDX element maps of doped sample (x = 6.25%) for (a) S and (b) Cl. Maps correspond to SEM image (Figure 4e). Scale bar is 10 mm.

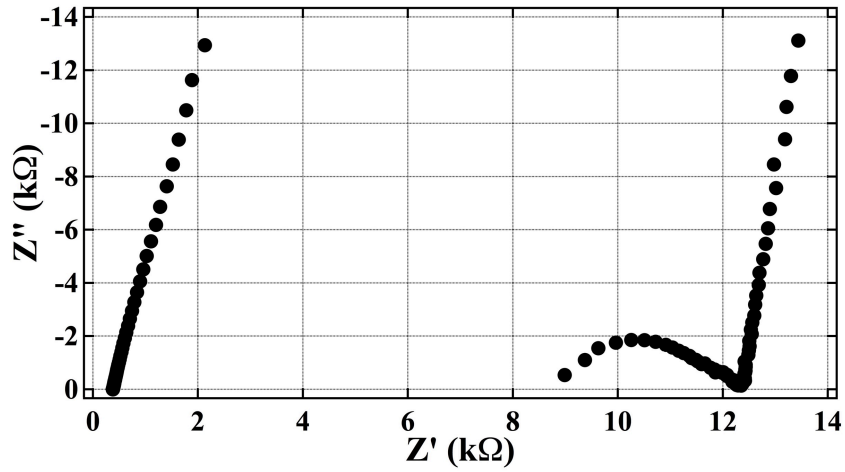

Figure C.2 Room temperature (303 K) Nyquist plots of t-$Na_{3-x}PS_{4-x}Cl_x$. Pristine (x = 0%) performance shown right and doped (x = 6.25%) shown left.

The ionic conductivity of the material was determined via electrochemical impedance spectroscopy (EIS). The total ionic conductivity has contributions from both the bulk and grain boundary, and was measured based on the intersection of the high-frequency capacitive semicircle and the low-frequency tail. The temperature-dependence of the ionic conductivity follows the equation $s=s_0e(-E_a/kT)$, so the slope of the Arrhenius plot can be used to calculate the

Na+ ion migration activation energy. The pristine (x=0%) pellet has the characteristic semicircle and spike typical of ionic conductors. On the other hand, the doped (x=6.25%) pellet does not have a resolvable semicircle though it was measured in the same frequency range as the pristine pellet. This phenomenon has been observed in several other materials, seemingly as the conductivity surpasses 1 mS cm-1. The total room temperature impedances for the pristine and Cl-doped (x = 6.25%) pellets were roughly 12 kΩ and 400 Ω, respectively. By normalizing with the factor (l/A), we account for the thickness (l) and cross-sectional area (A) of the pellet, and the impedance values were then converted to ionic conductivity. The resulting ionic conductivities for the pristine and Cl-doped (x = 6.25%) cases are 0.05 mS cm-1 and 1.14 mS cm-1, respectively. In these EIS measurements, the pristine and Cl-doped (x = 6.25%) pellets were 2.49 mm thick with a diameter of 9.52 mm and 2.40 mm thick with a 9.67 mm diameter, respectively. It is worth pointing out that these dimensions are quite different from the solid-electrolyte layer in the full-cell assembly, which was 1 mm thick with a 12.95 mm diameter. Note also that the measured impedance of the Cl- doped pellet is of the same order of magnitude for the Si-doped Na3PS4 pellet in the previous work by Tanibata et al., in which the resistance of their doped pellet is roughly 350 Ω.[156]

Table C.1. Density measurements of t-Na3-xPS4-xClx. The real density of the as-synthesized powders and the relative density of the spark plasma sintered pellets.

x	Real Density (g mL^{-1})	Relative Density (g mL^{-1})
0	2.268	2.085
0.0625	2.262	1.992

Though cold pressed sulfides, as compared to oxides, have been shown to be reasonably densified, there is still room for improvement. The increase in conductivity is, in part, owing to

the densification of pellets via spark plasma sintering (SPS) which results in a reduction of grain boundary resistance. Grain boundary resistance can be separated into components characteristic of diffusion through the grain and those stemming from a reduced contact area due to porosity. While SPS does not address the intrinsic nature of the grain boundary, it does significantly reduce the porosity of the material, permitting greater contact area between grains. This explains why the ionic conductivity of the pristine t-Na_3PS_4 is an order of magnitude higher than previous reports.[121] Density measurements were conducted to determine the real density of the as-synthesized powders and relative densities of the sintered pellets, and the results are shown in Table C.1. The densities of the two materials are quite similar and we do not observe a significant difference between them. The real densities of powders were measured using a pycnometer purging helium. The real density measurement was carried out in an inert environment. The pristine and doped materials were 2.268 g mL^{-1} and 2.262 g mL^{-1}, respectively. These values are within 2% of the theoretical density and well within experimental error. The relative densities of the pristine and doped pellets were 1.99 g mL^{-1} and 2.08 g mL^{-1}, respectively, which is at least 90% of the theoretical density, 2.22 g mL^{-1}.[121] For this reason, SPS typifies a novel glass-ceramic processing technique which can be effective in both minimizing a material's grain boundary resistance and manufacturing viable all-solid-state batteries by attending to the issue of interfacial contact between the electrode and electrolyte.

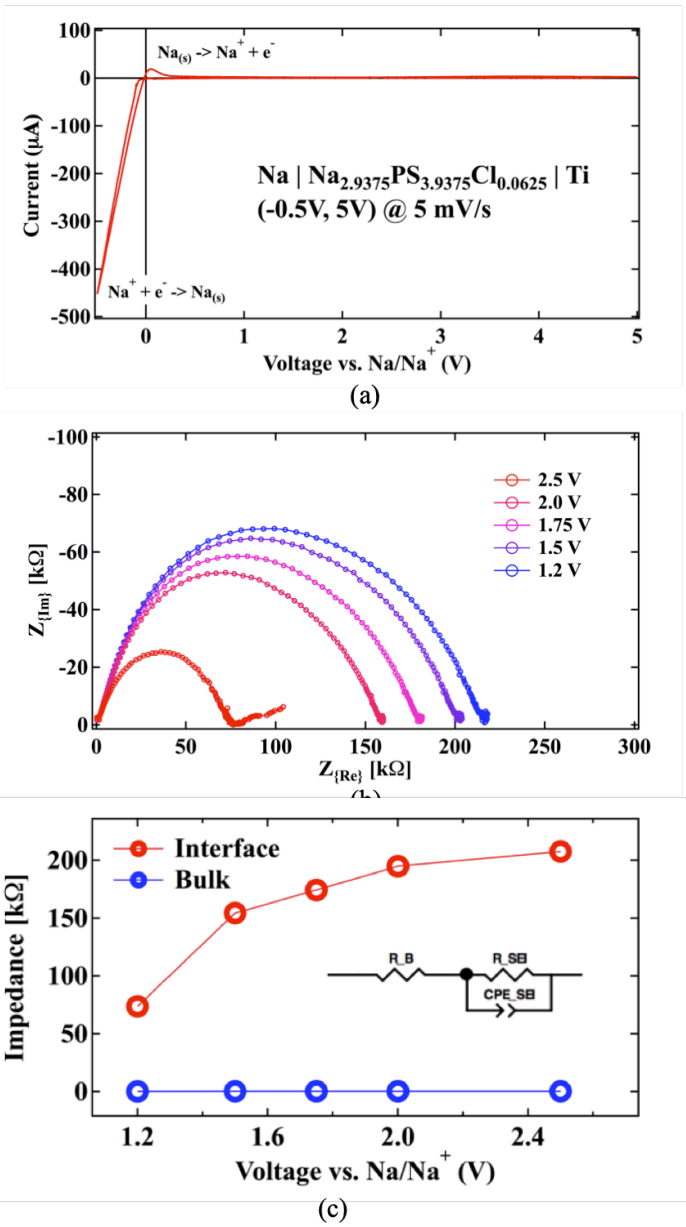

Figure C.3. (a) Cyclic voltammogram of the t-$Na_{3-x}PS_{4-x}Cl_x$ / Na (x=0.0625) interface, swept from -0.5 V to 5 V. Here, a titanium plunger was used as the blocking electrode. The stripping and plating of Na metal is observed at 0 V vs. Na/Na^+, and no other anodic currents are noted up to 5 V. (b) Impedance plots of a discharging TiS_2 / t-$Na_{3-x}PS_{4-x}Cl_x$ / Na full-cell. Measurements were collected at 2.5 V, 2.0 V, 1.75 V, 1.5 V, and 1.2 V. (c) The impedance contributions of bulk and interface are deconvoluted using the results from the provided equivalent circuit

The electrochemical stability of the Cl-doped t-Na3PS4 against Na metal was evaluated. Using a Solartron 1260/1287 analyzer, cyclic voltammetry was performed on a full-cell assembled as described in the Methods section, but using a titanium plunger as a blocking electrode instead of the TiS_2 cathode blende. The voltage was swept from -0.5 V to 5.0 V at 5 mV s^{-1}. The voltammogram shows cathodic and anodic peaks corresponding to the deposition and dissolution of sodium at 0 V vs. Na/Na^+ (see Figure C.3a). No other currents are observed up to 5 V vs. Na/Na^+, suggesting a stable passivation layer at the anode-electrolyte interface.

Impedance measurements of the full-cell were also obtained during the first cycle discharge (see Figure C.3b) using a Solartron 1260/1287. A cell assembled as described in the Methods section was discharged at a C/10 rate, but held at 2.5 V, 2.0 V, 1.75 V, 1.5 V, and 1.2 V while EIS measurements were performed. A 100 mV AC potential was applied and the frequency was swept from 1 MHz to 10 mHz. The cell was fitted using an equivalent circuit proposed by Oh and co- workers.,[184] including contributions from the bulk and interfacial phenomena.

Our results suggest the formation of solid-electrolyte interphase layers as the internal resistance of the cell increases dramatically over the course of the first discharge. We observe that the contributions from the bulk and grain boundary show hardly any deviation from their initial values, while a sharp increase is observed for the interfacial impedance. The capacitances from the interfacial contributions are 2 x 10^{-7} F, which is within the characteristic range of 10^{-7}-10^{-5} F.[18] Our results indicate that the increase in interfacial resistance is indeed attributable to a change in the nature of the interface.

Table C.2. Dopant formation energies Ef and ratio of halide to sulfide ionic radii (RX/RS) of the cubic Na3-xPS4-xXx (X=F, Cl, Br and I) at x = 6.25%.

Dopant	R_X/R_S	x (%)	E_f (eV/dopant)
F	0.70	6.25	0.76
Cl	0.98	6.25	1.14
Br	1.07	6.25	1.27
I	1.21	6.25	1.09

For the TiS_2 charged cathode, we also estimated the average voltage for one electron per transition metal redox reaction. Using Perdew-Burke-Ernzerhof (PBE) generalized-gradient approximation (GGA) functional,[47] the voltage is around 1.58 V, in good agreement with the previous study.[185] On the other hand, we also computed the voltage using the Heyd−Scuseria−Ernzerhof (HSE) hybrid functional,[89,165]from which the calculated voltages are found to agree better with experiment.[186] The calculated HSE voltage for $NaTiS_2$ is 1.7 V, which is about 0.1 V higher than the PBE value.

Appendix D Supporting Information for Chapter 7

Methods

All material synthesis, cell fabrication and testing were performed inside the glove box (MBraun MB 200B, H2O < 0.5 ppm, O2 < 1.0 ppm) due to high air-sensitivity of precursors and solid electrolytes. $LiNi_{0.85}Co_{0.1}Al_{0.05}O_2$ (NCA) was purchased from TODA Chemical.

Material synthesis

Li_6PS_5Cl was synthesized by ball milling the mixture of stoichiometric amount Li_2S (99.9%, Aldrich), P_2S_5 (99.8%, Aldrich) and LiCl (99%, Aldrich). Ball milling was carried out at 600 rpm for 18 hours using a planetary ball mill apparatus (Retsch, PM400) and an air-tight zirconia pot (50 ml) with 11 ZrO_2 balls of 10 mm size. $Li_{0.5}In$ alloy was prepared by mixing stoichiometric amount of lithium powder (FMC) and indium powder (Alfa Asear 99.6%) for 5 mins in the vortex mixer. Solution method was employed to coat $LiNbO_3$ (LNO) on the NCA particle. To be specific, lithium ethoxide (Aldrich 99.8%) and niobium ethoxide (Aldrich 99%) were first dissolved in dry ethanol (Aldrich 99.8%). NCA powder was added into the solution and the solution was stirred for one hour. The dry powder was collected by evaporating the ethanol using rotator vapor and followed by the heat-treatment at 450 °C for one hour to get the LNO coated NCA. The coated powder was dried overnight at 100 °C under vacuum before transferring to the inside of the glove box for storage and fabrication of solid state battery.

LPSCl/activated carbon composite (7:3 wt%) was made by ball mill method at 300 rpm for 30 mins using 5 mm ZrO_2 balls under Ar atmosphere.

Chemical reaction between NCA and LPSCl. Both pristine and charged (bare and LNO-coated) NCA were hand mixed with LPSCl for at least 15 mins (to exaggerate the chemical reaction) using mortar pestle. The ratio of NCA and LPSCl was 11:16 (w/w). The charged

samples were harvested by disassembling the coin cells inside the glove box, which were charged to 4.3 V at C/100. The pellets were made of 200 mg materials under 360 MPa pressure and used as electrode without any conductive additive and binder. The liquid electrolyte is 1 M $LiPF_6$ in ethylene carbonate (EC) /Dimethyl carbonate (DMC) (50:50 v/v). To remove the unreacted LPSCl, the LPSCl-NCA mixture was washed by the dry ethanol solution to dissolve the LPSCl.

Electrochemical characterization:

LPSCl pellet was prepared by cold press with 360 MPa pressure. The conductivity of LPSCl was measured in the Ti/LPSCl/Ti cells. The composite electrode was prepared with 10 mg of NCA, 16 mg of LPSCl and 1mg of carbon as conductive additive. All components were hand grinded with an agate mortar to make a homogeneous mixture. Solid electrolyte was pressed with 360 MPa pressure to make the pellet. 10 mg of the composite cathode was pressed on top of with same pressure. Finally, 70 mg of Li0.5In alloy was pressed with 144 MPa pressure on other side of the pellet. All the procedures were performed in a polyaryletheretherketone (PEEK) mould (diameter = 13 mm) with two Ti metal rods as current collectors. Fabrication of solid state Lithium metal battery was made with 50 micron meter thickness Li metal foil with applied pressure of 20 MPa. Galvanostatic charge discharge measurement was performed at different current densities and 180 mAh/g is equivalent to 1C. All the cells were operated within the potential range between 2.5 and 4.3 V vs. Li/Li^+. R2032 coin cell was used for the NCA/Li cell with liquid electrolyte. Composite slurry was made by mixing NCA powder, super P and poly(vinylidene fluoride) (PVDF) binder using N-Methylpyrrolidone as solvent. The weight ratio of the NCA, super P and PVDF were 85:10:5. The slurry was casted on Al foil and dried at 100 ^0C under vacuum. Li metal was used as counter and reference electrode. 1 M $LiPF_6$ in ethylene carbonate and Dimethyl carbonate (50:50 v/v) was used as electrolyte.

Electrochemical impedance spectroscopy (EIS) was performed using Solartron 1260 impedance analyzer. Conductivity measurement of LPSCl (Ti/LPSCl/Ti) was done with an applied AC potential of 50mV over a frequency range of 1MHz to 1Hz. Impedance measurement of the solid-state cells were performed after charging at 3.675 V (vs. Li0.5In/Li+) and kept with constant voltage of 3.675 vs. reference electrode. The AC perturbation signal was 10 mV, and the frequency range was from 10-2 to 106 Hz in the EIS.

Materials Characterizations

Boron rich capillary tube (Charles Supper) was used to load few milligrams of sample for X-ray diffraction measurement. The sample was loaded inside the glove box and caped with clay before to bring outside where it was flame sealed using a butane torch. Bruker Kappa goniometer equipped with a Bruker Vantec 500 detector was used for measuring the sample. The diffraction data was collected using Cu Kα radiation at 45kV and 50mA.

Raman (Renishaw inVia/Bruker Innova) spectra were measured using illumination of a Modu-Laser 50 mW Ar+ ion laser with wavelength of 514 nm. Samples for Raman measurement were made inside the glove where it was kept on top of glass slides and sealed with Kapton (to avoid the air contamination) tape before to bring it outside.

The XPS samples were prepared inside the glove box and carried outside with a sealed metal canister where it was transferred into the nitrogen filled glove box, attached with XPS chamber. Solid state cells were disassembled after different charge discharge cycle and isolate the cathode composites to prepare the XPS sample. X-ray photoelectron spectroscopy (XPS) was measured with a Kratos Axis Ultra spectrometer with a focused 500mm Rowland circle monochromator Al Kα radiation at 15 KeV. Avantage software was used for data calibration, fitting and analyzing the chemical species at the cathode electrolyte interface. All spectra were calibrated with reference of carbon 1s peak (284.8 eV) and fitted with Shirley type background.

XAS measurements at S K-edge were performed at the Advanced Photon Source on the bending-magnet beamline 9-BM-B with electron energy of 7 GeV and average current of 100 mA. The radiation was monochromatized by a Si (111) double-crystal monochromatic. At the S K-edge, spectra were collected in fluorescence mode using a four-element vortex detector. For energy calibration, a sodium thiosulfate sample was measured. The peak position by Gaussian fitting was adjusted to 2469.2 eV. In situ batteries were operated by a Maccor battery tester with a current density of 0.1 mA/g. Data reduction and analysis were processed by Athena software. (S)TEM: TEM was recorded on a field emission gun JEOL-2800 at 200 kV with Gatan OneView Camera (full 4 K * 4 K resolution). STEM/EDX was performed on primary particles using a JEOL JEM-2800 at annular dark field (ADF) mode. All ADF images and were acquired at 200 kV and with a beam size of ~5 Å. To minimize possible electron beam irradiation effects, ADF images were acquired from areas without pre-beam irradiation.

Computational methods

All density functional theory (DFT) calculations in this work were performed using Vienna ab initio simulation package (VASP)[45] within the projector augmented wave approach[46] using the Perdew−Burke−Ernzerhof generalized-gradient (GGA) functional.[47] All analyses are performed using the Python Materials Genomics (Pymatgen) package.[50]

Structure optimization of NCA and the phase equilibrium at interface DFT parameters (relaxation)

For structure relaxations and total energy calculations, GGA with Hubbard (+U) correction was applied. All calculation parameters, such as the plane wave energy cutoff of 520 eV and k-point density of at least 1000/(number of atom) were selected to keep consistent with the settings of Materials Project (MP)[49]

NCA enumeration

To handle the large number of orderings of the highly-disordered NCA, an enumeration of all symmetrically distinct $Li_9Ni_8CoO_{18}$ or $LiNi_{0.89}Co_{0.11}O_2$ (NCO) structures were performed, in which the initial disordered structure $LiCo_{0.1}Ni_{0.9}O_2$ (ICSD ID: 174452) was obtained from ICSD database. Similarly, the NCO configuration with the lowest energy was used to generate symmetrically distinct NCA orderings by substituting Co or Ni sites to Al atoms and NCA structure with the lowest energy (formula: $Li_{27}Ni_{23}Co_3AlO_{54}$ or $LiNi_{0.85}Co_{0.11}Al_{0.04}O_2$) was further selected to construct phase diagram.

Kinetics of interface: DFT parameters (AIMD):

Non-spin-polarized AIMD calculations were performed using Gamma-point grid and a time step of 2 fs up to 50 ps. A NpT-NVT scheme was applied to minimize the interfacial stress caused by lattice mismatch, which is similar to previous work by the authors7.

Interface construction

Considering the low concentration of Al in NCA, in ab initio molecular dynamics (AIMD) simulations were performed for the approximate interface NCO/LPSCl at half-discharged state. The initial structure of Li_6PS_5Cl (, MP id, mp-985592) was obtained from MP database. The coherent interface model was constructed by matching $Li_{0.5}Ni_{0.89}Co_{0.11}O_2$ and LPSCl with a mean absolute strain of 1.75% using the algorithm proposed by Stradi et al8.

$$\bar{\varepsilon} = \frac{|\varepsilon_{xx}|+|\varepsilon_{xy}|+|\varepsilon_{yy}|}{3} \qquad (1)$$

where, ε_{xx} and ε_{yy} are components of plane strain caused by matching two slabs. The detailed geometry of the atomic structure of the initial interface can be found in Supplementary Information Figure 3 and Table S3.

Geometry analysis:

Changing of the bonds are tracked using radial distribution functions (RDFs) of various species at the interface. Then RDFs of interface throughout the AIMD simulations are compared with known crystalline compounds in Li-Co-Ni-P-S-Cl chemical system extracted from MP database with less than 20 meV/atom. In consider of the limited time scale of AIMD simulation, the P-P and Cl-Cl pairs were not used in matching RDFs due to the low concentration (< 0.05) of P and Cl atoms as well as their commonly long bond lengths (> 3Å). As a result, the RDF spectra matching were performed for the rest 13 pairs, which is similar to previous work by the authors7.

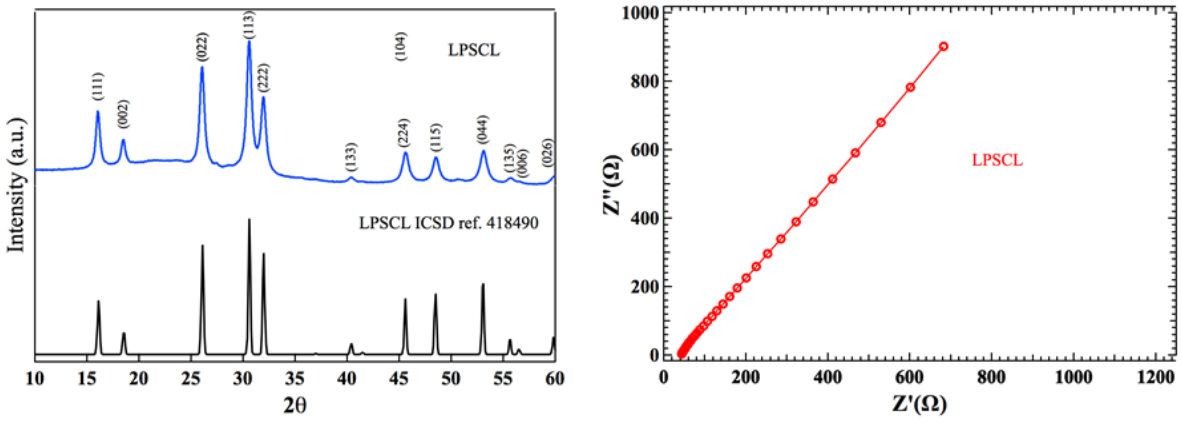

Figure D.1. XRD spectra (a) and Nyquist plot (b) of the LPSCl

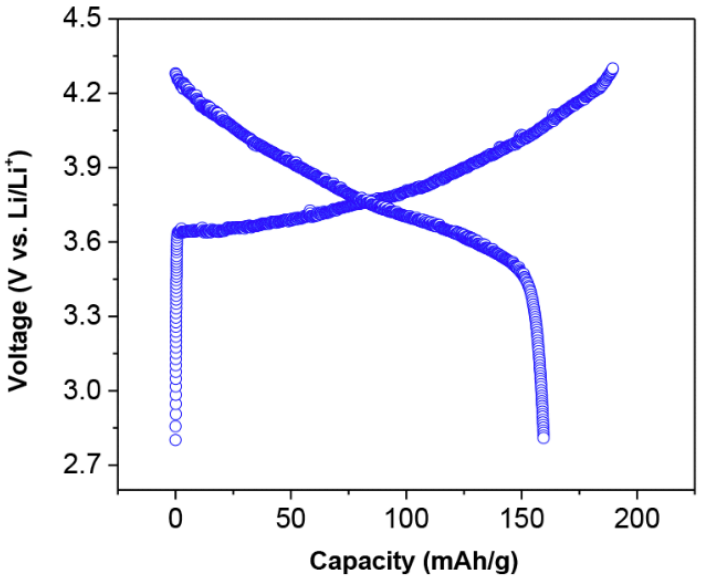

Figure D.2. Electrochemical performance of the LNO-NCA in liquid electrolyte at C/10

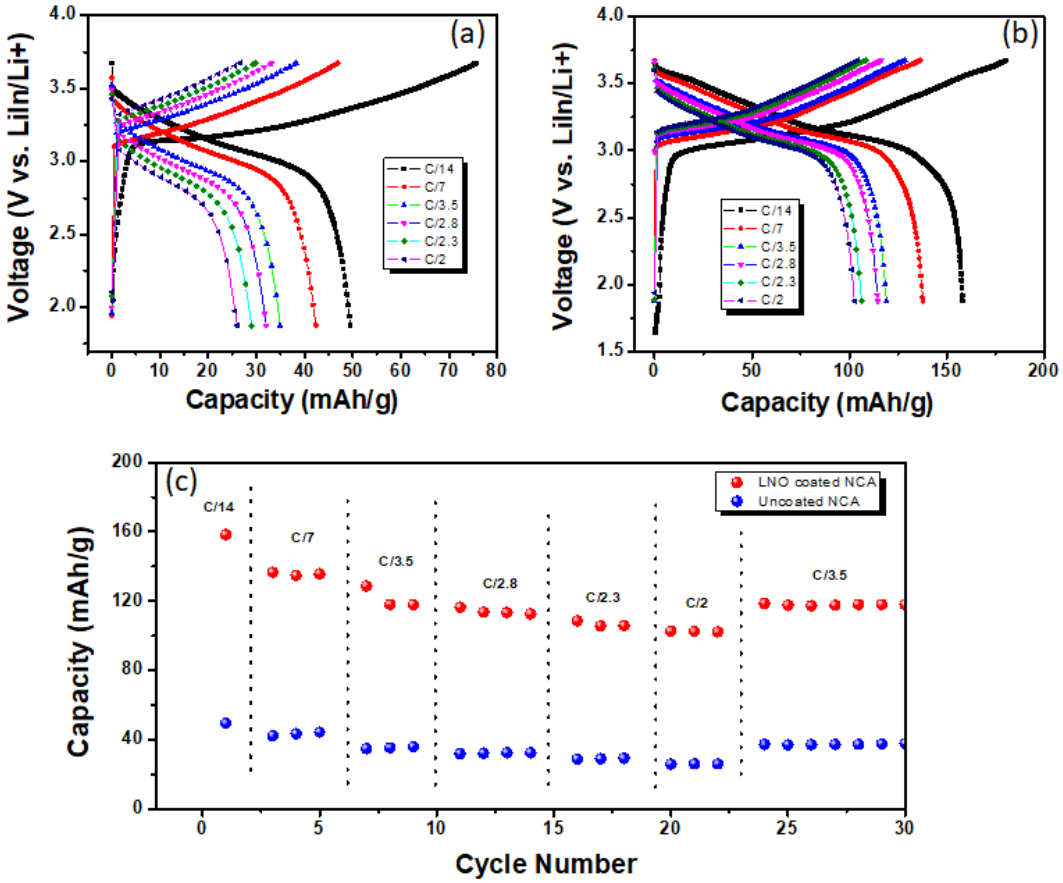

Figure D.3. Potential curve (a, b) and rate capability (c) of the bare and LNO coated NCA at different current densities.

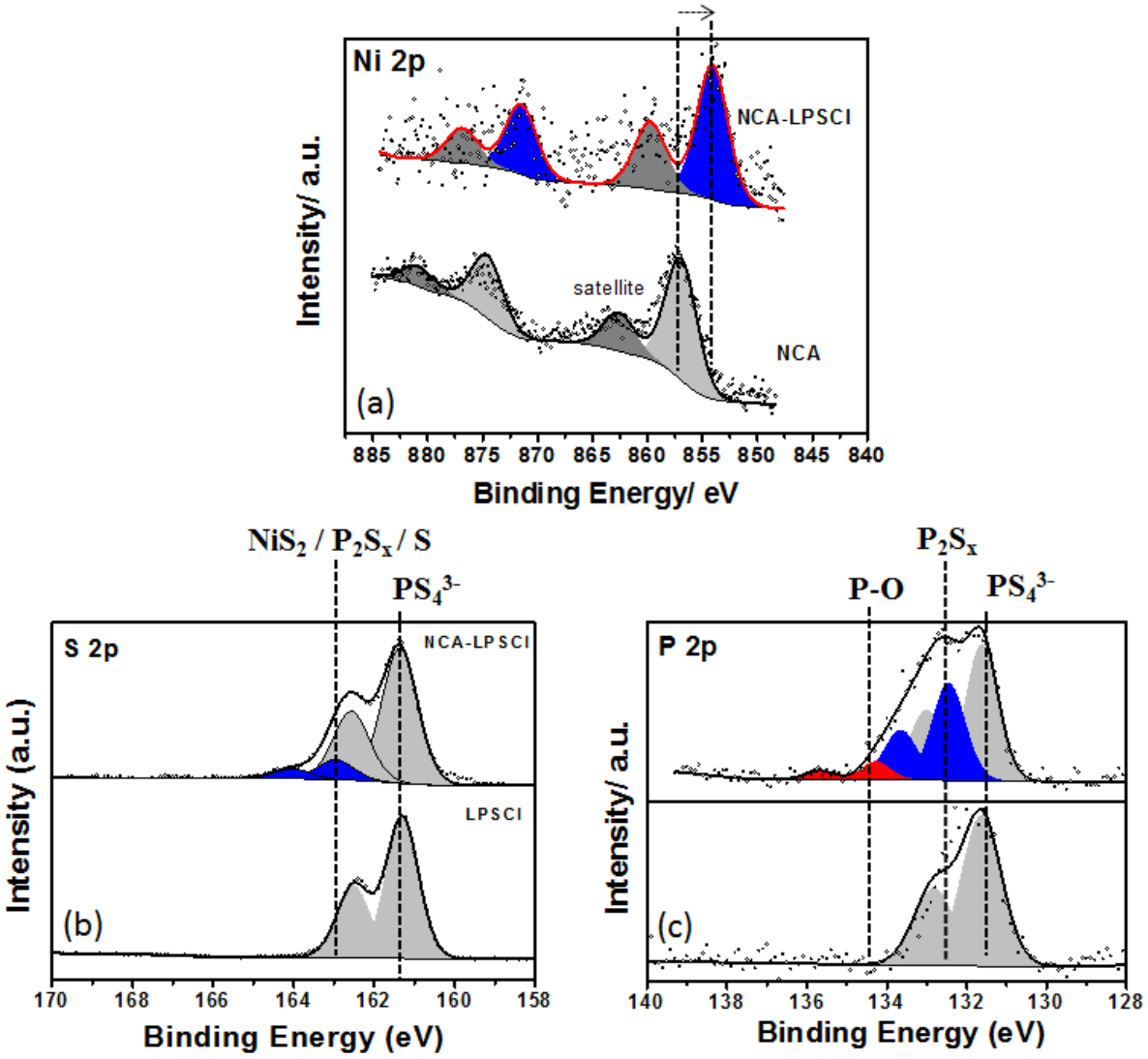

Figure D.4. XPS spectra of the Ni 2p (a), S 2p (a) and P 2p (a) from the mixture of the bare NCA and LPSCl

Table D.1. Phase equilibria at the LPSCl/NCA interface at discharged state as labeled in Figure 7.3a. The major reaction products Li_3PO_4, LiCl, and Ni_3S_4 are highlighted.

Label	Ratio x	Phase equilibria
1	0.0709	0.9291 Li_3PO_4 + 0.2128 $Co(NiS_2)_2$ + 0.4610 NiS_2 + 0.9291 LiCl + 0.0142 $LiAl_5O_8$ + 0.2482 Ni_3S_4 + 1.8794 Li_2S
2	0.0714	0.9286 Li3PO4 + 0.2143 Co(NiS2)2 + 0.4643 NiS2 + 0.9286 LiCl + 0.2500 Ni3S4 + 0.0714 LiAlO2 + 1.8571 Li2S
3	0.0774	0.9226 Li3PO4 + 0.2323 Co(NiS2)2 + 0.0839 Li2SO4 + 0.9226 LiCl + 0.4387 Ni3S4 + 0.0774 LiAlO2 + 1.8452 Li2S
4	0.0907	0.9093 Li3PO4 + 0.2720 Co(NiS2)2 + 0.1713 Ni9S8 + 0.2695 Li2SO4 + 0.9093 LiCl + 0.0907 LiAlO2 + 1.8186 Li2S
5	0.0992	0.9008 Li3PO4 + 0.2975 Co(NiS2)2 + 0.5620 Ni3S2 + 0.3884 Li2SO4 + 0.9008 LiCl + 0.0992 LiAlO2 + 1.8017 Li2S
6	0.1071	0.8929 Li3PO4 + 0.7679 Ni3S2 + 0.5000 Li2SO4 + 0.8929 LiCl + 0.1071 LiAlO2 + 0.1607 Co2NiS4 + 1.7857 Li2S
7	0.1143	0.8857 Li3PO4 + 0.8762 Ni3S2 + 0.0381 Co9S8 + 0.6000 Li2SO4 + 0.8857 LiCl + 0.1143 LiAlO2 + 1.7714 Li2S
8	0.1212	0.8788 Li3PO4 + 0.1212 Li5AlO4 + 0.9293 Ni3S2 + 0.0404 Co9S8 + 0.6364 Li2SO4 + 0.8788 LiCl + 1.5758 Li2S
9	0.1770	0.8230 Li3PO4 + 0.1770 Li5AlO4 + 1.8407 Li2O + 1.3569 Ni3S2 + 0.0590 Co9S8 + 0.9292 Li2SO4 + 0.8230 LiCl
10	0.2985	0.7015 Li3PO4 + 0.2985 Li5AlO4 + 1.2736 Li2O + 0.0995 Co9S8 + 2.7114 Li2SO4 + 0.7015 LiCl + 6.8657 Ni
11	0.3224	0.6776 Li3PO4 + 0.3224 Li5AlO4 + 0.4359 Li6CoO4 + 0.0590 Co9S8 + 2.9160 Li2SO4 + 0.6776 LiCl + 7.4143 Ni
12	0.3457	0.6543 Li3PO4 + 0.3457 Li5AlO4 + 0.3951 Li6CoO4 + 3.2716 Li2SO4 + 0.6543 LiCl + 0.2140 Co3Ni + 7.7366 Ni
13	0.3636	0.6364 Li3PO4 + 0.3636 Li5AlO4 + 0.3636 Li6CoO4 + 3.1818 Li2SO4 + 0.6364 LiCl + 0.7273 LiCoO2 + 8.3636 Ni
14	0.3670	0.4771 Li5CoO4 + 0.6330 Li3PO4 + 0.3670 Li5AlO4 + 3.1651 Li2SO4 + 0.6330 LiCl + 0.6239 LiCoO2 + 8.4404 Ni
15	0.5333	1.6000 Li5CoO4 + 0.4667 Li3PO4 + 0.5333 Li5AlO4 + 9.0667 NiO + 2.3333 Li2SO4 + 0.4667 LiCl + 3.2000 Ni
16	0.6349	1.9048 Li5CoO4 + 0.3651 Li3PO4 + 0.6349 Li5AlO4 + 14.6032 NiO + 0.7619 Li2O + 1.8254 Li2SO4 + 0.3651 LiCl
17	0.6667	1.0000 Li2NiO3 + 2.0000 Li5CoO4 + 0.3333 Li3PO4 + 0.6667 Li5AlO4 + 14.3333 NiO + 1.6667 Li2SO4 + 0.3333 LiCl

Table D.2. Phase equilibria at LPSCl/LNO interface at discharged state as labeled in Figure 7.3b

Label	Ratio	Phase equilibrium
1	0.5000	0.5000 Li3NbS4 + 0.1250 Li3PS4 + 0.5000 LiCl + 0.3750 Li3PO4
2	0.5714	0.0952 NbS2 + 0.4762 Li3NbS4 + 0.4286 LiCl + 0.4286 Li3PO4+ 0.0476 S
3	0.5797	0.1159 NbS2 + 0.4638 Li3NbS4 + 0.0145 Li2SO4 + 0.4203 LiCl + 0.4203 Li3PO4
4	0.5941	0.4007 Li3NbS4 + 0.0138 Li9(NbS2)14 + 0.0397 Li2SO4 + 0.4059 LiCl + 0.4059 Li3PO4

Table D.3. Phase equilibria at LNO/NCA interface at discharged state as labeled in Figure 7.3b

Label	Ratio	Phase equilibrium
1	0.0877	0.5862 Li(NiO2)2 + 0.3103 LiCoNiO4 + 0.8966 NiO + 0.1034 LiAlO2 + 0.8966 Li3NbO4
2	0.1034	0.4561 Ni3O4 + 0.1930 Li(NiO2)2 + 0.2632 LiCoNiO4 + 0.0877 LiAlO2 + 0.9123 Li3NbO4

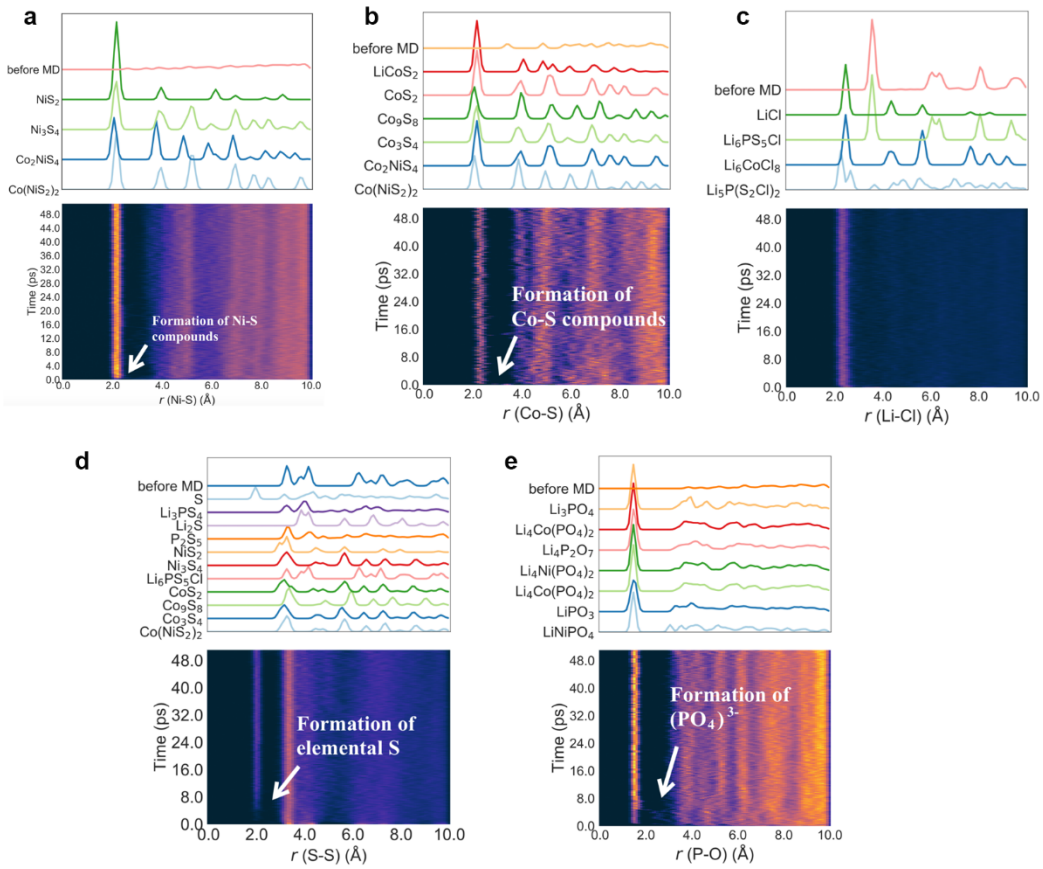

Figure D.5. Variation of P-O pair, Ni-S pair, Co-S pair, Li-Cl pair and S-S pair RDFs of NCA/LPSCl interface at 300K at the half-charged state with respect to AIMD simulation time plotted to 50 ps as a heat map, with a higher brightness indicating a higher value of g(r). The reference materials are provided above the. For comparison purpose, the g(r) of the initial structure labeled as "before MD" is also plotted as a reference structure. Note in (a) and (c) only some references are shown for clarity.

Figure D.6. Setup for purging oxygen to oxidize LPSCl to form oLPSCl

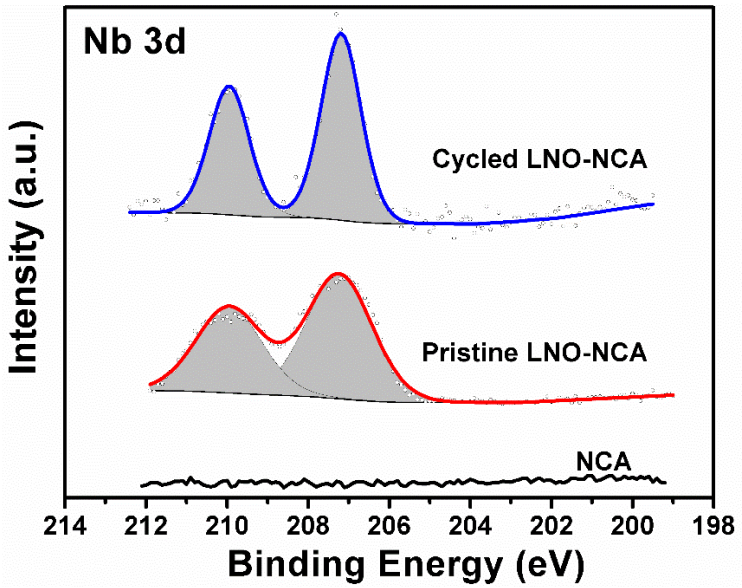

Figure D.7. XPS spectra of Nb for bare NCA, LNO-NCA and the cycled LNO-NCA

Table D.4. Energy density estimation of ASSBs

Component	value	unit
NCA Loading	10	mg/cm^2
NCA reversible Capacity	160	mAh/g
LPSCl film thickness	50	μm
Li metal thickness	50	μm
Cell energy density	425	Wh/kg

Reference

1. Goodenough, J. B. & Kim, Y. Challenges for rechargeable Li batteries. *Chem. Mater.* **22,** 587–603 (2009).

2. Geddes, L. A. & Hoff, H. E. The discovery of bioelectricity and current electricity. The Galvani-Volta controversy. *IEEE Spectr.* **8,** 38–46 (1971).

3. Ozawa, K. Lithium-ion rechargeable batteries with LiCoO2 and carbon electrodes: the LiCoO2/C system. *Solid State Ionics* (1994). doi:10.1016/0167-2738(94)90411-1

4. Chen, C. H., Liu, J., Stoll, M. E., Henriksen, G., Vissers, D. R. & Amine, K. Aluminum-doped lithium nickel cobalt oxide electrodes for high-power lithium-ion batteries. *J. Power Sources* **128,** 278–285 (2004).

5. Jung, S. K., Gwon, H., Hong, J., Park, K. Y., Seo, D. H., Kim, H., Hyun, J., Yang, W. & Kang, K. Understanding the degradation mechanisms of LiNi0.5Co0.2Mn0.3O2cathode material in lithium ion batteries. *Adv. Energy Mater.* **4,** 1–7 (2014).

6. Xu, K. Electrolytes and interphases in Li-ion batteries and beyond. *Chem. Rev.* **114,** 11503–11618 (2014).

7. Rapier, R. The Holy Grail Of Lithium Batteries. (2019). at <https://www.forbes.com/sites/rrapier/2019/05/16/the-holy-grail-of-lithium-batteries/#6004f4f93d63>

8. Xu, K. Nonaqueous liquid electrolytes for lithium-based rechargeable batteries. *Chem. Rev.* **104,** 4303–4418 (2004).

9. Aurbach, D., Zinigrad, E., Cohen, Y. & Teller, H. A short review of failure mechanisms of lithium metal and lithiated graphite anodes in liquid electrolyte solutions. in *Solid State Ionics* (2002). doi:10.1016/S0167-2738(02)00080-2

10. Thangadurai, V., Pinzaru, D., Narayanan, S. & Baral, A. K. Fast solid-state Li ion conducting garnet-type structure metal oxides for energy storage. *J. Phys. Chem. Lett.* **6,** 292–299 (2015).

11. Goodenough, J. B., Hong, H.-P. & Kafalas, J. A. Fast Na+-ion transport in skeleton structures. *Mater. Res. Bull.* **11,** 203–220 (1976).

12. Nimisha, C. S., Rao, K. Y., Venkatesh, G., Rao, G. M. & Munichandraiah, N. Sputter deposited LiPON thin films from powder target as electrolyte for thin film battery applications. *Thin Solid Films* **519,** 3401–3406 (2011).

13. Hueso, K. B., Armand, M. & Rojo, T. High temperature sodium batteries: status, challenges and future trends. *Energy Environ. Sci.* **6,** 734 (2013).

14. Kamaya, N., Homma, K., Yamakawa, Y., Hirayama, M., Kanno, R., Yonemura, M., Kamiyama, T., Kato, Y., Hama, S., Kawamoto, K. & Mitsui, A. A lithium superionic conductor. *Nat. Mater.* **10,** 682–686 (2011).

15. RAMAN, C. V & KRISHNAN, K. S. A New Type of Secondary Radiation. *Nature* **121,** 501–502 (1928).

16. Larkin, P. J. *IR and Raman Spectroscopy - Principles and Spectral Interpretation*. (2011).

17. Södergren, S., Siegbahn, H., Rensmo, H., Lindström, H., Hagfeldt, A. & Lindquist, S.-E. Lithium Intercalation in Nanoporous Anatase TiO 2 Studied with XPS . *J. Phys. Chem. B* **101,** 3087–3090 (2002).

18. Irvine, J. T. S., Sinclair, D. C. & West, A. R. Electroceramics: characterization by impedance spectroscopy. *Adv. Mater.* **2,** 132–138 (1990).

19. Xu, K. Nonaqueous liquid electrolytes for lithium-based rechargeable batteries. *Chem. Rev.* **104,** 4303–4417 (2004).

20. Goodenough, J. B. & Kim, Y. Challenges for rechargeable Li batteries. *Chem. Mater.* **22,** 587–603 (2010).

21. Dudney, N. J. Solid-state thin-film rechargeable batteries. *Mater. Sci. Eng. B Solid-State Mater. Adv. Technol.* **116,** 245–249 (2005).

22. Baggetto, L., Niessen, R. a H., Roozehoom, F. & Notten, P. H. L. High energy density all-solid-state batteries: A challenging concept towards 3D integration. *Adv. Funct. Mater.* **18,** 1057–1066 (2008).

23. Thangadurai, V., Pinzaru, D., Narayanan, S. & Baral, A. K. Fast Solid-State Li Ion Conducting Garnet-Type Structure Metal Oxides for Energy Storage. *J. Phys. Chem. Lett.* 6–13 (2015). doi:10.1021/jz501828v

24. Hayashi, A., Ohtomo, T., Mizuno, F., Tadanaga, K. & Tatsumisago, M. All-solid-state Li/S batteries with highly conductive glass-ceramic electrolytes. *Electrochem. commun.* **5,** 701–705 (2003).

25. Thompson, T., Wolfenstine, J., Allen, J. L., Johannes, M., Huq, A., David, I. N. & Sakamoto, J. Tetragonal vs. cubic phase stability in Al - free Ta doped Li7La3Zr2O12 (LLZO). *J. Mater. Chem. A* **2,** 13431–13436 (2014).

26. Zhu, Z., Chu, I. H., Deng, Z. & Ong, S. P. Role of Na+ Interstitials and Dopants in Enhancing the Na+ Conductivity of the Cubic Na3PS4 Superionic Conductor. *Chem. Mater.* **27,** 8318–8325 (2015).

27. Zhao, Y. & Daemen, L. L. Superionic conductivity in lithium-rich anti-perovskites. *J. Am. Chem. Soc.* **134,** 15042–15047 (2012).

28. Braga, M. H., Ferreira, J. a., Stockhausen, V., Oliveira, J. E. & El-Azab, a. Novel Li3ClO based glasses with superionic properties for lithium batteries. *J. Mater. Chem. A* **2,** 5470 (2014).

29. Lü, X., Wu, G., Howard, J. W., Chen, A., Zhao, Y., Daemen, L. L. & Jia, Q. Li-rich anti-perovskite Li<inf>3</inf>OCl films with enhanced ionic conductivity. *Chem. Commun.* **50,** 11520–11522 (2014).

30. Zhang, J., Han, J., Zhu, J., Lin, Z., Braga, M. H., Daemen, L. L., Wang, L. & Zhao, Y. High pressure-high temperature synthesis of lithium-rich Li3O(Cl, Br) and Li3−xCax/2OCl anti-perovskite halides. *Inorg. Chem. Commun.* **48,** 140–143 (2014).

31. Deng, Z., Radhakrishnan, B. & Ong, S. P. Rational Composition Optimization of the Lithium-rich Li3OCl1–xBrx Anti-perovskite Superionic Conductors. *Chem. Mater.* **27,** 3749 (2015).

32. Mouta, R., Melo, M. A. B., Diniz, E. M. & Paschoal, C. W. A. Concentration of charge carriers, migration, and stability in Li3OCl solid electrolytes. *Chem. Mater.* **26,** 7137–7144 (2014).

33. Emly, A., Kioupakis, E. & der Ven, A. Phase stability and transport mechanisms in antiperovskite Li3OCl and Li3OBr superionic conductors. *Chem. Mater.* **25,** 4663–4670 (2013).

34. Ellis, B. L. & Nazar, L. F. Sodium and sodium-ion energy storage batteries. *Curr. Opin. Solid State Mater. Sci.* **16,** 168–177 (2012).

35. Wang, Y., Wang, Q., Liu, Z., Zhou, Z., Li, S., Zhu, J., Zou, R., Wang, Y., Lin, J. & Zhao, Y. Structural manipulation approaches towards enhanced sodium ionic conductivity in Na-rich antiperovskites. *J. Power Sources* **293,** 735–740 (2015).

36. Moseley, P. & Garche, J. *Electrochemical Energy Storage for Renewable Sources and Grid Balancing*. *Electrochem. Energy Storage Renew. Sources Grid Balanc.* (2014). doi:10.1016/B978-0-444-62616-5.00017-6

37. Munir, Z. A., Anselmi-Tamburini, U. & Ohyanagi, M. The effect of electric field and pressure on the synthesis and consolidation of materials: A review of the spark plasma sintering method. *J. Mater. Sci.* **41,** 763–777 (2006).

38. Mei, A., Jiang, Q.-H., Lin, Y.-H. & Nan, C.-W. Lithium lanthanum titanium oxide solid-state electrolyte by spark plasma sintering. *J. Alloys Compd.* **486,** 871–875 (2009).

39. Langer, J., Hoffmann, M. J. & Guillon, O. Direct comparison between hot pressing and electric field-assisted sintering of submicron alumina. *Acta Mater.* **57,** 5454–5465 (2009).

40. Delaizir, G., Manafi, N., Jouan, G., Rozier, P. & Dollé, M. All-solid-state silver batteries assembled by Spark Plasma Sintering. *Solid State Ionics* **207,** 57–63 (2012).

41. Kobayashi, Y., Takeuchi, T., Tabuchi, M., Ado, K. & Kageyama, H. Densification of LiTi2(PO4)3-based solid electrolytes by spark-plasma-sintering. *J. Power Sources* **81–82,** 853–858 (1999).

42. Lee, J.-S., Chang, C.-M., Lee, Y. I. L., Lee, J.-H. & Hong, S.-H. Spark plasma sintering (SPS) of NASICON ceramics. *J. Am. Ceram. Soc.* **87,** 305–307 (2004).

43. Papadopulos, F., Spinelli, M., Valente, S., Foroni, L., Orrico, C., Alviano, F. & Pasquinelli, G. Common tasks in microscopic and ultrastructural image analysis using ImageJ. *Ultrastruct. Pathol.* **31,** 401–407 (2007).

44. Idris, M. S. & Osman, R. A. M. Structure refinement strategy of Li-based complex oxides using GSAS-EXPGUI software package. in *Adv. Mater. Res.* **795,** 479–482 (2013).

45. Kresse, G. & Furthmüller, J. Efficient Iterative Schemes for Ab Initio Total-energy Calculations Using a Plane-wave Basis Set. *Phys. Rev. B Condens. Matter Mater. Phys.* **54,** 11169 (1996).

46. Blöchl, P. E. Projector Augmented-wave Method. *Phys. Rev. B Condens. Matter Mater. Phys.* **50,** 17953 (1994).

47. Perdew, J., Burke, K. & Ernzerhof, M. Generalized Gradient Approximation Made Simple. *Phys. Rev. Lett.* **77,** 3865 (1996).

48. Jain, A., Ong, S. P., Hautier, G., Chen, W., Richards, W. D., Dacek, S., Cholia, S., Gunter, D., Skinner, D., Ceder, G. & Persson, K. a. Commentary: The Materials Project: A Materials Genome Approach to Accelerating Materials Innovation. *APL Mater.* **1,** 11002 (2013).

49. Ong, S. P., Cholia, S., Jain, A., Brafman, M., Gunter, D., Ceder, G. & Persson, K. a. The Materials Application Programming Interface (API): A Simple, Flexible and Efficient API for Materials Data Based on REpresentational State Transfer (REST) Principles. *Comput. Mater. Sci.* **97,** 209 (2015).

50. Ong, S. P., Richards, W. D., Jain, A., Hautier, G., Kocher, M., Cholia, S., Gunter, D., Chevrier, V. L., Persson, K. a. & Ceder, G. Python Materials Genomics (Pymatgen): A Robust, Open-Source Python Library for Materials Analysis. *Comput. Mater. Sci.* **68,** 314 (2013).

51. Hippler, K., Sitta, S., Vogt, P. & Sabrowsky, H. Structure of Na3OCl. *Acta Crystallogr. Sect. C Cryst. Struct. Commun.* **46,** 736–738 (1990).

52. Chu, I.-H., Nguyen, H., Hy, S., Lin, Y.-C., Wang, Z., Xu, Z., Deng, Z., Meng, Y. S. & Ong, S. P. Insights into the Performance Limits of the Li7P3S11 Superionic Conductor: A Combined First-Principles and Experimental Study. *ACS Appl. Mater. Interfaces* (2016). doi:10.1021/acsami.6b00833

53. Huggins, R. A. Simple method to determine electronic and ionic components of the

conductivity in mixed conductors a review. *Ionics (Kiel).* **8,** 300–313 (2002).

54. Li, S., Zhu, J., Wang, Y., Howard, J. W., Lü, X., Li, Y., Kumar, R. S., Wang, L., Daemen, L. L. & Zhao, Y. Reaction mechanism studies towards effective fabrication of lithium-rich anti-perovskites Li3OX (X= Cl, Br). *Solid State Ionics* **284,** 14–19 (2016).

55. Luo, J. Interfacial engineering of solid electrolytes. *J. Mater.* **1,** 22–32 (2015).

56. Lu, Z., Chen, C., Baiyee, Z. M., Chen, X., Niu, C. & Ciucci, F. Defect chemistry and lithium transport in Li 3 OCl anti-perovskite superionic conductors. *Phys. Chem. Chem. Phys.* **17,** 32547–32555 (2015).

57. Schroeder, D. J., Hubaud, A. A. & Vaughey, J. T. Stability of the solid electrolyte Li3OBr to common battery solvents. *Mater. Res. Bull.* **49,** 614–617 (2014).

58. Li, J., Ma, C., Chi, M., Liang, C. & Dudney, N. J. Solid Electrolyte: the Key for High-Voltage Lithium Batteries. *Adv. Energy Mater.* **5,** n/a-n/a (2015).

59. Shen, Z., Johnsson, M., Zhao, Z. & Nygren, M. Spark plasma sintering of alumina. *J. Am. Ceram. Soc.* **85,** 1921–1927 (2002).

60. Zhang, Y., Zhao, Y. & Chen, C. Ab initio study of the stabilities of and mechanism of superionic transport in lithium-rich antiperovskites. *Phys. Rev. B* **87,** 134303 (2013).

61. Qian, D., Xu, B., Cho, H.-M., Hatsukade, T., Carroll, K. J. & Meng, Y. S. Lithium lanthanum titanium oxides: a fast ionic conductive coating for lithium-ion battery cathodes. *Chem. Mater.* **24,** 2744–2751 (2012).

62. Inaguma, Y., Liquan, C., Itoh, M., Nakamura, T., Uchida, T., Ikuta, H. & Wakihara, M. High Ionic Conductivity in Lithium Lanthanum Titanate. *Solid State Commun.* **86,** 689 (1993).

63. Murugan, R., Thangadurai, V. & Weppner, W. Fast Lithium Ion Conduction in Garnet-type Li7La3Zr2O12. *Angew. Chem., Int. Ed.* **46,** 7778 (2007).

64. Kamaya, N., Homma, K., Yamakawa, Y., Hirayama, M., Kanno, R., Yonemura, M., Kamiyama, T., Kato, Y., Hama, S., Kawamoto, K. & Mitsui, A. A Lithium Superionic Conductor. *Nat. Mater.* **10,** 682 (2011).

65. Yamane, H., Shibata, M., Shimane, Y., Junke, T., Seino, Y., Adams, S., Minami, K., Hayashi, A. & Tatsumisago, M. Crystal Structure of a Superionic Conductor, Li7P3S11. *Solid State Ionics* **178,** 1163 (2007).

66. Seino, Y., Ota, T., Takada, K., Hayashi, A. & Tatsumisago, M. A Sulphide Lithium Super Ion Conductor Is Superior to Liquid Ion Conductors for Use in Rechargeable Batteries. *Energy Environ. Sci.* **7,** 627 (2014).

67. Tarascon, J. & Armand, M. Issues and Challenges Facing Rechargeable Lithium Batteries.

Nature **414,** 359 (2001).

68. Armand, M. & Tarascon, J. Building Better Batteries. *Nature* **451,** 652 (2008).

69. Xu, K. Electrolytes and Interphases in Li-ion Batteries and Beyond. *Chem. Rev.* **114,** 11503 (2014).

70. Mo, Y., Ong, S. P. & Ceder, G. First Principles Study of the Li10GeP2S12 Lithium Super Ionic Conductor Material. *Chem. Mater.* **24,** 15 (2012).

71. Mizuno, F., Hayashi, a., Tadanaga, K. & Tatsumisago, M. New, Highly Ion-conductive Crystals Precipitated from Li2S-P2S5 Glasses. *Adv. Mater.* **17,** 918 (2005).

72. Mizuno, F., Hayashi, a., Tadanaga, K. & Tatsumisago, M. High Lithium Ion Conducting Glass-Ceramics in the System Li2S-P2S5. *Solid State Ionics* **177,** 2721 (2006).

73. Minami, K., Hayashi, A. & Tatsumisago, M. Preparation and Characterization of Superionic Conducting Li7P3S11 Crystal from Glassy Liquids. *J. Ceram. Soc. Jpn.* **118,** 305 (2010).

74. Minami, K., Hayashi, A. & Tatsumisago, M. Crystallization Process for Superionic Li7P3S11 Glass-ceramic Electrolytes. *J. Am. Ceram. Soc.* **94,** 1779 (2011).

75. Ong, S. P., Mo, Y., Richards, W. D., Miara, L., Lee, H. S. & Ceder, G. Phase Stability, Electrochemical Stability and Ionic Conductivity of the Li10±1MP2X12 (M = Ge, Si, Sn, Al or P, and X = O, S or Se) Family of Superionic Conductors. *Energy Environ. Sci.* **6,** 148 (2013).

76. Bron, P., Johansson, S., Zick, K., Schmedt auf der Gunne, J., Dehnen, S. S. & Roling, B. Li10SnP2S12 - An Affordable Lithium Superionic Conductor Li10SnP2S12 - An Affordable Lithium Superionic Conductor. *J. Am. Chem. Soc.* **135,** 15694 (2013).

77. Kuhn, A., Duppel, V. & Lotsch, B. V. Tetragonal Li10GeP2S12 and Li7GePS8 - Exploring the Li Ion Dynamics in LGPS Li Electrolytes. *Energy Environ. Sci.* **6,** 3548 (2013).

78. Onodera, Y., Mori, K., Otomo, T., Sugiyama, M. & Fukunaga, T. Structural Evidence for High Ionic Conductivity of Li7P3S11 Metastable Crystal. *J. Phys. Soc. Jpn.* **81,** 44802 (2012).

79. Onodera, Y., Mori, K., Otomo, T., Arai, H., Uchimoto, Y., Ogumi, Z. & Fukunaga, T. Structural Origin of Ionic Conductivity for Li7P3S11 Metastable Crystal by Neutron And X-ray Diffraction. *J. Phys. Conf. Ser.* **502,** 12021 (2014).

80. Lepley, N. D. & Holzwarth, N. a. W. Computer Modeling of Crystalline Electrolytes: Lithium Thiophosphates and Phosphates. *J. Electrochem. Soc.* **159,** A538 (2012).

81. Monkhorst, H. & Pack, J. Special Points for Brillouin-zone Integrations. *Phys. Rev. B* **13,**

5188 (1976).

82. Ong, S. P., Wang, L., Kang, B. & Ceder, G. Li-Fe-P-O2 Phase Diagram from First Principles Calculations. *Chem. Mater.* **20,** 1798 (2008).

83. Wang, L., Maxisch, T. & Ceder, G. Oxidation Energies of Transition Metal Oxides within the GGA + U Framework. *Phys. Rev. B Condens. Matter Mater. Phys.* **73,** 195107 (2006).

84. Zhu, Z., Chu, I.-H., Deng, Z. & Ong, S. P. Role of Na+ Interstitials and Dopants in Enhancing the Na+ Conductivity of the Cubic Na3PS4 Superionic Conductor. *Chem. Mater.* **27,** 8318 (2015).

85. Togo, A., Oba, F. & Tanaka, I. First-Principles Calculations of the Ferroelastic Transition between Rutile-type and CaCl2-type SiO2 at High Pressures. *Phys. Rev. B Condens. Matter Mater. Phys.* **78,** 134106 (2008).

86. Baroni, S., de Gironcoli, S. D., Dal Corso, A. & Giannozzi, P. Phonons and Related Crystal Properties from Density-Functional Perturbation Theory. *Rev. Mod. Phys.* **73,** 515 (2001).

87. Miara, L. J., Richards, W. D., Wang, Y. E. & Ceder, G. First-principles Studies on Cation Dopants and Electrolyte-cathode Interphases for Lithium Garnets. *Chem. Mater.* **27,** 4040 (2015).

88. Ong, S. P. & Ceder, G. Investigation of the Effect of Functional Group Substitutions on the Gas-phase Electron Affinities and Ionization Energies of Room-temperature Ionic Liquids Ions Using Density Functional Theory. *Electrochim. Acta* **55,** 3804 (2010).

89. Heyd, J., Scuseria, G. E. & Ernzerhof, M. Hybrid Functionals Based on a Screened Coulomb Potential. *J. Chem. Phys.* **118,** 8207 (2003).

90. Heyd, J., Scuseria, G. E. & Ernzerhof, M. Erratum: ”Hybrid Functionals Based on a Screened Coulomb Potential” [J. Chem. Phys. 118, 8207 (2003)]. *J. Chem. Phys.* **124,** 219906 (2006).

91. Heyd, J. & Scuseria, G. E. Efficient Hybrid Density Functional Calculations in Solids: Assessment of the Heyd-Scuseria-Ernzerhof Screened Coulomb Hybrid Functional. *J. Chem. Phys.* **121,** 1187 (2004).

92. Wang, L., Zhou, F., Meng, Y. S. & Ceder, G. First-Principles Study of Surface Properties of LiFePO4: Surface Energy, Structure, Wulff Shape, and Surface Redox Potential. *Phys. Rev. B Condens. Matter Mater. Phys.* **76,** 165435 (2007).

93. Sakuda, A., Hayashi, A. & Tatsumisago, M. Interfacial Observation Between LiCoO2 Electrode and Li2S-P2S5 Solid Electrolytes of All-solid-state Lithium Secondary Batteries Using Transmission Electron Microscopy. *Chem. Mater.* **22,** 949 (2010).

94. Ramos, M., Berhault, G., Ferrer, D. a., Torres, B. & Chianelli, R. R. HRTEM and

Molecular Modeling of the MoS2-Co9S8 Interface: Understanding the Promotion Effect in Bulk HDS Catalysts. *Catal. Sci. Technol.* **2,** 164 (2012).

95. Qiao, L., Xiao, H. Y., Meyer, H. M., Sun, J. N., Rouleau, C. M., Puretzky, a. a., Geohegan, D. B., Ivanov, I. N., Yoon, M., Weber, W. J. & Biegalski, M. D. Nature of the Band Gap and Origin of the Electro-/Photo-activity of Co3O4. *J. Mater. Chem. C* **1,** 4628 (2013).

96. Xiong, K., Longo, R., Kc, S., Wang, W. & Cho, K. Behavior of Li Defects in Solid Electrolyte Lithium Thiophosphate Li7P3S11: A First Principles Study. *Comput. Mater. Sci.* **90,** 44 (2014).

97. Hayamizu, K. & Aihara, Y. Lithium Ion Diffusion in Solid Electrolyte (Li2S)7(P2S5)3 Measured by Pulsed-gradient Spin-echo 7Li NMR Spectroscopy. *Solid State Ionics* **238,** 7 (2013).

98. Perdew, J., Ruzsinszky, A., Csonka, G., Vydrov, O., Scuseria, G., Constantin, L., Zhou, X. & Burke, K. Restoring the Density-gradient Expansion for Exchange in Solids and Surfaces. *Phys. Rev. Lett.* **100,** 136406 (2008).

99. Mori, K., Enjuji, K., Murata, S., Shibata, K., Kawakita, Y., Yonemura, M., Onodera, Y. & Fukunaga, T. Direct Observation of Fast Lithium-Ion Diffusion in a Superionic Conductor: Li7P3S11 Metastable Crystal. *Phys. Rev. Appl.* **4,** 54008 (2015).

100. Zhu, Y., He, X. & Mo, Y. Origin of Outstanding Stability in the Lithium Solid Electrolyte Materials: Insights from Thermodynamic Analyses Based on First Principles Calculations. *ACS Appl. Mater. Interfaces* **7,** 23685 (2015).

101. Takada, K., Ohta, N., Zhang, L., Fukuda, K., Sakaguchi, I., Ma, R., Osada, M. & Sasaki, T. Interfacial Modification for High-power Solid-state Lithium Batteries. *Solid State Ionics* **179,** 1333 (2008).

102. Takada, K., Ohta, N., Zhang, L., Xu, X., Hang, B. T., Ohnishi, T., Osada, M. & Sasaki, T. Interfacial Phenomena in Solid-state Lithium Battery with Sulfide Solid Electrolyte. *Solid State Ionics* **225,** 594 (2012).

103. Seino, Y., Nakagawa, M., Senga, M., Higuchi, H., Takada, K. & Sasaki, T. Analysis of the Structure and Degree of Crystallisation of 70Li2S-30P2S5 Glass Ceramic. *J. Mater. Chem. A* **3,** 2756 (2015).

104. Wang, Y., Richards, W. D., Ong, S. P., Miara, L. J., Kim, J. C., Mo, Y. & Ceder, G. Design Principles for Solid-state Lithium Superionic Conductors. *Nat. Mater.* **14,** 1026 (2015).

105. Gao, Z., Sun, H., Fu, L., Ye, F., Zhang, Y., Luo, W. & Huang, Y. Promises, challenges, and recent progress of inorganic solid-state electrolytes for all-solid-state lithium batteries. *Adv. Mater.* **30,** 1705702 (2018).

106. Manthiram, A., Yu, X. & Wang, S. Lithium battery chemistries enabled by solid-state electrolytes. *Nat. Rev. Mater.* **2,** 16103 (2017).

107. Borsa, A. A., Fricker, H. A., Bills, B. G., Minster, J.-B., Carabajal, C. C. & Quinn, K. J. Topography of the salar de Uyuni, Bolivia from kinematic GPS. *Geophys. J. Int.* **172,** 31–40 (2008).

108. Munk, L. A., Hynek, S. A., Bradley, D., Boutt, D., Labay, K. & Jochens, H. Lithium brines: A global perspective. *Rev. Econ. Geol.* **18,** 339–365 (2016).

109. Pan, H., Hu, Y.-S. & Chen, L. Room-temperature stationary sodium-ion batteries for large-scale electric energy storage. *Energy Environ. Sci.* **6,** 2338 (2013).

110. Goodenough, J. B., Hong, H. Y.-P. & Kafalas, J. a. Fast Na/+/-ion transport in skeleton structures. **I,** 203–220 (1976).

111. Nagelberg, A. S. & Worrell, W. L. A thermodynamic study of sodium-intercalated TaS2 and TiS2. *J. Solid State Chem.* **29,** 345–354 (1979).

112. Parant, J.-P., Olazcuaga, R., Devalette, M., Fouassier, C. & Hagenmuller, P. Sur quelques nouvelles phases de formule NaxMnO2 (x⩽ 1). *J. Solid State Chem.* **3,** 1–11 (1971).

113. Delmas, C., Fouassier, C. & Hagenmuller, P. Structural classification and properties of the layered oxides. *Phys. B+ c* **99,** 81–85 (1980).

114. Braconnier, J.-J., Delmas, C., Fouassier, C. & Hagenmuller, P. Comportement electrochimique des phases NaxCoO2. *Mater. Res. Bull.* **15,** 1797–1804 (1980).

115. Whittingham, M. S. Chemistry of intercalation compounds: Metal guests in chalcogenide hosts. *Prog. Solid State Chem.* **12,** 41–99 (1978).

116. Ellis, B. L. & Nazar, L. F. Sodium and sodium-ion energy storage batteries. *Curr. Opin. Solid State Mater. Sci.* **16,** 168–177 (2012).

117. Hueso, K. B., Armand, M. & Rojo, T. High temperature sodium batteries: status, challenges and future trends. *Energy Environ. Sci.* **6,** 734 (2013).

118. Hong, H.-P. Crystal structures and crystal chemistry in the system Na1+ xZr2SixP3-xO12. *Mater. Res. Bull.* **11,** 173–182 (1976).

119. Takehiko, T., Katsumi, K. & Masahiro, S. Ion Conductors. **1,** 163–175 (1980).

120. Ahmad, A., Wheat, T. A., Kuriakose, A. K., Canaday, J. D. & McDonald, A. G. Dependence of the properties of Nasicons on their composition and processing. *Solid State Ionics* **24,** 89–97 (1987).

121. Jansen, M. & Henseler, U. Synthesis, structure determination, and ionic conductivity of sodium tetrathiophosphate. *J. Solid State Chem.* **99,** 110–119 (1992).

122. Hayashi, A., Noi, K., Sakuda, A. & Tatsumisago, M. Superionic glass-ceramic electrolytes for room-temperature rechargeable sodium batteries. *Nat. Commun.* **3,** 856 (2012).

123. Krauskopf, T., Culver, S. P. & Zeier, W. G. Local Tetragonal Structure of the Cubic Superionic Conductor Na3PS4. *Inorg. Chem.* **57,** 4739–4744 (2018).

124. Krauskopf, T., Pompe, C., Kraft, M. A. & Zeier, W. G. Influence of Lattice Dynamics on Na+ Transport in the Solid Electrolyte Na3PS4--x Se x. *Chem. Mater.* **29,** 8859–8869 (2017).

125. Tanibata, N., Deguchi, M., Hayashi, A. & Tatsumisago, M. All-solid-state Na/S batteries with a Na3PS4 electrolyte operating at room temperature. *Chem. Mater.* **29,** 5232–5238 (2017).

126. Tanibata, N., Matsuyama, T., Hayashi, A. & Tatsumisago, M. All-solid-state sodium batteries using amorphous TiS3 electrode with high capacity. *J. Power Sources* **275,** 284–287 (2015).

127. Tanibata, N., Noi, K., Hayashi, A., Kitamura, N., Idemoto, Y. & Tatsumisago, M. X-ray Crystal Structure Analysis of Sodium-Ion Conductivity in 94 Na3PS4· 6 Na4SiS4 Glass-Ceramic Electrolytes. *ChemElectroChem* **1,** 1130–1132 (2014).

128. Hibi, Y., Tanibata, N., Hayashi, A. & Tatsumisago, M. Preparation of sodium ion conducting Na3PS4-NaI glasses by a mechanochemical technique. *Solid State Ionics* **270,** 6–9 (2015).

129. Hayashi, A., Noi, K., Tanibata, N., Nagao, M. & Tatsumisago, M. High sodium ion conductivity of glass–ceramic electrolytes with cubic Na3PS4. *J. Power Sources* **258,** 420–423 (2014).

130. Wan, H., Mwizerwa, J. P., Qi, X., Xu, X., Li, H., Zhang, Q., Cai, L., Hu, Y.-S. & Yao, X. Nanoscaled Na3PS4 Solid Electrolyte for All-Solid-State FeS2/Na Batteries with Ultrahigh Initial Coulombic Efficiency of 95% and Excellent Cyclic Performances. *ACS Appl. Mater. Interfaces* **10,** 12300–12304 (2018).

131. Wenzel, S., Leichtweiss, T., Weber, D. A., Sann, J., Zeier, W. G. & Janek, J. Interfacial reactivity benchmarking of the sodium ion conductors Na3PS4 and sodium $β$-alumina for protected sodium metal anodes and sodium all-solid-state batteries. *ACS Appl. Mater. Interfaces* **8,** 28216–28224 (2016).

132. Yue, J., Han, F., Fan, X., Zhu, X., Ma, Z., Yang, J. & Wang, C. High-performance all-inorganic solid-state sodium--sulfur battery. *ACS Nano* **11,** 4885–4891 (2017).

133. Yu, Z., Shang, S.-L., Seo, J.-H., Wang, D., Luo, X., Huang, Q., Chen, S., Lu, J., Li, X., Liu, Z.-K. & others. Exceptionally High Ionic Conductivity in Na3P0. 62As0. 38S4 with Improved Moisture Stability for Solid-State Sodium-Ion Batteries. *Adv. Mater.* **29,** 1605561 (2017).

134. Yu, C., Ganapathy, S., de Klerk, N. J. J., van Eck, E. R. H. & Wagemaker, M. Na-ion dynamics in tetragonal and cubic Na 3 PS 4, a Na-ion conductor for solid state Na-ion batteries. *J. Mater. Chem. A* **4,** 15095–15105 (2016).

135. Larson, A. C. & Von Dreele, R. B. Gsas. *Rep. lAUR* 86–748 (1994).

136. Toby, B. H. EXPGUI, a graphical user interface for GSAS. *J. Appl. Crystallogr.* **34,** 210–213 (2001).

137. Wu, E. A., Kompella, C. S., Zhu, Z., Lee, J. Z., Lee, S. C., Chu, I. H., Nguyen, H., Ong, S. P., Banerjee, A. & Meng, Y. S. New Insights into the Interphase between the Na Metal Anode and Sulfide Solid-State Electrolytes: A Joint Experimental and Computational Study. *ACS Appl. Mater. Interfaces* **10,** 10076–10086 (2018).

138. Berbano, S. S., Seo, I., Bischoff, C. M., Schuller, K. E. & Martin, S. W. Formation and structure of Na2S+ P2S5 amorphous materials prepared by melt-quenching and mechanical milling. *J. Non. Cryst. Solids* **358,** 93–98 (2012).

139. Larcher, D. & Tarascon, J. Towards greener and more sustainable batteries for electrical energy storage. *Nat. Chem.* **7,** 19–29 (2014).

140. Ong, S. P., Chevrier, V. L., Hautier, G., Jain, A., Moore, C., Kim, S., Ma, X. & Ceder, G. Voltage, stability and diffusion barrier differences between sodium-ion and lithium-ion intercalation materials. *Energy Environ. Sci.* **4,** 3680 (2011).

141. Deng, Z., Mo, Y. & Ong, S. P. Computational studies of solid-state alkali conduction in rechargeable alkali-ion batteries. *Npg Asia Mater.* **8,** e254 (2016).

142. Tatsumisago, M. & Hayashi, A. Sulfide Glass-Ceramic Electrolytes for All-Solid-State Lithium and Sodium Batteries. *Int. J. Appl. Glas. Sci.* **5,** 226–235 (2014).

143. Hooper, a. A study of the electrical properties of single-crystal and polycrystalline β-alumina using complex plane analysis. *J. Phys. D. Appl. Phys.* **10,** 1487–1496 (1977).

144. Anantharamulu, N., Koteswara Rao, K., Rambabu, G., Vijaya Kumar, B., Radha, V. & Vithal, M. A wide-ranging review on Nasicon type materials. *J. Mater. Sci.* **46,** 2821–2837 (2011).

145. Chu, I. H., Nguyen, H., Hy, S., Lin, Y. C., Wang, Z., Xu, Z., Deng, Z., Meng, Y. S. & Ong, S. P. Insights into the Performance Limits of the Li7P3S11 Superionic Conductor: A Combined First-Principles and Experimental Study. *ACS Appl. Mater. Interfaces* **8,** 7843–7853 (2016).

146. Zhang, L. Vacancy-contained tetragonal Na3SbS4 superionic conductor. *Adv. Sci.* 1600089 (2016).

147. Kandagal, V. S., Bharadwaj, M. D. & Waghmare, U. V. Theoretical prediction of a highly conducting solid electrolyte for sodium batteries: Na10GeP2S12. *J. Mater. Chem. A* **3,** 1–

8 (2015).

148. Zhang, L. Na3PSe4: A novel chalcogenide solid electrolyte with high ionic conductivity. *Adv. Energy Mater.* **5,** 1501294 (2015).

149. Kuhn, A., Gerbig, O., Zhu, C., Falkenberg, F., Maier, J. & Lotsch, B. V. A new ultrafast superionic Li-conductor: ion dynamics in Li11Si2PS12 and comparison with other tetragonal LGPS-type electrolytes. *Phys. Chem. Chem. Phys.* **16,** 14669–74 (2014).

150. Bron, P., Johansson, S., Zick, K., Der Günne, J. S. A., Dehnen, S. & Roling, B. Li10SnP2S12: An affordable lithium superionic conductor. *J. Am. Chem. Soc.* **135,** 15694–15697 (2013).

151. Mo, Y., Ong, S. P. & Ceder, G. First principles study of the Li 10GeP 2S 12 lithium super ionic conductor material. *Chem. Mater.* **24,** 15–17 (2012).

152. Banerjee, A. Na3SbS4: A solution processable sodium superionic conductor for all-solid-state sodium-ion batteries. *Angew. Chemie* **42988,** 9786–9790 (2016).

153. Richards, W. D., Miara, L. J., Wang, Y., Kim, J. C. & Ceder, G. Interface stability in solid-state batteries. *Chem. Mater.* **28,** 266–273 (2015).

154. Deng, Z., Wang, Z., Chu, I.-H., Luo, J. & Ong, S. P. Elastic properties of alkali superionic conductor electrolytes from first principles calculations. *J. Electrochem. Soc.* **163,** A67–A74 (2016).

155. Tanibata, N. X-ray crystal structure analysis of sodium-ion conductivity in 94Na3PS4•6Na4SiS4 glass-ceramic electrolytes. *Chem Electro Chem* **1,** 1130–1132 (2014).

156. Tanibata, N., Noi, K., Hayashi, A. & Tatsumisago, M. Preparation and characterization of highly sodium ion conducting Na3PS4–Na4SiS4 solid electrolytes. *Rsc Adv.* **4,** 17120 (2014).

157. de Klerk, N. J. J. & Wagemaker, M. Diffusion mechanism of the sodium-ion solid electrolyte Na3PS4 and potential improvements of halogen doping. *Chem. Mater.* **28,** 3122–3130 (2016).

158. Zhu, Z., Chu, I.-H., Deng, Z. & Ong, S. P. Role of Na+ interstitials and dopants in enhancing the Na+ conductivity of the cubic Na3PS4 superionic conductor. *Chem. Mater.* **27,** 8318–8325 (2015).

159. Hart, G. L. W. & Forcade, R. W. Algorithm for generating derivative structures. *Phys. Rev. B* **77,** 224115 (2008).

160. Wei, S.-H. & Zhang, S. Chemical trends of defect formation and doping limit in II–VI semiconductors: The case of CdTe. *Phys. Rev. B* **66,** 1–10 (2002).

161. Hoover, W. G. Canonical dynamics: Equilibrium phase-space distributions. *Phys. Rev. A* **31,** 1695–1697 (1985).

162. Nose, S. A unified formulation of the constant temperature molecular dynamics methods. *J. Chem. Phys.* **81,** 511 (1984).

163. Jain, A. FireWorks: a dynamic workflow system designed for highthroughput applications. *Concurr. Comput. Pr. Exp.* **27,** 5037–5059 (2015).

164. Malik, R., Burch, D., Bazant, M. & Ceder, G. Particle size dependence of the ionic diffusivity. *Nano Lett.* **10,** 4123–4127 (2010).

165. Heyd, J., Scuseria, G. E. & Ernzerhof, M. Erratum: 'Hybrid functionals based on a screened Coulomb potential'. *J. Chem. Phys.* **124,** 219906 (2006).

166. Bo, S.-H., Wang, Y. & Ceder, G. Structural and Na-ion conduction characteristics of Na3PSxSe4−x. *J. Mater. Chem. A* **4,** 9044–9053 (2016).

167. Monroe, C. & Newman, J. The Impact of Elastic Deformation on Deposition Kinetics at Lithium/Polymer Interfaces. *J. Electrochem. Soc.* **152,** A396 (2005).

168. Monroe, C. & Newman, J. Dendrite Growth in Lithium/Polymer Systems. *J. Electrochem. Soc.* **150,** A1377 (2003).

169. Porz, L., Swamy, T., Sheldon, B. W., Rettenwander, D., Frömling, T., Thaman, H. L., Berendts, S., Uecker, R., Carter, W. C. & Chiang, Y. M. Mechanism of Lithium Metal Penetration through Inorganic Solid Electrolytes. *Adv. Energy Mater.* (2017). doi:10.1002/aenm.201701003

170. McGrogan, F. P., Swamy, T., Bishop, S. R., Eggleton, E., Porz, L., Chen, X., Chiang, Y. M. & Van Vliet, K. J. Compliant Yet Brittle Mechanical Behavior of Li2S–P2S5 Lithium-Ion-Conducting Solid Electrolyte. *Adv. Energy Mater.* **7,** 1–5 (2017).

171. Wood, K. N., Noked, M. & Dasgupta, N. P. Lithium Metal Anodes: Toward an Improved Understanding of Coupled Morphological, Electrochemical, and Mechanical Behavior. *ACS Energy Lett.* **2,** 664–672 (2017).

172. Guo, Y., Li, H. & Zhai, T. Reviving Lithium-Metal Anodes for Next-Generation High-Energy Batteries. *Adv. Mater.* **29,** 1–25 (2017).

173. Ren, Y., Shen, Y., Lin, Y. & Nan, C. W. Direct observation of lithium dendrites inside garnet-type lithium-ion solid electrolyte. *Electrochem. commun.* **57,** 27–30 (2015).

174. Lin, D., Liu, Y. & Cui, Y. Reviving the lithium metal anode for high-energy batteries. *Nat. Nanotechnol.* **12,** 194–206 (2017).

175. Erlangung, Z. Mechanisms of Dendrite Growth in Lithium Metal Batteries. (2015).

176. Seitzman, N., Guthrey, H., Sulas, D. B., Al-jassim, M., Pylypenko, S. & Platt, H. A. S. Toward All-Solid-State Lithium Batteries : Three-Dimensional Visualization of Lithium Migration in β -Li 3 PS 4 Ceramic Electrolyte. **165,** 3732–3737 (2018).

177. Trevey, J. E., Gilsdorf, J. R., Miller, S. W. & Lee, S.-H. Li2S–Li2O–P2S5 solid electrolyte for all-solid-state lithium batteries. *Solid State Ionics* **214,** 25–30 (2012).

178. Yersak, T. a., Evans, T., Whiteley, J. M., Son, S.-B., Francisco, B., Oh, K. H. & Lee, S.-H. Derivation of an Iron Pyrite All-Solid-State Composite Electrode with Ferrophosphorus, Sulfur, and Lithium Sulfide as Precursors. *J. Electrochem. Soc.* **161,** A663–A667 (2014).

179. Fan, L., Wei, S., Li, S., Li, Q. & Lu, Y. Recent Progress of the Solid-State Electrolytes for High-Energy Metal-Based Batteries. *Adv. Energy Mater.* **1702657,** 1702657 (2018).

180. Jung, Y. S., Oh, D. Y., Nam, Y. J. & Park, K. H. Issues and Challenges for Bulk-Type All-Solid-State Rechargeable Lithium Batteries using Sulfide Solid Electrolytes. *Isr. J. Chem.* **742,** n/a-n/a (2015).

181. Tatsumisago, M., Mizuno, F. & Hayashi, A. All-solid-state lithium secondary batteries using sulfide-based glass-ceramic electrolytes. *J. Power Sources* **159,** 193–199 (2006).

182. Ferrese, A. & Newman, J. Mechanical Deformation of a Lithium-Metal Anode Due to a Very Stiff Separator. **161,** 1350–1359 (2014).

183. Togo, A., Chaput, L., Tanaka, I. & Hug, G. First-principles phonon calculations of thermal expansion in Ti3SiC2, Ti3AlC2, and Ti3GeC2. *Phys. Rev. B* **81,** 174301 (2010).

184. Oh, G., Hirayama, M., Kwon, O., Suzuki, K. & Kanno, R. Bulk-Type All Solid-State Batteries with 5 v Class LiNi0.5Mn1.5O4 Cathode and Li10GeP2S12 Solid Electrolyte. *Chem. Mater.* **28,** 2634–2640 (2016).

185. Ong, S. P. Voltage, stability and diffusion barrier differences between sodium-ion and lithium-ion intercalation materials. *Energy Environ. Sci.* **4,** 3680 (2011).

186. Lin, Y. C., Wen, B., Wiaderek, K. M., Sallis, S., Liu, H., Lapidus, S. H., Borkiewicz, O. J., Quackenbush, N. F., Chernova, N. A., Karki, K., Omenya, F., Chupas, P. J., Piper, L. F. J., Whittingham, M. S., Chapman, K. W. & Ong, S. P. Thermodynamics, Kinetics and Structural Evolution of ε-LiVOPO 4 over Multiple Lithium Intercalation. *Chem. Mater.* **28,** 1794–1805 (2016).